

**Single Particle Studies of Heterogeneous Atmospheric Chemistry
on Aluminum Oxide Particles in a Quadrupole Trap**

Final Report

Final Report

Prepared by:

A.J.R. Hunter, D.M. Sonnenfroh, D.B. Oakes, and W. T. Rawlins

Physical Sciences Inc.
20 New England Business Center
Andover, MA 01810

Prepared for:

Air Force Office of Scientific Research
110 Duncan Avenue, Suite B115
Bolling AFB, DC 20332-0001

Contract No. F49620-96-C-0012

March 2000

DISTRIBUTION STATEMENT A
Approved for Public Release
Distribution Unlimited

20000419 149

PSI

P H Y S I C A L S C I E N C E S I N C.

0130

REPORT DOCUMENTATION PAGE		OMB No. 0704-0188	
<p>Public reporting burden for this collection of information is estimated to average 1 hour per response, including the time for reviewing instructions, searching existing data sources, gathering and maintaining the data needed, and completing and reviewing the collection of information. Send comments regarding this burden estimate or any other aspect of this collection of information, including suggestions for reducing this burden, to Washington Headquarters Services, Directorate for Information Operations and Reports, 1215 Jefferson Davis Highway, Suite 1204, Arlington, VA 22202-4302, and to the Office of Management and Budget, Paperwork Reduction Project (0704-0188), Washington, DC 20503.</p>			
1. AGENCY USE ONLY (Leave blank)	2. REPORT DATE	3. REPORT TYPE AND DATES COVERED	
	March 2000	Final - 3/96-6/99	
4. TITLE AND SUBTITLE		5. FUNDING NUMBERS	
Single Particle Studies of Heterogeneous Atmospheric Chemistry on Aluminum Oxide Particles in a Quadrupole Trap		F49620-96-C-0012	
6. AUTHOR(S)			
A.J.R. Hunter, D.M. Sonnenfroh, D.B. Oakes, and W.T. Rawlins			
7. PERFORMING ORGANIZATION NAME(S) AND ADDRESS(ES)		8. PERFORMING ORGANIZATION REPORT NUMBER	
Physical Sciences Inc. 20 New England Business Center Andover, MA 01810		PSI-1249/TR-1664	
9. SPONSORING/MONITORING AGENCY NAME(S) AND ADDRESS(ES)		10. SPONSORING/MONITORING AGENCY REPORT NUMBER	
Air Force Office of Scientific Research 110 Duncan Avenue, Suite B115 Bolling AFB, DC 20332-0001			
11. SUPPLEMENTARY NOTES			
12a. DISTRIBUTION/AVAILABILITY STATEMENT		12b. DISTRIBUTION CODE	
Approved for public release; distribution unlimited		A	
13. ABSTRACT (Maximum 200 words)			
<p>This report documents a research program consisting of laboratory and field measurements investigating the atmospheric chemistry and aerosol microphysics of the impacts of rocket motor</p> <p style="text-align: right;"><i>(Continued)</i></p>			
14. SUBJECT TERMS		15. NUMBER OF PAGES	
		81	
		16. PRICE CODE	
17. SECURITY CLASSIFICATION OF REPORT	18. SECURITY CLASSIFICATION OF THIS PAGE	19. SECURITY CLASSIFICATION OF ABSTRACT	20. LIMITATION OF ABSTRACT
Unclassified	Unclassified	Unclassified	Unlimited

NSN 7540-01-280-5500

Standard Form 298 (Rev. 2-89) (EG)
 Prescribed by ANSI Std. Z39-18
 Designed using Perform Pro, WHS/DIOR, Oct. 94

SECURITY CLASSIFICATION OF THIS PAGE

CLASSIFIED BY:

DECLASSIFY ON:

13. ABSTRACT (Continued)

exhausts on upper atmospheric chemical cycles and ozone. The experimental investigation employs a laboratory quadrupole trap electrodynamic levitation apparatus to study heterogeneous processes on single aluminum oxide particles representative of those exhausted into the atmosphere by solid rocket motors. We have investigated the activities of different types of aluminum oxide particles for uptake of gas-phase H₂O and HCl. The particle types investigated were α -Al₂O₃, γ -Al₂O₃, H₂SO₄-treated α -Al₂O₃, H₂SO₄-treated γ -Al₂O₃, and metastable aluminum oxide formed by rapid cooling from molten Al₂O₃ in a shock tube, analogous to particle processing in a rocket exhaust nozzle. Particles were treated with H₂SO₄ by vapor deposition in an oven. The kinetic measurements consisted of independent, simultaneous observations of mass uptake and particle size increase upon exposure of single particles to fixed concentrations of H₂O or HCl in slowly flowing gas mixtures at 1 atm and temperatures from 300 K to 190 K. α -Al₂O₃ and γ -Al₂O₃ were essentially inert toward H₂O and HCl uptake, however they readily adsorbed monolayer-equivalent levels of H₂SO₄ vapor, and H₂SO₄-coated and metastable particles were active toward H₂O and HCl uptake. The measured uptake efficiencies imply fast reaction rates within rocket exhaust plumes, potentially leading to CCN behavior as well as heterogeneous chlorine activation by these particles.

The field measurements consisted of *in situ* ozone mixing ratio measurements on the NASA WB57-F high altitude aircraft, as part of a suite of instrumentation designed to characterize the chemistry and dynamics of rocket exhaust plumes in the lower stratosphere. We have observed substantial and rapid stratospheric ozone depletions within the exhaust plumes of solid-boosted liquid-fueled rockets, for periods up to ~1 hour after launch. These data, taken together with other species measurements such as ClO, CH₄, and particle concentrations, are analyzed to evaluate the primary mechanisms for ozone consumption within the plume. The reaction of O₃ with Cl, from the active-chlorine effluent of the solid-fueled boosters, appears to account for much of the observed ozone loss; however total active-chlorine concentrations in the plume are not high enough for this reaction to account for all of the loss in a strictly gas-phase reaction mechanism. Additional contributions may arise from reaction mechanisms triggered by the exhaust products of the liquid-fueled main engine, such as the direct reaction of ozone with carbonaceous soot particles.

CONTENTS

<u>Section</u>	<u>Page</u>
1. INTRODUCTION	1
2. REVIEW AND BACKGROUND.....	2
2.1 Solid Rocket Exhaust Particles	3
2.2 Atmospheric Effects	5
3. EXPERIMENTAL APPARATUS AND METHODS	6
3.1 Quadrupole Trap	6
3.2 Particle Sizing	9
3.3 Gas Reagents and Composition.....	11
3.4 Apparatus Modifications	12
3.5 Alumina Samples and Their Preparation	12
3.6 Shock-Heated Aluminum Oxide Particles	13
4 RESULTS AND ANALYSIS	14
4.1 Particle Surface Characterization and Activity for H_2SO_4 Uptake	14
4.2 Single-Particle Hydration Measurements: Virgin and H_2SO_4 -Treated Particles	21
4.3 High-Temperature H_2SO_4 Treatment: Activity for H_2O and HCl	25
4.3.1 Activity of Virgin Particles	26
4.3.2 Activity of H_2SO_4 -Treated and Shock-Heated Particles	29
5 DISCUSSION	32
5.1 Surface Chemistry	32
5.2 Atmospheric Significance	33
6 CONCLUSIONS	36
7 REFERENCES.....	39
APPENDIX A - WB57B Ozone Measurements	43
APPENDIX B - Airborne In Situ Ozone Measurements in Rocket Exhaust Plumes	53

LIST OF FIGURES

<u>Figure No.</u>		<u>Page</u>
1	Enhancement of imaginary index of solid aluminum oxide particles by rapid cooling from the melt.....	4
2	Spherical void electrodynamic trap	7
3	Schematic of quadrupole trap apparatus including temperature control and reagent supply manifold	8
4	Quadrupole trap optical diagnostics: particle imaging, optical scattering, and Raman spectrometer	9
5	Stability diagram showing the combination of AC field parameter and drag parameter which result in particle instability	10
6	Illustration of the H ₂ SO ₄ dosing process.....	13
7	SEM micrographs of untreated α -Al ₂ O ₃ particle sample, 4.5 m ² /g	17
8	SEM micrographs of H ₂ SO ₄ -treated α -Al ₂ O ₃ particle sample, 2.0 m ² /g	18
9	SEM micrographs of untreated $\gamma\alpha$ -Al ₂ O ₃ particle sample, 45 m ² /g.....	19
10	SEM micrographs of H ₂ SO ₄ -treated γ -Al ₂ O ₃ particle sample, 0.2 m ² /g	20
11	SEM micrograph of shock-heated aluminum oxide particle sample, \leq 0.3 m ² /g	21
12	Relative particle mass versus relative humidity for a heat-treated Alpha Aesar γ -Al ₂ O ₃ particle	22
13	Relative particle mass versus relative humidity for an H ₂ SO ₄ -treated Alpha Aesar γ -Al ₂ O ₃ particle	22
14	Relative particle mass versus time measured during the transition from 0 to 50% relative humidity for the H ₂ SO ₄ -treated Alpha Aesar γ -Al ₂ O ₃ particle in Figure 13	23
15	Computed limits for capillary condensation of H ₂ O in the small contact angle limit, 300 K	25

LIST OF FIGURES (Continued)

<u>Figure No.</u>		<u>Page</u>
16	Single-particle total mass and diameter versus RH over a 26-hour period, 300 K, untreated α -Al ₂ O ₃	26
17	Temperature cycling, α -Al ₂ O ₃ particle, 28.9 μ m diameter, <30 ppm H ₂ O in N ₂	27
18	Temperature cycling, γ -Al ₂ O ₃ particle, 37.1 μ m diameter, <30 ppm H ₂ O in N ₂	28
19	Temperature cycling, with added HCl: α -Al ₂ O ₃ (d = 32.5 μ m) particle dosed with 30 ppm HCl during warming cycle.....	28
20	Time profile of dosing experiment in Figure 19	29
21	H ₂ O and HCl uptake on H ₂ SO ₄ -treated γ -Al ₂ O ₃ particle at 298 K	30
22	H ₂ O and HCl uptake on shock-heated metastable-phase aluminum oxide particle at 298 K	30
23	Köhler curves for the hydration growth of a spherical H ₂ SO ₄ -coated aluminum oxide particle with initial radius of 60 nm and solute coverages of 0.1, 0.3, and 0.5 monolayer (ML)	35
24	Köhler critical supersaturations as a function of surface coverage for spherical H ₂ SO ₄ -coated aluminum oxide particles with initial radii of 20, 40, 60, and 80 nm	36

LIST OF TABLES

<u>Table No.</u>		<u>Page</u>
1	Minimum Particle Radii to Observe Balancing Instability as a Function of Particle Density for Maximum AC Voltage of 1000 V at 60 Hz.....	11
2	Particle Treatments and Activities for H ₂ SO ₄ Vapor	15
3	Summary of Single-Particle Gas Uptake Results.....	31

ACKNOWLEDGMENTS

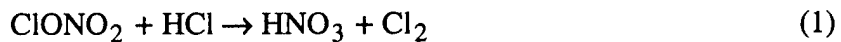
We are grateful to several colleagues for laboratory assistance and stimulating discussions. J. R. Morency and A. Petti (both of PSI) assisted with the particle characterization. S. J. Davis (PSI), B. E. Wyslouzil (Worcester Polytechnic Institute), S. Arnold (Polytechnic University), S. M. George (University of Colorado), M. J. Molina (MIT), M. N. Ross (Aerospace Corp.), and P. D. Whitefield (University of Missouri-Rolla) contributed generously to many enlightening discussions during the course of the work.

This report documents a research program investigating the atmospheric chemistry and microphysics of the impacts of rocket motor exhausts on upper atmospheric chemical cycles and ozone. The experimental investigation employs a laboratory quadrupole trap electrodynamic levitation apparatus to study heterogeneous processes on single aluminum oxide particles representative of those exhausted into the atmosphere by solid rocket motors. We have investigated the effects of rocket-exhausted and ambient atmospheric species on particle hydration kinetics and catalytic activity, including a comparison of the chemical and optical properties of shock-heated aluminum oxide particles as surrogates for rocket-fired particulates. The overall objective of these measurements is to provide a basis for and contribute to an assessment of the environmental impact of potential new solid fuel propulsion systems.

As an additional part of this program, we have used the PSI UV Ozone Photometer on board the NASA WB57-F high-altitude aircraft to make *in situ* measurements of ozone in the ambient and rocket-perturbed upper atmosphere. These measurements were performed as part of two multi-investigator field missions focussed on detailed, *in situ* characterization of species concentrations and reaction kinetics in solid-fueled and solid-boosted liquid-fueled rocket exhaust plumes. A detailed description of the measurement results and a kinetics analysis from the first of these missions is given in Appendix B. A summary description of the measurement results from the second mission and an update of the kinetics analysis are given in Appendix A. The laboratory aerosol chemistry work is described in the main text below.

1. INTRODUCTION

The major exhaust products of solid rocket motors include H₂, H₂O, HCl, Cl₂, CO, N₂, CO₂, and aluminum oxide (nominally Al₂O₃) particles. The deleterious effects of the emitted gas phase species, in particular HCl and Cl₂, on stratospheric ozone levels have been addressed by several modeling studies,¹⁻⁴ and the potential for ice nucleation on the particles has been modeled by Turco et al.⁵ Previous modelers^{2,3} have predicted insignificant effects of aluminum oxide particles on ozone chemistry, however these studies considered only the heterogeneous conversion of ambient reservoir species (N₂O₅, ClONO₂), on a globally averaged basis. In fact, the aluminum oxide surface itself is well known to be catalytically active towards adsorption of H₂O and other species,⁶ and this activity may play a role in the localized chemistry of the evolving rocket wake both in the stratosphere and in the troposphere. For example, work by Robinson et al⁷ demonstrated the dissociative adsorption of halomethanes on clean, single-crystal α -Al₂O₃ surfaces in ultra-high vacuum. Such processes occurring on atmospheric aluminum oxide particles would lead to an enhancement of the chlorofluorocarbon (CFC) dissociation rate, which would contribute to the opposing effects of ozone destruction in the stratosphere and CFC removal in the troposphere. More recently, Molina et al⁸ measured a reaction probability $\gamma = 0.02$ for the activation of chlorine nitrate by HCl on hydrated α -Al₂O₃ surfaces:



Thus sufficient surface area of Al₂O₃ aerosol deposited in the lower stratosphere by solid rocket launches could significantly enhance the production rate of free chlorine (Cl₂), resulting in increased ozone destruction. However, direct particle size distribution sampling in solid rocket

exhaust plumes indicates that the available Al_2O_3 surface area from a given launch is small, mitigating this effect.⁹

The chemistry of "real" aluminum oxide particles in the atmosphere is complex, because of the potential enhancement and/or poisoning effects of adsorbed plume and ambient species (e.g., H_2O , HCl , HNO_3 , SO_2 , and H_2SO_4), the possibility of photochemical effects on the adsorbates due to exposure to ultraviolet solar radiation, and the likelihood that other, more catalytically active, phases besides pure $\alpha\text{-Al}_2\text{O}_3$ may be present. The experiments undertaken in this program have investigated these effects for plume and ambient species, as well as for particles composed of the α and metastable phases. This research bridges the gap between fundamental studies of detailed heterogeneous reaction mechanisms and direct sampling of processes occurring in atmospheric solid rocket plumes by including examinations of both high purity commercial alumina particles and shock-heated particles to simulate the effects of rocket firing on the particle structure and phase. The results will aid in the identification and quantification of the key microphysical and chemical processes which must be considered in assessing the environmental impacts of solid rocket operations in the stratosphere and troposphere.

The potential chemical and microphysical phenomena listed above cover a wide range, and could lead to complex interactions with the chemical cycles of O_3 , NO_x , and ClO_x in the stratosphere and upper troposphere. The development of acid/ice aerosols can affect the sequestration of NO_x and ClO_x in the stratosphere and the formation of high-altitude clouds and acid rain in the troposphere, especially in localized regions of the atmosphere processed by passage of the exhaust plume. The catalytic processes leading to species dissociation could significantly alter the oxidizing capacity of the atmosphere within plume-affected air parcels, resulting in hitherto unsuspected effects on the local atmospheric photochemistry. The overall objective of the proposed research is to investigate these classes of heterogeneous reactions on single aluminum oxide particles, 10 to 30 μm diameter, under controlled reagent conditions and at representative atmospheric temperatures (190 to 300 K).

We have investigated the activation of aluminum oxide aerosols by plume processing using the quadrupole trap apparatus described in Section 3. Activation of aluminum oxide particles by adsorption of H_2SO_4 was studied by following the mass uptake of single, pretreated particles exposed to controlled relative humidity. These particles were pretreated by vapor deposition of H_2SO_4 in an oven prior to insertion into the trap. Through control of the deposition rate of H_2SO_4 by changing the oven temperature, we observed variations of the hydration behavior with water soluble mass fraction. Commercially available α - and $\gamma\text{-Al}_2\text{O}_3$ were used for the model aluminum oxide aerosol. Shock-heated alumina particles were used as surrogates for rocket-exhausted aluminum oxide particles.

The following sections review the background of aluminum oxide particle phenomenology in solid rocket exhausts and in atmospheric reactions, describe the experimental apparatus and methods, and present the experimental results and analysis, discussion, and conclusions.

2. REVIEW AND BACKGROUND

2.1 Solid Rocket Exhaust Particles

It is important to understand the chemical and physical processes by which rocket exhaust particulates are formed, and to realize that the model system of pure-form α -Al₂O₃ is probably an oversimplification of their actual structures, compositions and morphologies. The characteristics of rocket-exhausted aluminum oxide particles have received much attention over the last two decades owing to their importance as a source of intense, continuum radiation in the high-temperature exhaust plumes of solid rocket motors. Much of this work was reviewed by Reed and Calia.¹⁰ In brief, the observed visible and short-wavelength infrared radiances due to particulates in solid rocket plumes are much too intense to be accounted for by plume models using the accepted high-temperature optical properties of α -Al₂O₃. This still-unsolved discrepancy has prompted a large number of test stand measurements and laboratory investigations, including a series of shock tube investigations by Rawlins and coworkers at PSI funded by the Air Force Astronautics Laboratory^{11,12} and NASA Marshall Space Flight Center.¹³⁻¹⁵

Solid-propellant rockets use a propellant casting consisting of aluminum fuel, ammonium perchlorate oxidizer, and a hydrocarbon binder (e.g., carboxyl-terminated polybutadiene). The fuel and oxidizer are cast as fine powders in the 10 to 100 μ m size range. Materials such as iron oxide or carbon black may also be used to modify the burn rate. The aluminum grains are borne in a flow driven by combustion of the binder, where they vaporize and burn at temperatures near 3000 K and pressures near 100 atm. This process ultimately forms spherical liquid aluminum oxide droplets (melting temperature 2320 K) in a bimodal size distribution, i.e., submicron particles from the combustion of aluminum vapor followed by nucleation, and supramicron particles from the heterogeneous combustion of the aluminum grains. Liquid aluminum oxide is well known to be highly emissive in the visible and short-wavelength infrared, in marked contrast to the transparent behavior of α -Al₂O₃ in this spectral regime. As the high-temperature, two-phase flow expands through the rocket nozzle, the initially molten particles cool rapidly (10⁵ to 10⁶ K/s) to temperatures below the melt point (2320 K), and pass into the solid phase, maintaining a reasonably spherical shape. The dynamics of this phase change are poorly understood, and may be related to the apparently enhanced emissivity of aluminum oxide particles in the plume. By analogy to the results of electrohydrodynamic atomization experiments,¹⁶ the rapid cooling process may lead to the formation of cubic ($\gamma, \eta, \delta, \theta$), amorphous, or other metastable phases, particularly for the smaller particles. However, in an afterburning plume, these could be converted in the afterburning region to the familiar α (hexagonal close-packed) phase.¹⁷

Shock tube experiments at PSI have demonstrated the formation of a highly emissive, and potentially highly catalytically active, metastable solid phase during the rapid cooling process.¹³⁻¹⁵ In these experiments, pure-form, submicron α -Al₂O₃ particles were shock-heated in an argon bath to 3000 K, and were then rapidly quench-cooled below the melting point by a rarefaction wave at cooling rates comparable to those in the expanding rocket plume. Upon cooling through the melting point, the large decrease in emissivity expected for a phase change from the liquid to α -Al₂O₃ was not observed; indeed, the observed spectral emissivities remained comparable to those of the liquid to temperatures at least 600 K below the melting point, with no

discernible recalescence effect. Particles processed in this fashion, subsequently collected from the shock tube at room temperature, and shock-heated to submelt temperatures, also exhibited enhanced spectral emissivities compared to α -Al₂O₃ at similar temperatures, signifying the formation of a long-lived metastable solid phase of aluminum oxide.

To illustrate this, Figure 1 compares the measured imaginary refractive indices for pure-form α -phase and thermally processed aluminum oxides near 1800 K. The three-order-of-magnitude increase in imaginary index near 1 to 2 μ m signifies conversion of the material from an insulator to a semiconductor, with a corresponding decrease in the band gap from 8.8 eV (300 K) for α -Al₂O₃ to as low as \approx 3 eV for the thermally processed material. In addition, energy dispersive x-ray analysis of the processed aluminum oxide gives a cubic crystalline pattern which does not conform to any of the 21 known phases of aluminum oxide. This apparently metastable phase may be at least partly responsible for the high emissivities of rocket plume particulates, and may represent some of the material that enters the atmosphere. If this occurs, the reduced band gap will, in effect, activate the material as a semiconductor catalyst for a variety of

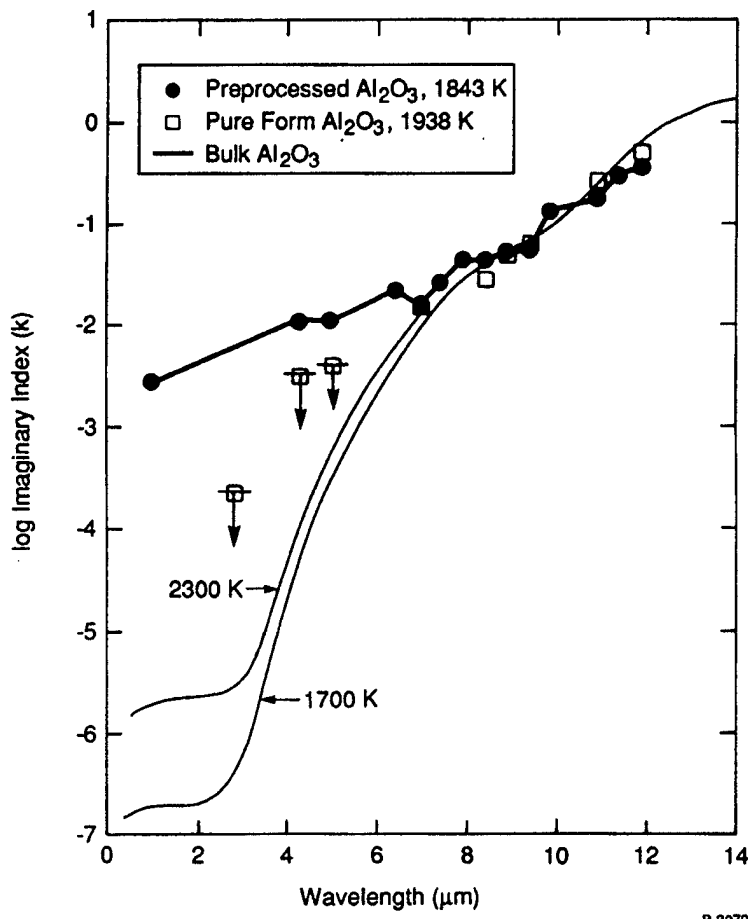


Figure 1. Enhancement of imaginary index of solid aluminum oxide particles by rapid cooling from the melt. Downward arrows signify measurement upper bounds, i.e., S/N = 1. Solid curves are taken from literature values for bulk α -Al₂O₃.

photoassisted heterogeneous reactions, leading to previously unexpected effects on atmospheric chemistry. Clearly, this possibility bears further investigation.

In addition to the possibility of metastable phase formation, rocket-exhausted aluminum oxide particles may contain metal or carbonaceous contaminants which would also affect their catalytic activity. Since the supramicron particles arise from heterogeneous combustion of aluminum grains, some traces of unburned aluminum metal may be present. In addition, post-combustion samples from test stand firings often show trace metal contaminants, however it is not clear whether these arise from the combustor or from the collection process. For example, rocket exhaust particles sampled by AEDC from a motor test and provided to PSI by the Air Force Astronautics Laboratory were found to contain substantial impurities of Fe, Cr, and carbon, possibly due to contamination by stainless steel during the collection process.¹¹ For this reason it is important to obtain carefully sampled rocket exhaust particles from the atmosphere, characterize their composition and structure, and compare their chemical behavior to that observed for idealized, α -Al₂O₃.

2.2 Atmospheric Effects

The concentration of micron-sized particles in the stratosphere has risen sharply since the 1970's, in part due to solid rocket exhaust particles.¹⁸ During a Shuttle launch, approximately 2/3 of the exhausted aluminum oxide particles are deposited in the troposphere, and 1/3 in the stratosphere.¹⁹ The particle size distributions are typically found to be bimodal, with a component at 0.3 μ m and the other mode at 2 to 8 μ m.^{19,20} Early atmospheric sampling measurements reported the particle compositions to be mostly α -Al₂O₃ with some γ -Al₂O₃,^{21,22} however this has not been confirmed by subsequent atmospheric particle sampling. Microscopic examination of collected particles shows generally spherical shapes, with surface deformations and cracks extending into the interior as might be expected due to the shrinkage in molar volume of the material upon solidification.²⁰ The lifetime of the submicron particles in the stratosphere is substantial, \approx 4 years for 0.01 μ m radius and 0.3 years for 1 μ m radius; hence it is possible for launch-injected aluminum oxide particles to eventually spread over hemispheric areas.^{5,23} Rocket-exhausted aluminum oxide particles are also a major component of stratospheric aerosol in the 1 to 10 μ m size range.¹⁸

Rocket-exhausted aluminum oxide particles may affect tropospheric and stratospheric radiative balance through nucleation and growth of water ice clouds, both locally in the launch corridor and globally.⁵ In addition, these particles tend to be active toward chemisorption of HCl²⁴ and dissociative chemisorption of CFCs.⁷ Plume particle surfaces are likely to contain adsorbed H₂O and HCl, which will interact with ambient atmospheric species. For example, due to the high solubility of HCl in HNO₃,²⁵ HCl-covered aluminum oxide particles may be effective in the uptake of atmospheric HNO₃. There is also potential for uptake of ambient H₂SO₄, which could result in incorporation of rocket particles into the background sulfuric acid aerosol budget. The presence of adsorbed species such as H₂O and HCl from the plume and HNO₃ and H₂SO₄ from the atmosphere may impact the potential for water/ice cloud formation, as well as the chemistry of CFC adsorption on the surfaces.

Irradiation of the adsorbed species by ultraviolet light (250 to 400 nm) in the upper troposphere and stratosphere can initiate photoassisted reactions, especially if the rocket-exhausted material has semiconductor properties or metallic impurities as discussed above. Experimental evidence exists for both the enhancement of photodissociation cross sections of adsorbed molecules and the shifting of the absorption spectrum to wavelengths longward of the gas phase absorption threshold,^{26,27} effects which would enhance solar photolysis rates at lower altitudes. If, as discussed above, a metastable phase of aluminum oxide with a reduced (semiconductor) band gap plays a role in the atmosphere, the particles themselves may absorb solar radiation in the 300 nm region. The absorbed light would increase the number of conduction band electrons and valence band holes in the aluminum oxide, enabling photoassisted chemisorption/dissociation processes analogous to those observed for other metal oxide systems such as TiO₂.²⁸ As an additional photochemical effect to consider, absorption of ultraviolet light by 1 to 10 μm aerosols can result in cavity-enhanced energy transfer via morphological resonances,²⁹⁻³¹ possibly affecting the dynamics of adsorbed species on the surface of the particle.

The potential chemical and microphysical phenomena listed above cover a wide range, and could lead to complex interactions with the chemical cycles of O₃, NO_x, and ClO_x in the stratosphere and upper troposphere. The development of acid/ice aerosols can affect the sequestration of NO_x and ClO_x in the stratosphere and the formation of high-altitude clouds and acid rain in the troposphere, especially in localized regions of the atmosphere processed by passage of the exhaust plume. The catalytic processes leading to species dissociation could significantly alter the oxidizing capacity of the atmosphere within plume-affected air parcels, resulting in hitherto unsuspected effects on the local atmospheric photochemistry. The objective of the present research is to investigate these classes of heterogeneous reactions on single aluminum oxide particles, 10 to 30 μm diameter, under controlled reagent conditions and at representative atmospheric temperatures (190 to 300 K).

3. EXPERIMENTAL APPARATUS AND METHODS

3.1 Quadrupole Trap

The trap geometry is a spherical void electrodynamic levitator as shown schematically in Figure 2.^{32,33} This geometry is easier to manufacture than the more traditional hyperbolic electrodes since the spherical void can be machined using a ball end mill. This geometry also has a stronger trapping potential since the electric field's quadrupole moment is a factor of two larger than that of the hyperbolic design.^{33,34} The trap is fabricated in three sections as shown in Figure 2. These sections are constructed from high purity copper and are electrically isolated from one another by 1 mm thick sapphire inserts which are sandwiched between the sections. The sections are fastened together with stainless steel screws, which are insulated with ceramic washers. An AC bias (100 to 1000 V rms) is applied to the middle "ring" electrode which produces the trapping field. This section includes four holes positioned in 90 deg intervals around the electrode for optical access to the center of the spherical void. The endcaps include 4 mm diameter holes for particle injection into and removal from the trap, and are biased with a DC voltage (2 to 200 V typical) which serves to counter the gravitational effect on the particle.

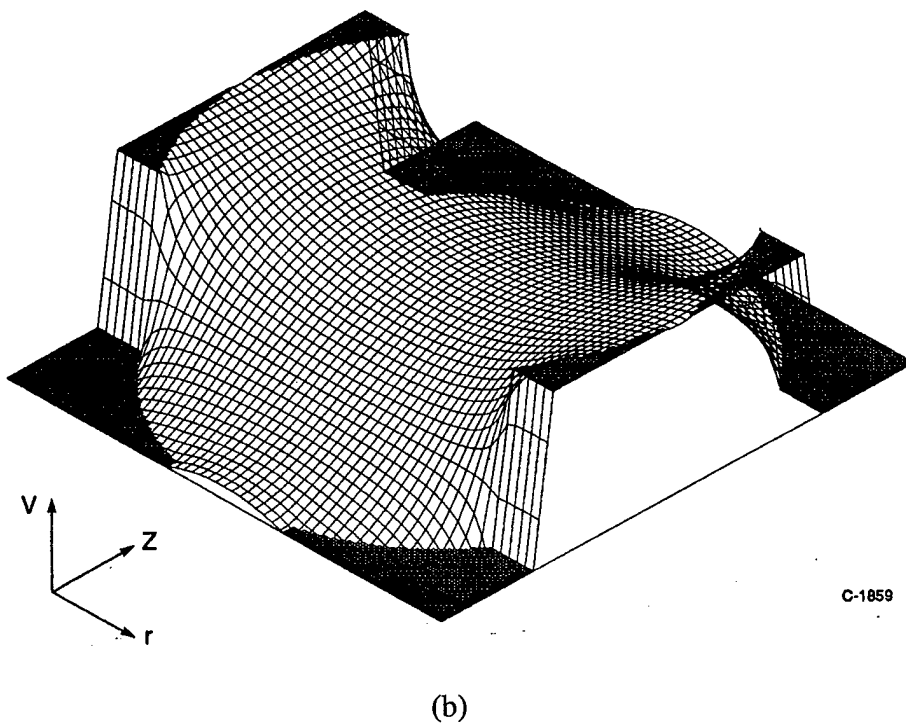
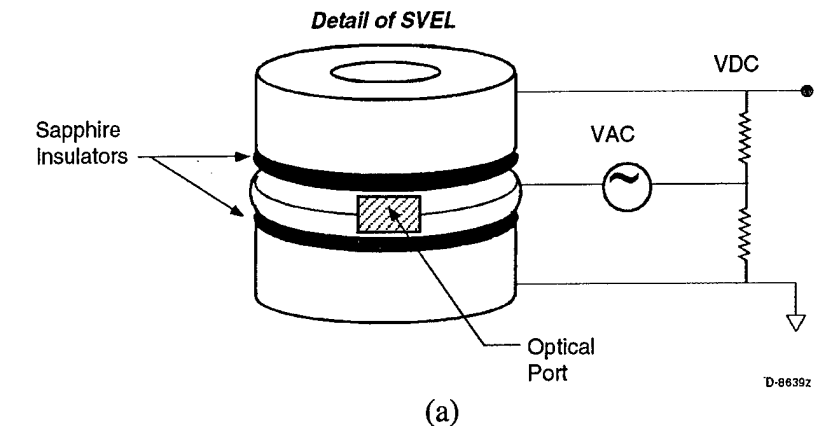


Figure 2. Spherical void electrodynamic trap: (a) schematic of trap geometry showing position of electrodes; (b) calculated AC potential surface.

Figure 2 illustrates both the trap and the AC potential within it. The DC voltage is provided by a commercial low current, high voltage supply. One of the endcap electrodes is grounded and the other is biased. If the top endcap is the biased electrode, negatively charged particles are balanced with positive voltages. The AC supply is a combination of a variable transformer (0 to 140 V) and a step up transformer, providing 0 to 1800 V at 60 Hz. The AC and DC voltages are measured with a digital volt meter.

The environmentally controlled trap facility is illustrated in Figure 3. The trap is mounted in a temperature controlled flow cell. The small mass of the trap enables temperature

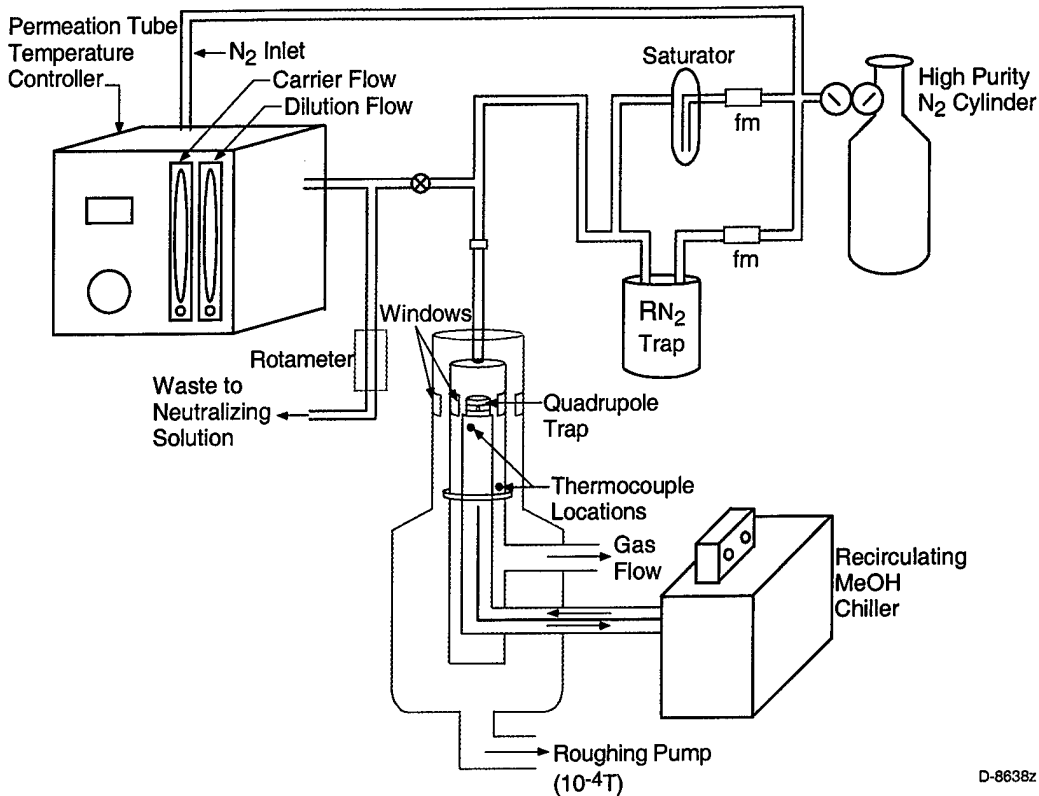


Figure 3. Schematic of quadrupole trap apparatus, including temperature control and reagent supply manifold.

control by flowing methanol from a recirculating chiller through the cold block; the trap is routinely cooled to 185 K. The flow cell is enclosed in a vacuum jacket to minimize conductive thermal losses. The relative humidity in the trap volume is controlled by mixing metered flows of dry nitrogen and nitrogen that has passed through a water saturator.

We have several optical diagnostics for single particle measurements in our facility, as illustrated in Figure 4. For balancing, sizing, and optical scattering measurements, the particle is illuminated with a 3 mW, linearly polarized HeNe laser. Light scattered at 90 deg is imaged with a microscope-based video camera system for viewing the particle. Light scattered at 135 deg is detected through a slit in the ring electrode by the linear array of an Optical Multichannel Analyzer (OMA) system to obtain angularly resolved optical scattering patterns. For spherical particles, the angular scattering patterns can be analyzed via Mie scattering theory to obtain particle size and/or index of refraction. As illustrated in Figure 4, we have also used a 0.3 m monochromator with the OMA to obtain Raman spectra of various liquid-phase particles in the trap.

Solid particles are inserted into the quadrupole trap by the following procedure. The top of the environmental chamber which houses the trap is removed, allowing access to the top of the trap. The AC and DC trap voltages are set to values that enable particles of the desired size to be

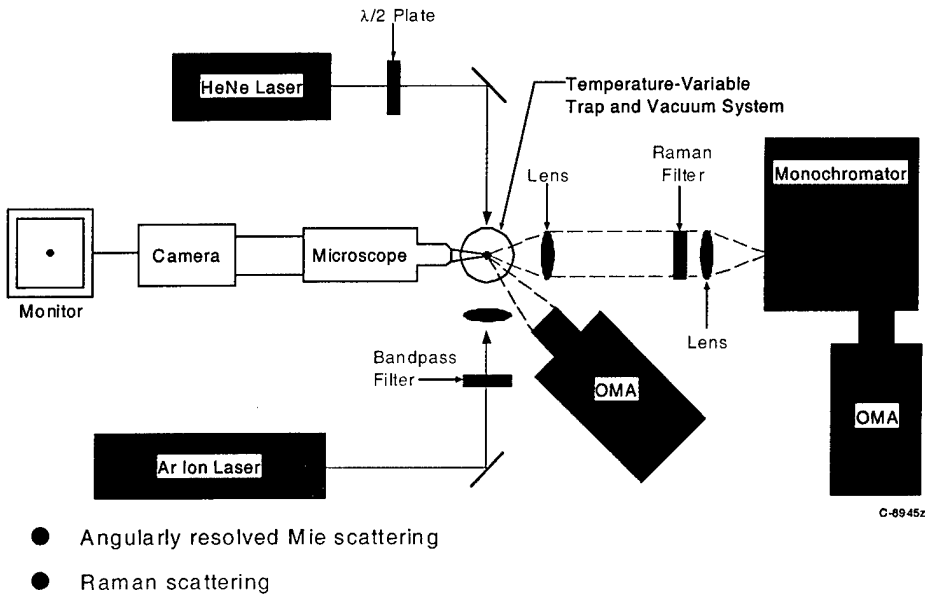


Figure 4. Quadrupole trap optical diagnostics: particle imaging, optical scattering, and Raman spectrometer.

captured (AC \sim 400 V, DC \sim 40 V). A few grains of the sample to be analyzed are then picked up on the end of a nylon wire-tie and are scraped across the top surface and over the hole of the uppermost electrode of the trap. The static charge on the alumina particles that results from this procedure ($\sim 10^4$ charges/particle) is enough to enable stable capture in the trap. After capturing a particle, the AC and DC voltages are adjusted to stably trap the particle in the center of the spherical void as observed on the video monitor of the HeNe laser scattering diagnostic. The lid of the environmental chamber is then reattached and the desired gas flow (relative humidity) is established.

3.2 Particle Sizing

The particle aerodynamic diameters were determined by the spring point balance method. This method is based on the interplay between the trapping potential provided by the AC field and the aerodynamic drag. At moderate AC fields, these two forces balance each other and confine the particle to a small region of the trap. However, as the AC trapping voltage becomes larger, the AC field strength becomes sufficient to overcome the drag and to harmonically drive the particle to oscillate with larger amplitude. This point is visually obvious in the magnified video image when viewing the particle while increasing the AC voltage.

The conditions for instability or oscillation have been extensively analyzed by several groups for a wide variety of trap geometries.³⁴ The equations of motion, as determined from the force balance on the particle, can be solved mathematically based on the Mathieu equations as a function of two parameters: ϵ' , the AC field strength parameter and δ , the drag parameter. These variables are given by:

$$\epsilon' = \frac{2C_1 V_{sp} g}{V_{dc} C_0 z_0 \omega^2} \quad \delta = \frac{9\mu}{(1+f) \rho \omega a^2} \quad (2)$$

where

V_{sp} is the AC voltage at which oscillation begins
 V_{dc} is the DC balancing voltage
 g is the gravitational constant
 C_0 and C_1 are geometric constants for a given trap geometry
 z_0 is the trap radius
 ω is the AC driving frequency
 μ is the viscosity of the bath gas
 $1+f$ is the Cunningham drag correction
 ρ is the particle density
and a is the particle radius.

Because ϵ' is related to the spring point voltage at which the particle begins to oscillate and the DC balance voltage, it can be measured for each particle. The stability diagram (Figure 5) then gives the corresponding drag parameter from which the particle size can be determined. (This analysis is for a spherical particle though in principle, other particle shapes can be handled with their corresponding drag parameters). This method is easy to implement by visually observing the particle and can be used to determine the particle mass with 5% accuracy.

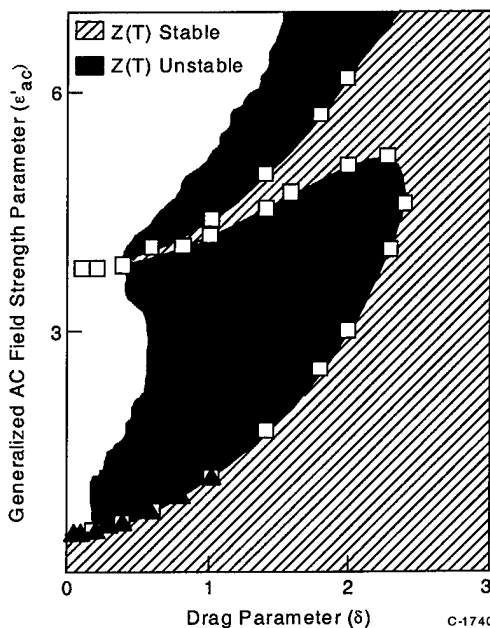


Figure 5. Stability diagram showing the combination of AC field parameter and drag parameter which result in particle instability.

Because the drag parameter is inversely proportional to particle radius squared, smaller particles have larger drag parameters. For the operating conditions used in this work (the maximum AC voltage: 1000 V, the AC frequency: 60 Hz, the trap geometry: $z_0=0.635$, $C_0=1$, $C_1=1$ and particle charges) the AC field parameter is always less than six. As shown in Figure 5, the maximum drag parameter at which instability will be observed for $\epsilon' \leq 6$ is $\delta \leq 2.42$. Therefore, particles with a drag parameter greater than 2.42 will never become unstable with the current operating trap parameters. For a given particle density, this corresponds to a minimum particle radius below which particle instability will not occur. Table 1 shows the minimum particle radii required to observe instabilities as a function of density for the operating conditions used in this work. The density of alumina is 3.97 g/cm³ which corresponds to a minimum radius of 4.7 μm for determination by the springpoint method. For the experiments reported here, the springpoint method can only be used to give a relative measure of the particle size since the particles vary from nearly cubic to roughly spherical and their density will be somewhat less than bulk density due to pores and voids in the particles.

Table 1. Minimum Particle Radii to Observe Balancing Instability as a Function of Particle Density for Maximum AC Voltage of 1000 V at 60 Hz

Density (g/cm ³)	Minimum Particle (radii μm)
1.2	8.6
2.0	6.6
3.97	4.7

3.3 Gas Reagents and Composition

The facility has a temperature regulated gas handling system for dosing trapped particles with controlled flows of various reagents at atmospherically relevant compositions. Mixtures of water vapor and dry nitrogen of known compositions were prepared using a bakeable preparation line with calibrated flow meters and pressure gauges. We prepare H₂O/N₂ mixtures by flowing the dry N₂ through a temperature-controlled saturator to take up the saturated water vapor. This mixture is then diluted with dry nitrogen to the desired final composition. The gas can then flow into a temperature-controlled cell, is cooled with blow-off gas from a liquid nitrogen tank to reach the desired temperature, and is introduced into the trap. The gas cell and quadrupole trap are held at the same temperature to prevent supersaturation. We have calibrated the water delivery system in H₂SO₄ trapping experiments,³⁵ by a dew point hygrometer, and by optical absorption measurements using a near-IR diode laser hygrometer.

The nitrogen used for water vapor dosing has a purity rating of 99.995% while the water used in the saturator is the Deionized, Ultrafiltered grade from Fisher. The concentrated sulfuric acid used for H₂SO₄ dosing is the Optima grade from Fisher.

In separate time-resolved humidity measurements by near-IR diode laser absorption, we have determined the equilibration time for the apparatus inner surfaces to be ~15 minutes for each change in RH setting. This is also consistent with time-resolved observations of hydration

of sulfuric acid droplets. The observed gas uptake rates were determined over periods of several hours, and thus are not affected by the apparatus equilibration time.

3.4 Apparatus Modifications

In order to introduce HNO_3 and HCl into the quadrupole trap reactor, we have passivated the internal metal surfaces to prevent corrosion and insure high cleanliness. The electrodynamic trap must be constructed from copper to achieve good thermal and electrical conductivity; however, this material is highly reactive with many of the reagents of interest. In addition, the reactor inlet manifold consisted of stainless steel tubing which might be active toward gas phase acids and other species. First, we fabricated a new copper electrodynamic trap and had it coated with gold, rendering it impervious to acid attack. Second, we replaced the inlet gas handling system with silicon dioxide coated stainless steel tubing (Silcosteel) to eliminate losses of the reagents by reaction with the walls of the delivery tubing.

To facilitate the introduction of well-calibrated flows of trace gas reagents, we have incorporated a permeation tube inlet system consisting of a VICI Metronics oven and a set of calibrated permeation tubes containing the reagents of interest. This approach minimizes experimental complexity and maximizes the purity of the admitted gases. The principle behind the permeation device is simple. A small quantity of the chosen reagent is sealed by the manufacturer in a small length of teflon tubing. The emission rate of the gas phase species from this sealed tube is calibrated by holding the tube at a specified temperature for a measured time, and observing the weight change of the tube over that interval. This emission rate is usually in the ng/min range, and can easily be diluted both inside the temperature-controlled oven and after the gas stream emerges.

The permeation tube oven has been mated with the Silcosteel gas handling system, as illustrated in Figure 3. This system can now be used to expose levitated Al_2O_3 particles to metered flows of HCl and HNO_3 at concentrations representative of those found in rocket exhaust plumes and in the background stratosphere. Other species of atmospheric importance are also available in permeation tubes, including SO_2 , NO_2 , NH_3 , and many halocarbons.

3.5 Alumina Samples and Their Preparation

Alumina samples were obtained from two vendors for these studies. α and γ alumina were purchased from Alfa Aesar / Johnson Matthey with nominal particle sizes specified as $110\text{ }\mu\text{m}$. This size designation is a crude estimate of the peak of the particle diameter distribution which ranged from less than one micron to several hundred microns. Both alumina samples purchased from Alfa Aesar were composed of particles with a shape that was approximately cubic. The α -alumina sample (99.997%, stock # 38368) has a specified surface area of $9\text{ m}^2/\text{gram}$ while the specified surface area of the γ -alumina sample (99.999%, stock #36264) is $55\text{ m}^2/\text{gram}$.

Two α -alumina samples manufactured by the Bayer process (99.8% purity) with a specified size of $60\text{ }\mu\text{m}$, referred to as A-10 and A-13, were obtained from the Alcoa Powders

Division. The A-10 sample is comprised of 100% α -alumina with a specified surface area equal to $0.5 \text{ m}^2/\text{gram}$ while the A-13 sample is largely α -alumina but contains 5 to 7% γ -alumina and has a surface area in the range 10 to $13 \text{ m}^2/\text{gram}$. The particles in both these samples are roughly spherical and have a specified porosity of 60 to 70%.

Hydration experiments were conducted with these samples as provided and also after heat and acid treatments. The heat treatment involved heating the samples to 135 or 165 C in an oven for more than 24 hours. The particles were then removed from the oven and were inserted into the trap. Generally less than 15 min elapsed between removal of the treated sample from the oven and capture of a particle in the trap. The technique for H_2SO_4 dosing of the samples is shown schematically in Figure 6. Approximately 20 mg of an alumina sample on a watch glass was placed in a glass container along with 10 ml of concentrated sulfuric acid. This assembly was then placed in an oven at 135 or 165 C for greater than 24 hours. The weight of the alumina sample was measured to a precision of 0.1 mg before and after the acid treatment to quantify the mass uptake due to the treatment.

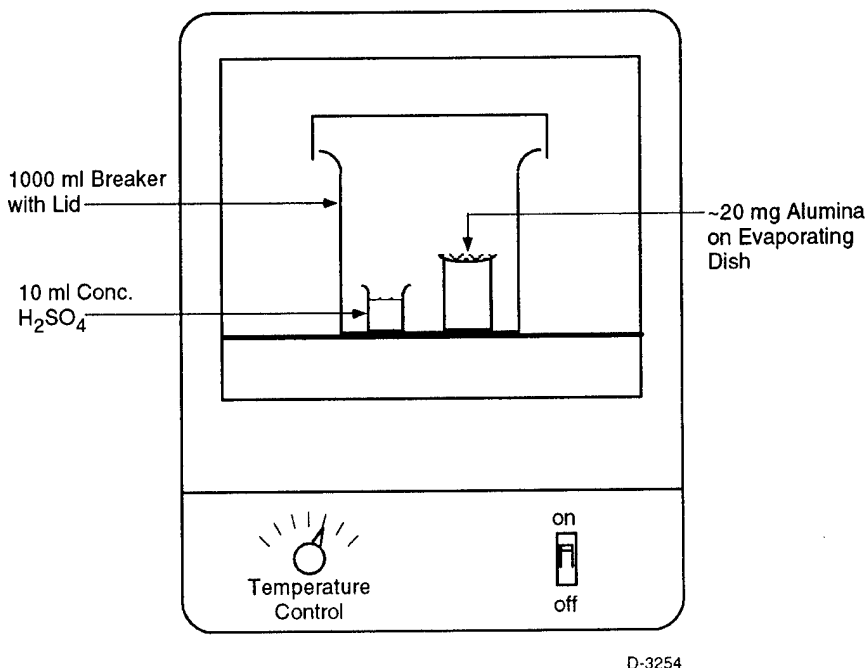


Figure 6. Illustration of the H_2SO_4 dosing process

3.6 Shock-Heated Aluminum Oxide Particles

Shock-heated aluminum oxide particles were prepared as described in Section 2.1, in order to simulate the effects of rocket firing on the structure and reactivity. A small sample of commercial, pure-form α - Al_2O_3 particles was placed in the reflected shock region (i.e. near the end wall) of the test section of a conventional, 4-inch (i.d.) shock tube. The shock tube facility is described in detail elsewhere.³⁶ The shock tube was slowly evacuated, and then was filled with

UHP-grade argon. Using hydrogen driver gas and a double-diaphragm burst technique, a shock was fired to achieve reflected shock conditions of 3000 K and 20 atm. Wall pressure and optical pyrometry measurements of particle emissivities^{11,12} verified that the reflected shock condition was maintained for 2 ms, during which time the aerodynamically suspended particle field reached equilibrium with the gas phase reflected shock temperature. The reflected shock period was terminated by the arrival of the rarefaction wave reflected from the driver end wall. The rarefaction wave created a period of rapid cooling which lasted about 2 ms. From dual-wavelength radiometric observations of the aerosol thermal emission,^{13,14} we observed the maximum cooling rate to be $\sim 2 \times 10^6$ K/s. During the rarefaction wave period, the suspended particles cooled from ~ 3000 K to ~ 1600 K, i.e. from well above the 2320 K melting point to well below it. These cooling rates and temperatures are similar to those experienced by aluminum oxide particles in solid rocket exhaust plumes,¹⁰ albeit in an exhaust gas environment rather than argon. The shock-heating process was repeated several times for the same particle sample. The sample was then collected and removed from the shock tube. Portions of the sample used in the quadrupole trap experiments were dried in an oven and were introduced into the electrodynamic trap without further treatment.

We noted a change in color of the particles from initially white as received to gray following the shock-heating treatment. Energy-dispersive x-ray analysis of a portion of the sample indicated a cubic structure which could not be identified in terms of the known crystal structures of aluminum oxide. No measurable contamination was introduced during the treatment. Another portion of the sample was subjected to quantitative emissivity measurements in the shock tube at a reflected shock temperature of 1843 K, well below the melting point; these measurements (Figure 1) yielded greatly enhanced visible and near-infrared absorption coefficients, suggesting a ~ 5 eV reduction in the material's band gap as discussed in Section 2.1. We speculate that the alteration of the material properties occurred through evaporative depletion of oxygen while in the liquid phase, followed by rapid solidification into a long-lived, metastable, oxygen-poor lattice structure. While this condition would not be expected to persist in a high-temperature oxidizing environment,¹⁵ it may be applicable to the bulk of the rocket-exhausted particles near the plume centerline immediately downstream of the nozzle and prior to the afterburning region.

4. RESULTS AND ANALYSIS

4.1 Particle Surface Characterization and Activity for H₂SO₄ Uptake

The physical characteristics of the Alfa-Aesar α and γ -Al₂O₃ particles were analyzed by scanning electron microscopy (SEM), energy dispersive x-ray fluorescence analysis (EDAX), mercury porosimetry and nitrogen BET surface area analysis. The SEM and EDAX analyses were performed at the Sevrin-Trent laboratory in Chelmsford, MA. SEM reveals the microscopic surface morphology of the particles, especially the changes in the surface morphology upon the sulfuric acid treatment. The EDAX assay, performed on the same samples as the SEM work, gives small-scale surface elemental analysis, which was used in this case to quantify the uptake of the sulfuric acid on the particles. Mercury porosimetry was performed at Porous

Materials Incorporated to quantify the size distribution of both the particles and the pores of the particles, as well as to provide an idea of the shape of the pores. N₂ BET analysis was performed in-house at PSI. SEM, EDAX, and BET analyses were performed for both the as-received and H₂SO₄-treated particle samples; mercury porosimetry was performed only for the as-received samples, as we expected that mercury would react with H₂SO₄ on the acid-treated samples. Owing to the small sample size, analysis of the shock-heated particles was limited to SEM and BET.

The mass fraction of H₂SO₄ taken up by the particle samples ranged from ~0 to 30% of the sample mass, depending on the particle type and the temperature of the treatment. A summary of the particle types and H₂SO₄ treatment results is given in Table 2. In general, the α -Al₂O₃ samples exhibited smaller BET surface areas than the γ -Al₂O₃ samples, and took up correspondingly smaller mass fractions of H₂SO₄ at a given treatment temperature. The larger H₂SO₄ uptake exhibited by both particle types at the higher temperature is probably a

Table 2. Particle Treatments and Activities for H₂SO₄ Vapor

Particle Type	Treatment	N ₂ BET Surface Area	H ₂ SO ₄ Uptake (% of sample mass)
α -Al ₂ O ₃	none	8.4 m ² /g	-
α -Al ₂ O ₃	135 C H ₂ SO ₄	8.3 m ² /g	< 2 %
γ -Al ₂ O ₃	none	61.7 m ² /g	-
γ -Al ₂ O ₃	135 C H ₂ SO ₄	58.3 m ² /g	16.4 %
α -Al ₂ O ₃	none	4.5 m ² /g	-
α -Al ₂ O ₃	165 C H ₂ SO ₄	2.0 m ² /g	12 %*
γ -Al ₂ O ₃	none	45 m ² /g	-
γ -Al ₂ O ₃	165 C H ₂ SO ₄	0.2 m ² /g	30 %*

* confirmed by EDAX analysis

consequence of the ~6-fold larger vapor pressure of H₂SO₄ at 165 C. We note that H₂SO₄ uptake by α -Al₂O₃ is considerably less facile than we previously observed for porous carbon particles, which took up 10-20% mass fractions at 120-140 C.^{37,38} However, the carbon particles had mass-specific surface areas in the range of ~1000 m²/g, over 100 times larger than the BET surface areas of the α -Al₂O₃ samples and almost 20 times larger than those of the γ -Al₂O₃ samples. Thus, on the basis of unit mass-specific surface area, both α -Al₂O₃ and γ -Al₂O₃ are considerably more active than carbon to uptake of H₂SO₄ vapor

The uptake of H₂SO₄ vapor by the Al₂O₃ particle samples results in drastic surface morphology changes, especially in the γ -alumina samples. Using SEM, we obtained images of

the surface morphology showing the surfaces of α - and γ - Al_2O_3 at two different magnifications, both before and after the treatment with sulfuric acid.

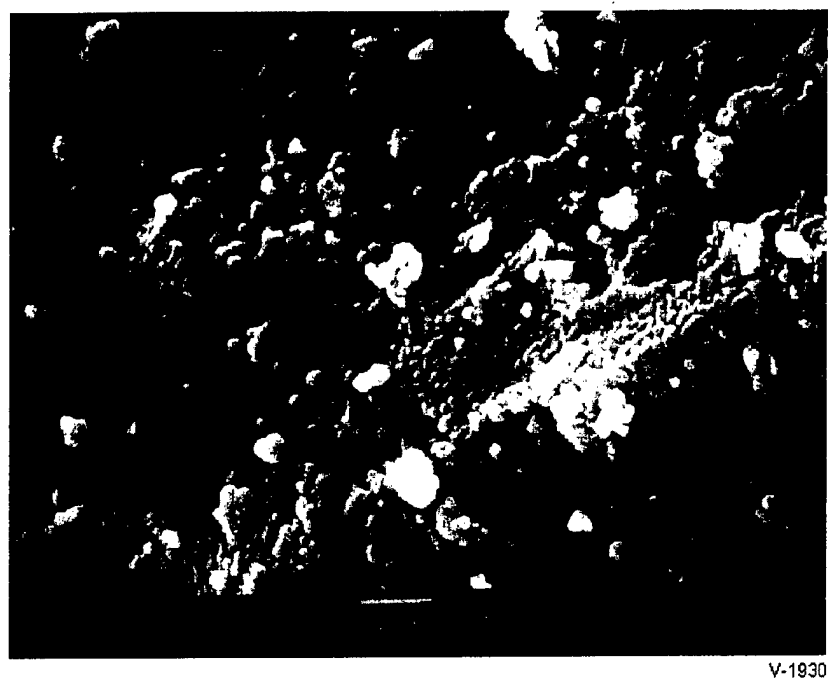
The two scanning electron micrographs in Figure 7 show pristine α - Al_2O_3 particles (as received from Alfa-Aesar) at two different magnifications. In Figure 7a, the white bar at the bottom of the photo is $1\text{ }\mu\text{m}$ and in Figure 7b, the white bar is 100 nm . It is clear from these pictures that, while the surface area of the bulk powder is not high, there is appreciable complexity in the surface morphology. When the α - Al_2O_3 is exposed to the acid vapors at 165 C for a period of three days, the appearance of the surface features is softened, as shown in Figure 8. Following H_2SO_4 treatment, the bulk surface area of these particles is reduced by a factor of two to $2\text{ m}^2/\text{g}$, likely due to pore filling by the adsorbed H_2SO_4 molecules. During the course of these analyses, the uptake of 12% mass fraction of H_2SO_4 was confirmed by the EDAX technique.

The next set of SEM results compares γ - Al_2O_3 without and with H_2SO_4 treatment. In the first pair of images, Figure 9, the complicated “rug-like” surface of the γ -alumina is shown, again at two magnifications. This sample has a BET surface area of $45\text{ m}^2/\text{g}$, nearly equivalent to the specifications from the manufacturer. When this sample is exposed to the acid treatment, as shown in Figure 10, the surface becomes quite smooth in appearance, and almost all visible surface roughness is gone. This fact is confirmed by the N_2 BET surface area, which has been reduced to $\leq 0.2\text{ m}^2/\text{g}$. This sample gained 30% mass fraction during processing, a value confirmed by sulfur measurements during the EDAX analysis.

Information provided by mercury porosimetry helps to illuminate the meaning of these data. Porosimetry is a technique used to give an indication of pore size and volume within a porous material. This is done by infiltrating a sample of the material with mercury using a controlled applied pressure. The pressure can be related to pore size using the assumption of cylindrical pores. Volume can be measured by forcing the mercury into the pores of the material while monitoring resistivity of a wire suspended in the mercury. As the mercury is pushed into the pores, the resistivity of the system is altered.

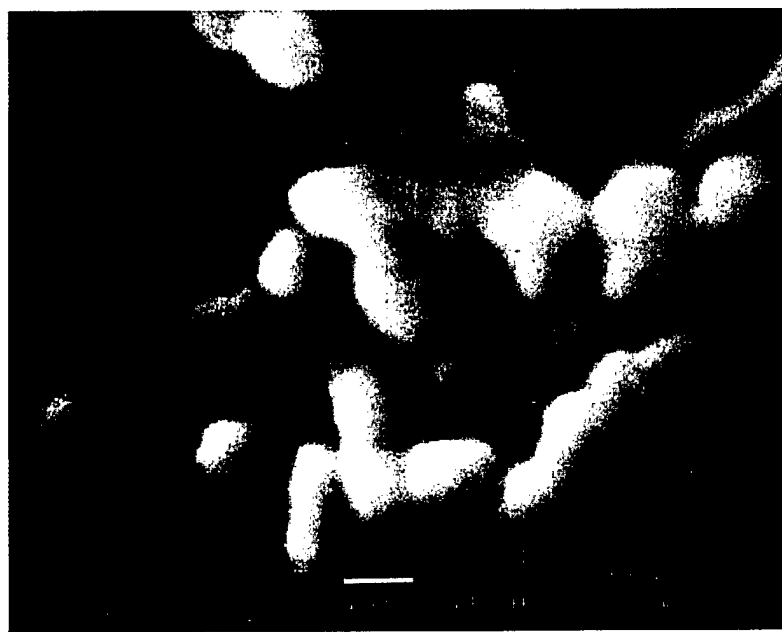
The porosimetry results reveal that the untreated α - Al_2O_3 sample has a total porosity of 31%, with a pore size distribution that peaks at $0.7\text{ }\mu\text{m}$ in diameter. This pore size corresponds to the overall surface roughness shown in Figure 7. Additionally, the BET surface area compares well with the surface area calculated from the porosimetry measurement, which is indicative of nearly cylindrical pores. Lastly, the density of the bulk powder was measured at 0.58 g/cm^3 , much less than the density of 3.97 g/cm^3 for bulk aluminum oxide.

Porosimetry results for the untreated γ - Al_2O_3 sample reveal a total porosity of 77%, with much smaller pores than are associated with the α sample. In the γ - Al_2O_3 sample, 89% of the pores are $\leq 60\text{ nm}$ in diameter. Additionally, the BET surface area is much smaller than the surface area based upon the porosimetry results, indicating “ink bottle” pores. This term describes pores that can contain much more internal volume than would be anticipated from an assumption of cylindrically-shaped pores. The density of this material was measured to be 0.45 g/cm^3 , which is also much less than the density of the bulk solid.



V-1930

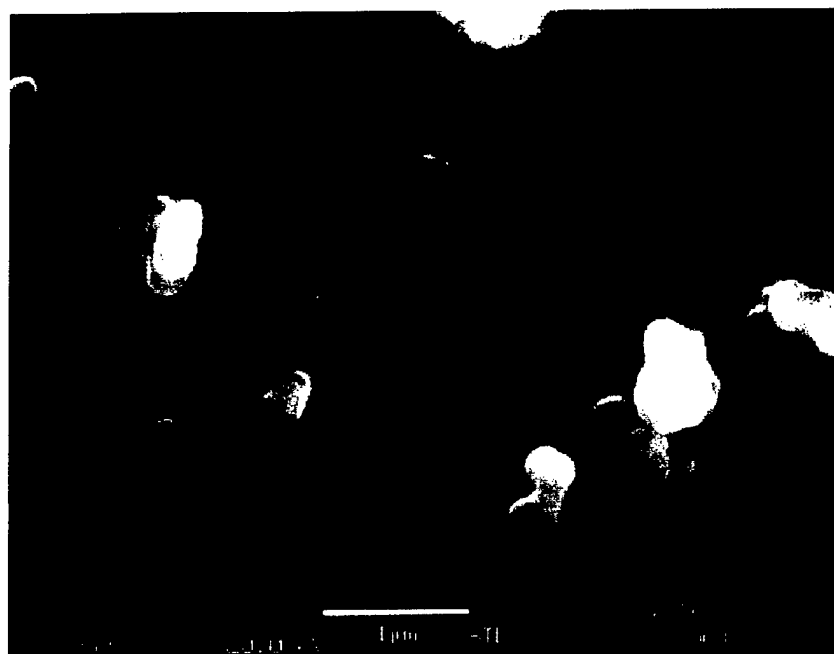
(a)



V-1765

(b)

Figure 7. SEM micrographs of untreated α -Al₂O₃ particle sample, $4.5 \text{ m}^2/\text{g}$.

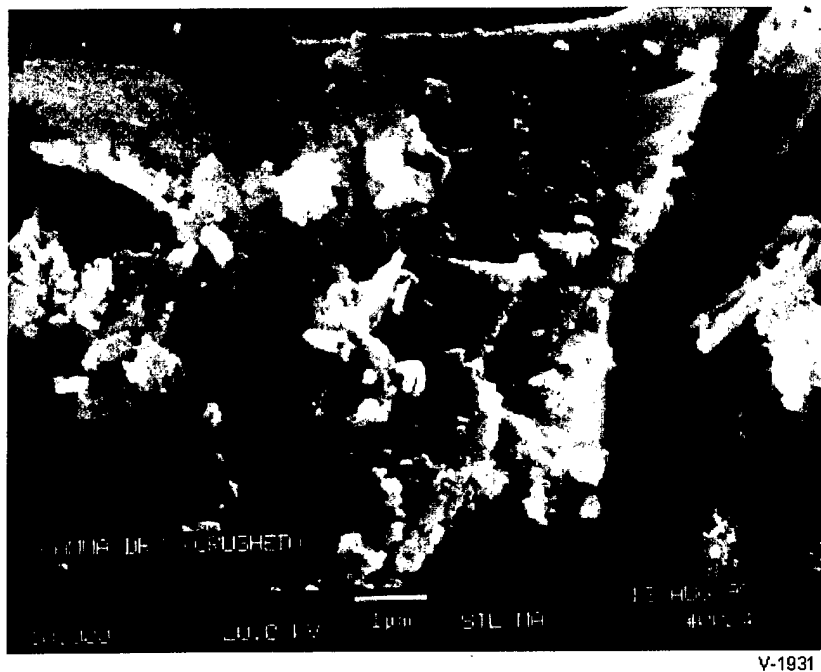


(a)

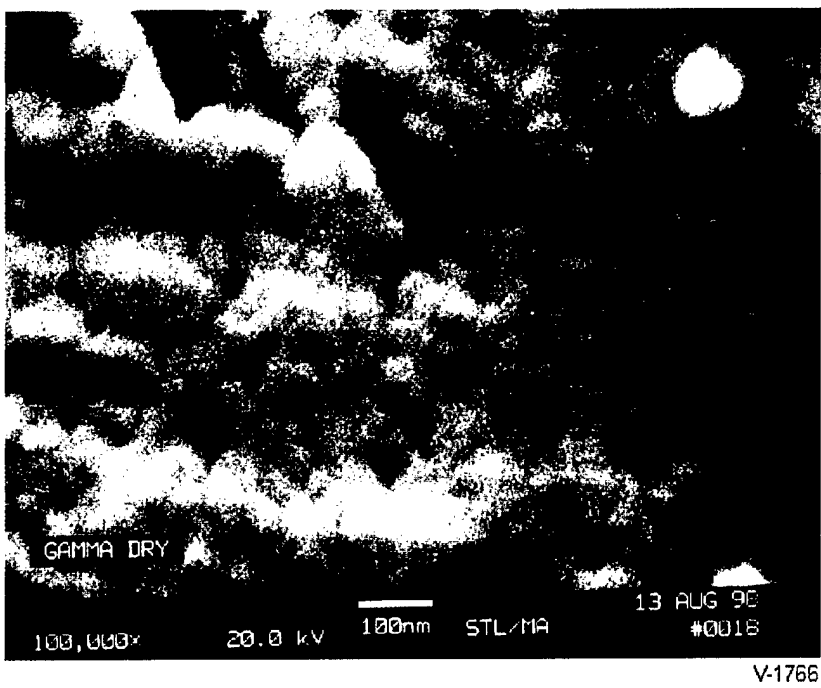


(b)

Figure 8. SEM micrographs of H_2SO_4 -treated $\alpha\text{-Al}_2\text{O}_3$ particle sample, $2.0 \text{ m}^2/\text{g}$.



(a)

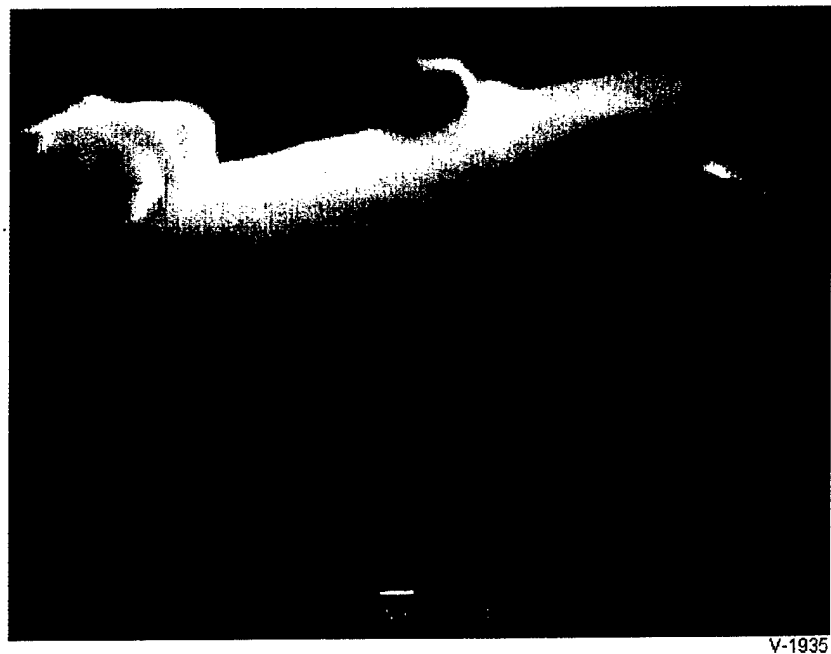


(b)

Figure 9. SEM micrographs of untreated γ -Al₂O₃ particle sample, 45 m²/g.



(a)



(b)

Figure 10. SEM micrographs of H_2SO_4 -treated $\gamma\text{-Al}_2\text{O}_3$ particle sample, $0.2 \text{ m}^2/\text{g}$.

The structure of the shock-heated particles is shown by the SEM image in Figure 11. As expected from the thermal recalcination process by which they were formed, these particles are more spherical than the commercially grown particles, and have much lower porosity and mass-specific surface area. The BET surface area of the shock-heated particle sample is $<0.3 \text{ m}^2/\text{g}$, similar to that of the H_2SO_4 -treated $\gamma\text{-Al}_2\text{O}_3$ sample.

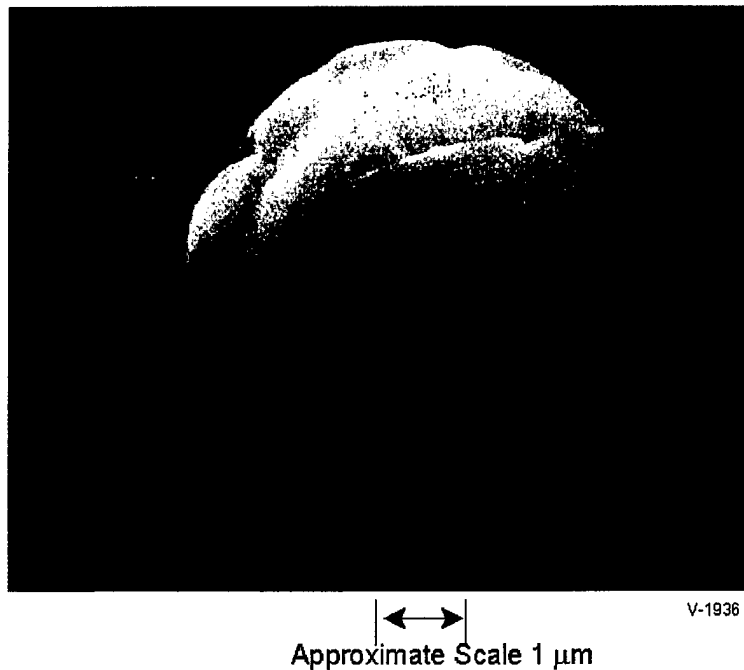


Figure 11. SEM micrograph of shock-heated aluminum oxide particle sample, $\leq 0.3 \text{ m}^2/\text{g}$.

4.2 Single-Particle Hydration Measurements: Virgin and H_2SO_4 -Treated Particles

In an initial series of single-particle quadrupole trap experiments, we compared the hydration behaviors of untreated particles and particles that had been exposed to H_2SO_4 vapor at 135 C. As discussed in Section 4.1, acid treatment at this temperature results in no measurable surface coverage by H_2SO_4 for the $\alpha\text{-Al}_2\text{O}_3$ particles and modest coverage for the $\gamma\text{-Al}_2\text{O}_3$ particles. In general, $\alpha\text{-Al}_2\text{O}_3$, H_2SO_4 -coated $\alpha\text{-Al}_2\text{O}_3$, and $\gamma\text{-Al}_2\text{O}_3$ particles exhibited no ($<1\%$) H_2O mass uptake upon prolonged exposure to high relative humidities. Typical particle sizes for these experiments were $\approx 20 \mu\text{m}$. In contrast, H_2SO_4 -coated $\gamma\text{-Al}_2\text{O}_3$ behaved quite differently. First, the bulk sample showed a 16.4% mass increase resulting from the H_2SO_4 vapor deposition treatment. Second, the single-particle H_2O uptake measurements showed $\approx 25\%$ mass uptake in a slow, irreversible process, and an additional $\approx 10\%$ mass uptake in a faster process as the relative humidity of the gas was varied from 0 to 70%. Unfortunately, these particles also tended to build up larger static charges during insertion into the trap, resulting in balancing voltages that precluded sizing of the particle by the spring point method. Hydration data for the inactive and active $\gamma\text{-Al}_2\text{O}_3$ particles are shown in Figures 12 through 14. These figures illustrate the variations in relative particle mass, as indicated by variations in the DC balance voltage, with

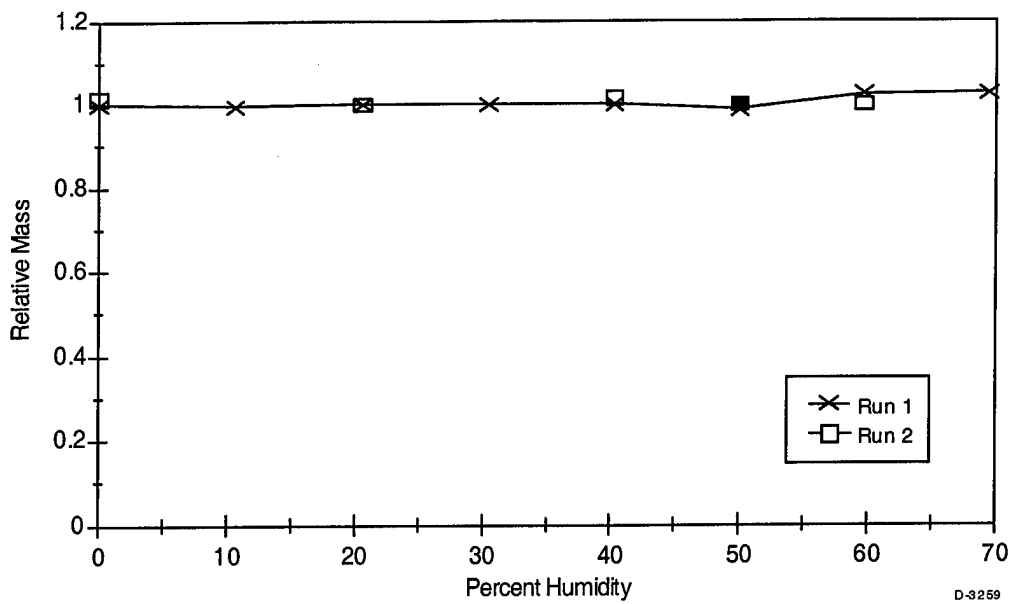


Figure 12. Relative particle mass versus relative humidity for a heat-treated Alpha Aesar γ - Al_2O_3 particle. The particle diameter determined by the spring point method is $13.2 \mu\text{m}$.

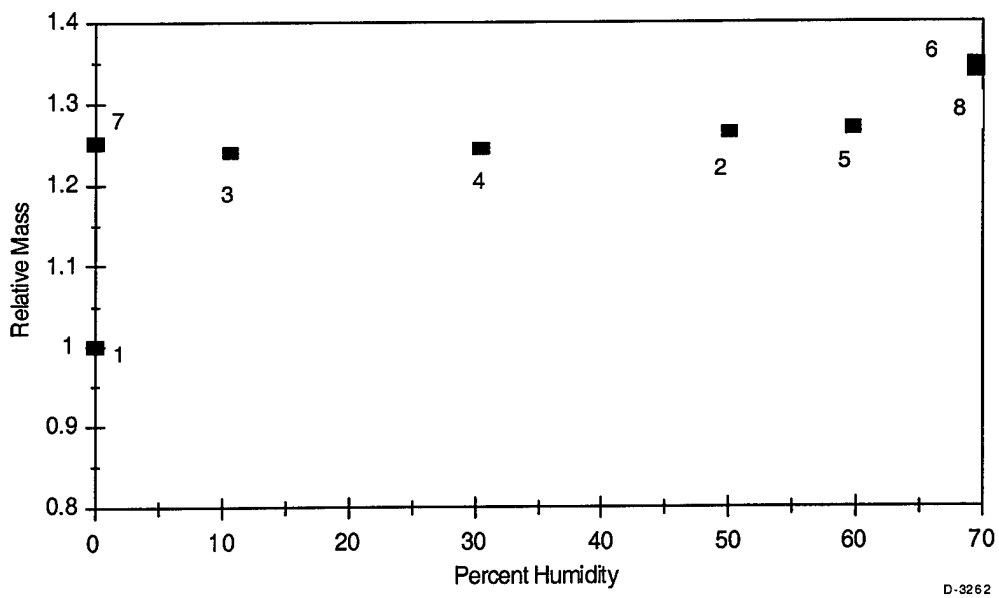


Figure 13. Relative particle mass versus relative humidity for an H_2SO_4 -treated Alpha Aesar γ - Al_2O_3 particle. The order in which the data points were determined is indicated by the number accompanying each data point.

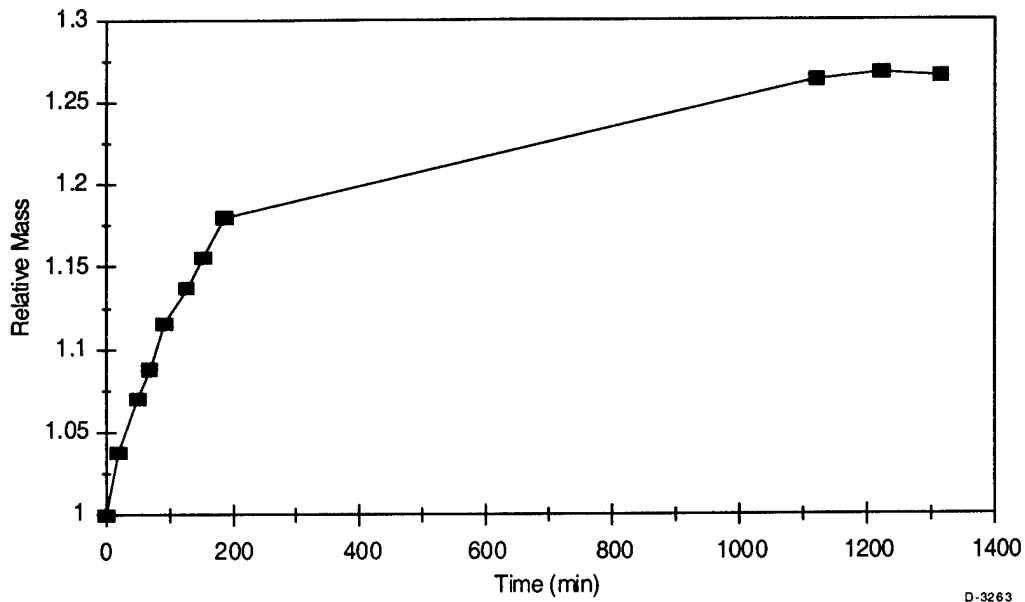


Figure 14. Relative particle mass versus time measured during the transition from 0 to 50% relative humidity for the H₂SO₄-treated Alpha Aesar γ-Al₂O₃ particle in Figure 13.

variations in relative humidity (RH). Figures 12 and 13 show variations in the steady-state particle mass at each RH; Figure 14 shows the time-dependent approach to steady-state for a fixed RH.

Analysis of the BET surface areas of bulk particle samples produced the following results. The α-Al₂O₃ particles had a specific surface area of 8.4 m²/g prior to H₂SO₄ vapor deposition treatment at 135 °C and 8.3 m²/g after treatment. This difference in surface area is not significant, so the particle surface area was not measurably affected by H₂SO₄ treatment at this temperature. Particle size analysis for the α-Al₂O₃ sample gave an area-weighted mean diameter,

$$D_{20} = (N_i d_i^2 / N_i)^{1/2},$$

of 55 μm. The γ-Al₂O₃ sample had a specific surface area of 61.7 m²/g prior to H₂SO₄ vapor deposition treatment and 58.3 m²/g after treatment. The area-weighted mean diameter for the sample, D₂₀, was 225 μm. The specific surface areas for the α and γ samples are 300 and 9200 times larger, respectively, than the mean spherical surface areas, indicating high surface roughness and, in the case of the γ sample, high internal porosity as well.

The α-Al₂O₃ sample showed an insignificant weight change following low temperature acid vapor treatment, indicating no measurable H₂SO₄ deposition. This corresponds to uptake of less than 2 × 10¹⁶ H₂SO₄ molecules, or less than 1% surface coverage. The mass of a single 20 μm Al₂O₃ particle is about 1.7 × 10⁻⁸ g, so our observation of no H₂O uptake to within ±1% of the particle mass signifies an H₂O mass uptake of <1.7 × 10⁻¹⁰ g, or <5.6 × 10¹² H₂O molecules.

However, for the nominal specific surface area of the sample, a single 20 μm particle should have roughly 1.4×10^{12} surface sites, so our measurement precision does not preclude the uptake of up to ~ 4 monolayers of H_2O by the untreated and treated $\alpha\text{-Al}_2\text{O}_3$ particles.

Similarly, for the untreated $\gamma\text{-Al}_2\text{O}_3$ (13 μm), we observe an H_2O mass uptake of $<4.8 \times 10^{11}$ g, or $<1.6 \times 10^{12}$ H_2O molecules. In this case, the higher specific surface area measured for the bulk sample suggests 3×10^{12} surface sites, giving a detection limit of ≈ 0.5 monolayer.

The bulk γ sample (20 mg) took up 3.3 mg upon exposure to sulfuric acid vapor, and lost 3.4 m^2/g of specific surface area. For the initial surface area, 20 mg comprises 1.2×10^{19} surface sites. The mass uptake, if entirely due to H_2SO_4 adsorption, corresponds to $\approx 2 \times 10^{19}$ H_2SO_4 molecules, equivalent to ≈ 2 monolayers. Some of this mass is likely also due to H_2O , so this estimate is an upper bound for H_2SO_4 and a lower bound for total molecular coverage. The occluded surface area corresponds to $\approx 7 \times 10^{17}$ surface sites. This suggests some degree of blockage of the smallest internal pores by H_2SO_4 molecules, preventing their penetration by the N_2 BET method.

Now we turn to the observed single-particle H_2O adsorption on H_2SO_4 -treated $\gamma\text{-Al}_2\text{O}_3$. Let us assume that the particle size was on the order of 20 μm . Following this assumption, the initial slow process results in adsorption of $\approx 1.4 \times 10^{14}$ H_2O molecules, while the subsequent faster process accounts for an additional $\approx 5 \times 10^{13}$ H_2O molecules; these are to be compared to $\approx 1 \times 10^{13}$ surface sites available.

The slow, irreversible H_2O uptake is characteristic of capillary condensation in nm-sized pores, where the curvature of condensed liquid surfaces reduces the saturation vapor pressure.³⁹ We have observed this phenomenon previously for H_2O condensation on porous carbon spheres.³⁸ For sufficiently small pores and small contact angles (i.e., small radius of curvature), H_2O can condense at partial pressures well below the equilibrium vapor pressure over a flat surface. The cylindrical capillary condensation criteria are given by

$$N_A kT \ln(RH) = -2M\gamma \cos\theta / \rho r \quad (3)$$

where N_A is Avogadro's number, k is Boltzmann's constant, RH is fractional relative humidity, M is molecular weight, γ is surface tension, θ is contact angle, ρ is density, and r is the critical pore radius giving condensation at relative humidity RH . Evaluation of this equation in the limit of small contact angle gives the maximum critical pore radius as a function of relative humidity. A computed curve for capillary condensation of H_2O at 300 K in the small contact angle limit is shown in Figure 15. The curve delineates the maximum pore radius at which capillary condensation can occur for a given RH . The onset of capillary condensation at $\approx 50\%$ relative humidity, as we observe, is consistent with a critical pore radius of ≈ 1.5 nm. This view is consistent with the SEM images and porosity measurements described in Section 4.1.

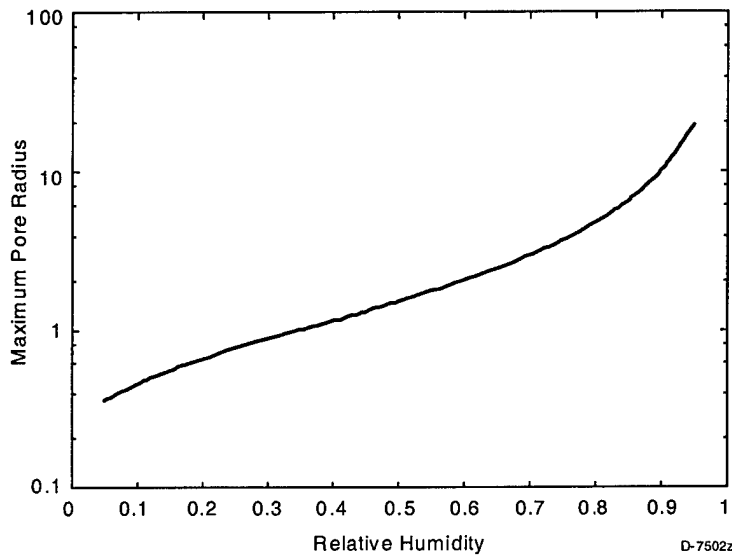


Figure 15. Computed limits for capillary condensation of H_2O in the small contact angle limit, 300 K.

The more efficient H_2O adsorption on sulfated particles at sub-saturated humidity levels appears to be due to solubility-induced adsorption of H_2O by H_2SO_4 adsorbed on the $\gamma\text{-Al}_2\text{O}_3$ surfaces. This is similar in character to the hydration behavior we have previously reported for H_2SO_4 -treated carbon particles.^{37,38} These data suggest the adsorption of several monolayer-equivalents of H_2O , or more than one H_2O molecule for every available adsorbed H_2SO_4 molecule. The data from both the bulk vapor deposition and the single particle hydration measurements are consistent with 1 to 2 monolayers of surface coverage by H_2SO_4 , as opposed to 0.2 to 0.4 monolayers of coverage inferred for carbon.^{37,38}

4.3 High-Temperature H_2SO_4 Treatment: Activity for H_2O and HCl

We have shown above that, during the lower-temperature sulfuric acid treatment, uptake of H_2SO_4 and the consequent activity of the particles for H_2O were very small, and were experimentally detectable only for the γ -alumina particles. The measurement sensitivity of these single-particle experiments is limited by the relatively small activated surface area of the particle. The high-temperature treatment results in much higher uptake of acid on the particles, due to the much higher vapor pressure of H_2SO_4 . In this case, the $\alpha\text{-Al}_2\text{O}_3$ particles experience a 12% weight increase during processing. A calculation based upon the measured percentage pore volume (31%) indicates that the pores in these particles are between 39 and 59% filled with sulfuric acid (assuming densities of 1.8 and 1.2 g/cm^3 , respectively, for the deposited sulfuric acid).

4.3.1 Activity of Virgin Particles

To establish a quantitative baseline activity for untreated particles, we suspended some pristine particles in the electrodynamic levitator and monitored their H₂O and HCl uptake over long time periods and as a function of temperature down to 190 K. The α -Al₂O₃ and γ -Al₂O₃ particles showed no measurable HCl uptake and slow, irreversible H₂O uptake.

An example hydration experiment is shown in Figure 16. Here an α -Al₂O₃ particle was exposed to a controlled flow of humid N₂ at room temperature over a 26-hour period. Particle mass was determined from the DC balance voltage, and particle aerodynamic diameter was determined from spring point measurements. Initially, the particle is about 7.9 ng and 24.7 μ m in diameter. Upon prolonged exposure at 30 to 40% relative humidity (RH), there is a slight increase in mass without a corresponding increase in diameter, suggesting H₂O uptake in internal pores. During exposure overnight at about 50% RH, the particle increases in both mass and diameter, and the H₂O uptake is irreversible as the RH is reduced to zero.

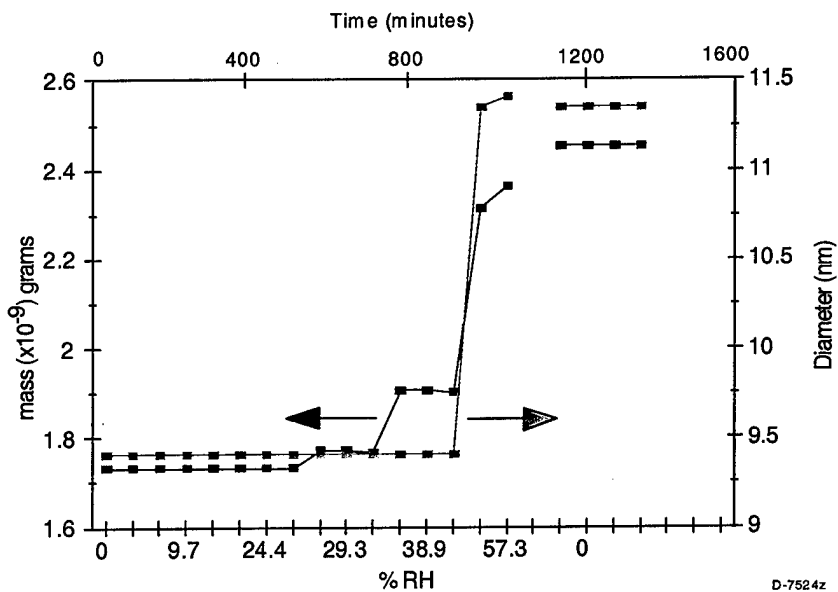


Figure 16. Single-particle total mass and diameter versus RH over a 26-hour period, 300 K, untreated α -Al₂O₃.

As before, the behavior exhibited in Figure 16 is consistent with capillary condensation in small pores, combined with irreversible chemisorption of H₂O. The onset of mass uptake at \approx 30% RH, with no concomitant increase in diameter, indicates capillary condensation in \approx 1 nm radius pores. The overall H₂O uptake is slow, probably because of diffusion into the small pores and because of occupation of most of the active sites by chemisorbed hydroxyl acquired from the ambient air prior to the experiments.

Temperature cycling experiments for particles in the presence of H_2O and HCl are illustrated in Figures 17 through 20. In Figures 17 through 19, the observed quantities are the AC spring point voltage, indicative of aerodynamic diameter, and the DC balance voltage, indicative of particle mass. For Figures 17 and 18, the H_2O content of the N_2 gas flow is <30 ppm (dew point <220 K); for Figure 19, the HCl content of the gas stream is 30 ppm. The cooling and warming rates are ≈ 1 K/min and ≈ 0.5 K/min, respectively, as depicted in Figure 19. In all cases, the DC voltage showed no significant changes in particle mass, and the changes in the AC spring point voltage are entirely attributable to the change in the viscosity of N_2 with temperature. Thus the activity of both α and γ Al_2O_3 toward H_2O and HCl uptake at low temperature is very low, probably because of hydroxylation of the active sites.

From the experimental data, we have evaluated H_2O and HCl uptake coefficients as the ratio of the observed uptake rate (molecules/s) to the gas-particle collision rate. The measurements give upper bound values of $\leq 1 \times 10^{-11}$, consistent with values observed on $\alpha\text{-Al}_2\text{O}_3$ single crystals by George and coworkers⁴⁰ for high OH coverage. They have reported sticking coefficients ranging from near-unity for the unhydroxylated surface to 10^{-10} or less for saturated OH coverage.⁴⁰ We conclude that, prior to admission of the particles to the trap, the surface sites are nearly saturated with chemisorbed OH acquired from H_2O in the room air, and additional gas uptake is severely inhibited as a result.

In an attempt to remove the OH from the particle surfaces, we irradiated suspended particles with a beam from a 5 W, cw CO_2 laser at $\approx 10.6 \mu\text{m}$. Based on the laser intensity, the computed absorption cross section of the particle, and cooling by radiative and conductive heat transfer, we estimated the temperature of the particle to be ≈ 750 K. According to the work of George and coworkers,⁴⁰ this should be sufficient to dehydroxylate the surface. However, we observed no mass change, and no significant increase in post-treatment H_2O uptake. This null

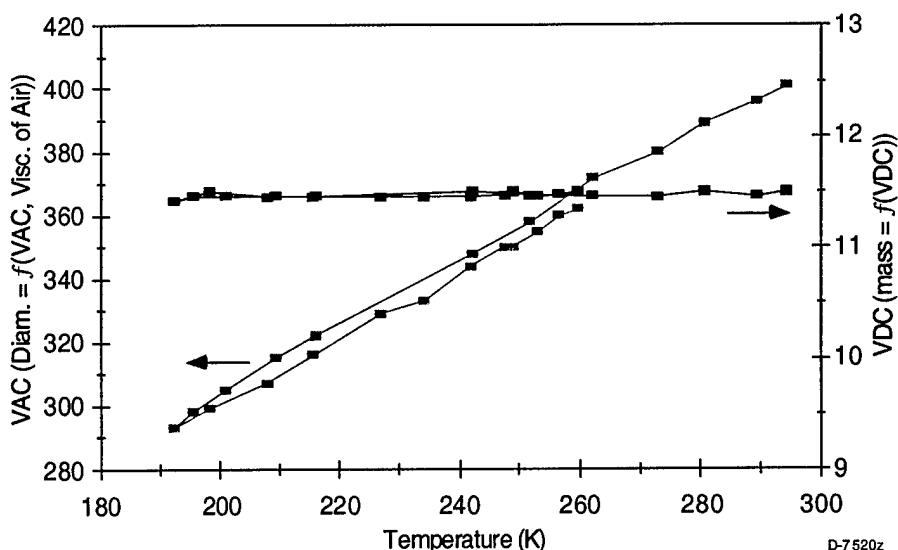


Figure 17. Temperature cycling, $\alpha\text{-Al}_2\text{O}_3$ particle, $28.9 \mu\text{m}$ diameter, <30 ppm H_2O in N_2 .

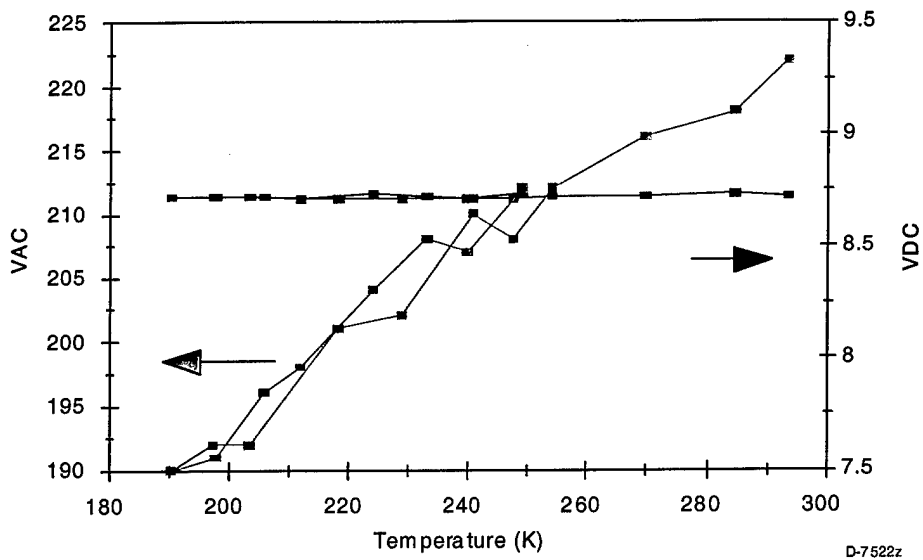


Figure 18. Temperature cycling, γ -Al₂O₃ particle, 37.1 μm diameter, <30 ppm H₂O in N₂.

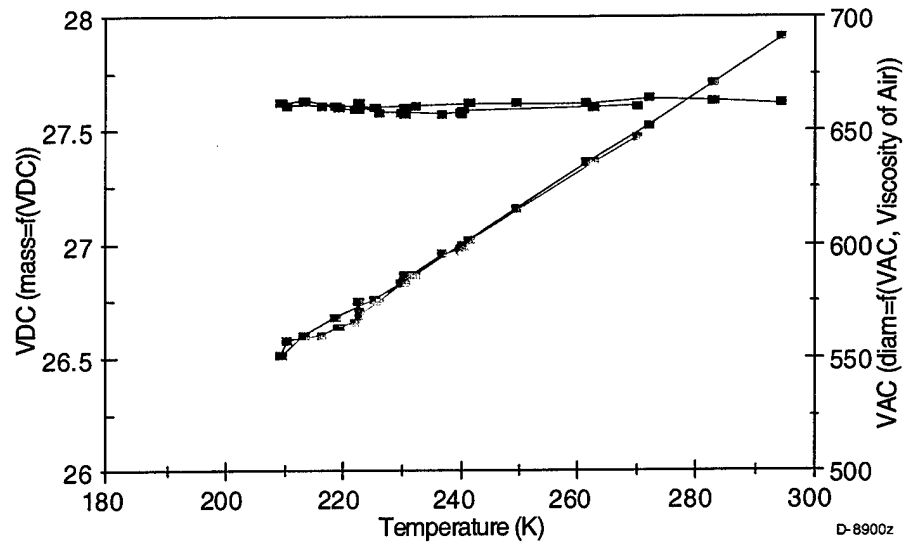


Figure 19. Temperature cycling with added HCl: α -Al₂O₃ ($d = 32.5 \mu\text{m}$) particle dosed with 30 ppm HCl during warming cycle.

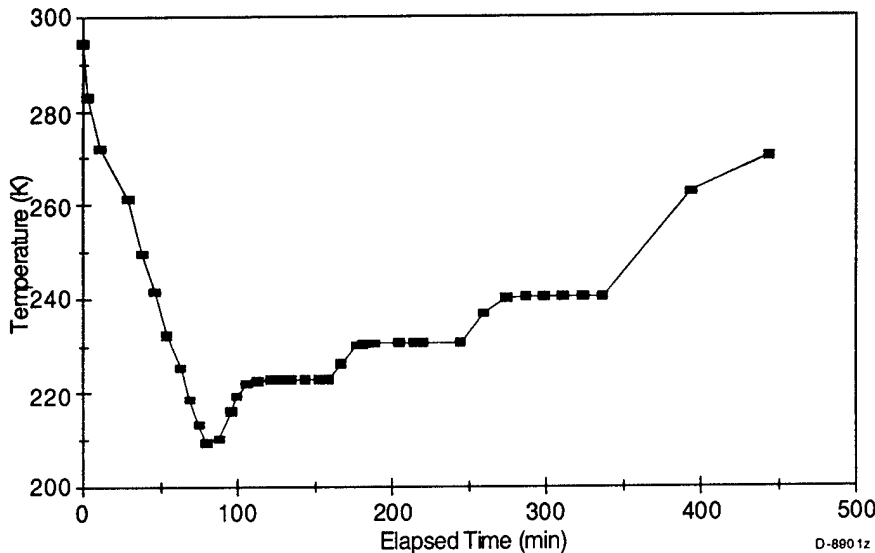


Figure 20. Time profile of dosing experiment in Figure 19.

result may be due to the short time scale for rehydroxylation at atmospheric pressure. Even in "dry" N_2 (≈ 30 ppm H_2O), at $\gamma = 0.1$, the time scale for rehydroxylation is on the order of milliseconds in the kinetics-controlled limit. Our conclusion is that OH coverage of Al_2O_3 surfaces limits their reactivity, both in the laboratory and in the expanding plume and ambient atmosphere.

4.3.2 Activity of H_2SO_4 -Treated and Shock-Heated Particles

Following exposure of the particles to H_2SO_4 vapor at 165°C, individual particles were inserted into the electrodynamic levitator, and were dosed first with H_2O vapor and then with HCl . Results for an H_2SO_4 -treated γ - Al_2O_3 particle are shown in Figure 21. The particle was initially dosed with H_2O at 50% relative humidity, resulting in mass increase as H_2O was adsorbed. Then the particle was dried at 0% RH overnight, with no mass change, signifying that the H_2O uptake is essentially irreversible. The H_2O -laden particle was then exposed to a flow containing 100 ppm HCl , resulting in additional mass increase due to adsorption of HCl . Continued observation revealed that the HCl uptake was also irreversible. Similar results were obtained for the H_2SO_4 -coated α - Al_2O_3 particles.

Gas uptake data for a shock-heated (metastable) aluminum oxide particle are shown in Figure 22. These particles were not treated with H_2SO_4 vapor. The activity of these particles was strikingly high, especially considering their lack of porosity and relatively small available surface area. Substantial mass gains were observed for uptake of both H_2O and HCl . As with the other particles, this mass uptake was essentially irreversible on time scales up to 3 days.

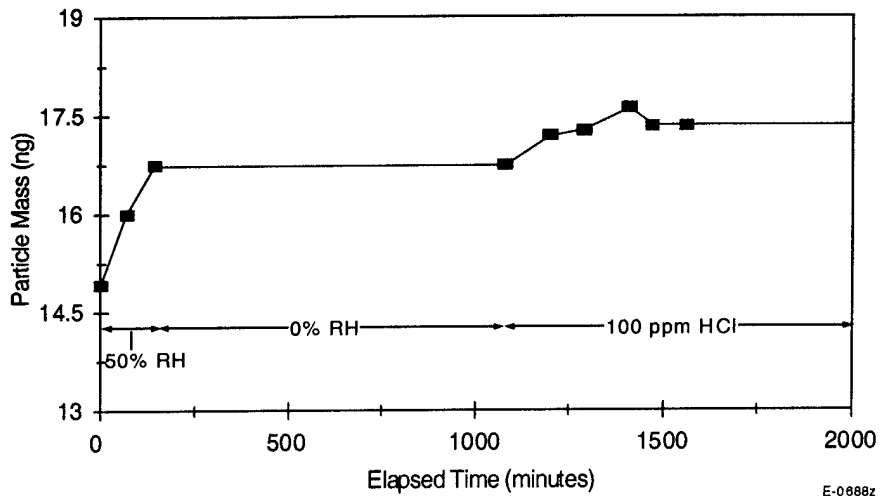


Figure 21. H₂O and HCl uptake on H₂SO₄-treated γ -Al₂O₃ particle at 298 K.

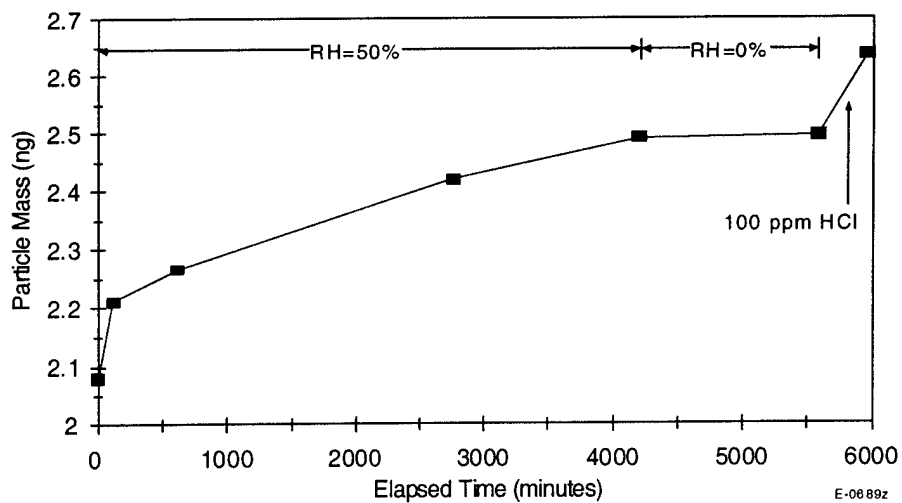


Figure 22. H₂O and HCl uptake on shock-heated metastable-phase aluminum oxide particle at 298 K

The gas uptake data were reduced to relative mass uptake rates, $\Delta m/m\Delta t$, and then to a sticking coefficient γ , defined as the ratio of the rates of adsorbing collisions and total collisions between the gas phase species and the particle surface:

$$\gamma = R_{\text{ads}}/R_{\text{tot}} \quad (4)$$

The total collision rate is given by the product of the particle surface area, the gas phase number density, and the average molecular velocity of the adsorbing species at the temperature of interest. The particle surface area is in turn given by the product of the particle mass and the mass-specific surface area A_s , resulting in the expression

$$R_{\text{tot}} = m_p A_s [H_2O(HCl)] \bar{v} \quad (5)$$

The particle mass is determined from the aerodynamic diameter (from spring point balancing), porosity, and bulk density:

$$M_p = \varphi \rho \pi D^3 / 6 \quad (6)$$

The collision rate for adsorbing collisions is given by the product of the relative mass uptake rate and the particle mass divided by the mass of a molecule (molecular weight/Avogadro's number):

$$R_{\text{ads}} = (\Delta m / m \Delta t) m_p N_A / M_{H_2O(HCl)} \quad (7)$$

In taking the ratio of the two collision rates, the particle mass cancels out, and the final expression is

$$\gamma = (\Delta m / m \Delta t) N_A / \{M_{H_2O(HCl)} A_s [H_2O(HCl)] \bar{v}\} \quad (8)$$

The values of γ determined in this manner are listed in Table 3. For the virgin α -Al₂O₃ and γ -Al₂O₃ particles, the activities were very low, $\gamma \sim 10^{-12}$ to 10^{-11} . Treatment with H₂SO₄ vapor increased the activities by three to four orders of magnitude. However, the most active particles were the shock-heated, metastable phase aluminum oxide particles, with $\gamma_{H_2O} = 1 \times 10^{-7}$ and $\gamma_{HCl} = 1 \times 10^{-8}$. In all cases, the uptake of water and hydrochloric acid was irreversible on the time scale of the experiments (up to 3 days).

Table 3. Summary of Single-Particle Gas Uptake Results

Particle Type	Reagent	Uptake Coefficient
α -Al ₂ O ₃	H ₂ O, HCl	10^{-11} to 10^{-12}
γ -Al ₂ O ₃	H ₂ O, HCl	10^{-11} to 10^{-12}
H ₂ SO ₄ -treated α -Al ₂ O ₃	H ₂ O	1×10^{-9} (diffusion limited)
H ₂ SO ₄ -treated γ -Al ₂ O ₃	H ₂ O	4×10^{-8} (diffusion limited)
H ₂ SO ₄ -treated γ -Al ₂ O ₃	HCl after H ₂ O saturation	1×10^{-9} (diffusion limited)
Metastable Al ₂ O ₃	H ₂ O	10^{-7} (kinetic limit)
Metastable Al ₂ O ₃	HCl after H ₂ O saturation	10^{-8} (kinetic limit)

5. DISCUSSION

5.1 Surface Chemistry

The observed particle activities cover a wide range, depending on the chemical nature of the particle surfaces. In investigations of single-crystal α -Al₂O₃(0001) surfaces, George and coworkers⁴⁰ found the H₂O sticking coefficient to depend strongly on the degree of surface coverage by chemisorbed hydroxyl (OH). They observed the H₂O sticking coefficient to vary from ~0.1 at low hydroxyl coverage to $<10^{-10}$ for essentially full OH coverage of the available surface sites. They interpreted these results in terms of a kinetic model in which gas phase H₂O adsorbs onto the Al₂O₃ surface and then dissociates to form chemisorbed OH, where the oxygen end of the OH is bonded to an –Al– site on the top layer. Based on these results, we expect Al₂O₃ surfaces at room laboratory conditions to be essentially saturated with chemisorbed OH. In addition, a dehydroxylated surface would rapidly become saturated again within milliseconds upon exposure to even the low-RH conditions within our apparatus. This accounts for our observation of very low sticking coefficients for H₂O and HCl on the virgin particles. Based on the SEM and porosity analyses, the small amount of H₂O uptake we observed for these particles is probably due to capillary condensation in the small pores as discussed in Section 4.2. The irreversibility of the uptake in a dry environment is characteristic of that process.

On the other hand, the α -Al₂O₃ and γ -Al₂O₃ particles are quite active toward H₂SO₄ uptake, which greatly increases their activity towards H₂O and HCl. H₂SO₄ may be taken up by ordinary condensation on the particles, but may also be physically or chemically adsorbed or condensed in the small pores. The significantly greater activity (per unit mass-specific surface area) compared to carbon^{37,38} suggests chemisorption. It is not clear what role the OH groups on the surface might play in this process. In any event, once the surfaces are covered with H₂SO₄, uptake of H₂O and subsequently of HCl are facilitated by solvation in the H₂SO₄ layer, as we have previously observed for carbon.^{37,38} Again, we observe the uptake to be irreversible, suggesting that much of the solvation occurs in small pores which are partially filled with H₂SO₄. Based on the mass gain upon exposure to H₂SO₄ vapor, we estimate as much as 10 to 15% of the pore volume may be filled with condensed H₂SO₄. The observed uptake coefficients of 10⁻⁹ to 10⁻⁸ are consistent with diffusion-limited reaction rates within pores in the 1 to 10 nm size range. The actual uptake coefficient for a non-porous particle could be substantially larger than the measured values, perhaps near unity. Thus it is likely that the uptake rates we observe for these porous, commercially manufactured particles are limited by diffusion of the species into the internal pore structure, and therefore represent lower bounds to the actual kinetic uptake rates.

The apparently high activity of the shock-heated metastable aluminum oxide particles is moderated by the fact that these particles are essentially non-porous. The observed values of $\gamma_{\text{H}_2\text{O}} \sim 10^{-7}$ and $\gamma_{\text{HCl}} \sim 10^{-8}$ appear to represent the actual kinetic limits for uptake on this surface. These values are much greater than those observed for α -Al₂O₃ and γ -Al₂O₃, but are probably much less than the actual kinetic limits for the H₂SO₄-coated particles. Based on the results of George and coworkers⁴⁰ for single-crystal α -Al₂O₃(0001) surfaces, the uptake coefficient we observe for H₂O corresponds to the surface activity expected for about 30% of the saturation OH coverage on α -Al₂O₃(0001). This suggests that more –Al– sites are available on the surface of

the metastable structure, and/or that its propensity for chemisorption of OH is much lower. The former possibility is consistent with our expectation that the metastable phase is oxygen-deficient. However, our observation that the species uptake on even this non-porous surface is irreversible suggests that chemisorption plays a key role.

5.2 Atmospheric Significance

Rocket-exhausted aluminum oxide particles are likely to be non-porous spheres, as they solidify from molten droplets that are formed in the combustion chamber. The phase into which the particles solidify is unknown, but may well be similar to the metastable phase that was formed in our shock tube simulation of the exhaust nozzle expansion process. Some, if not all, of these particles pass through the afterburning volume, where they may be converted to the α and possibly γ phases. The surfaces of these particles will be rapidly hydroxylated to saturation levels, inhibiting their reactivities with ambient plume and atmospheric species. For example, at 18 km altitude, a representative ambient H_2O concentration is 8.8×10^{12} molecules/cm³ (4 ppmv) at 215 K, giving a thermal molecular flux of 4.4×10^{17} cm⁻²s⁻¹. For a non-porous, spherical aluminum oxide particle 100 nm in radius, the H_2O collision rate with the surface is 5.6×10^8 s⁻¹. From the results of George and coworkers,⁴⁰ the time scale for hydroxylation of an initially “clean” surface by ambient H_2O to 40% of the saturation level of $\alpha\text{-Al}_2\text{O}_3(0001)$ is \sim 1.2 hours for this particle size. From the uptake coefficients we observe for $\alpha\text{-Al}_2\text{O}_3$ and $\gamma\text{-Al}_2\text{O}_3$ particles, the time required for H_2O uptake equivalent to 1 monolayer coverage of a 100 nm diameter particle is greater than 7 years, well in excess of the residence time of the particle (\sim 1 year/km at 18 km, and scaling as D_p^{-2}). In contrast, the H_2O monolayer-uptake time scale for a 100 nm diameter particle is \sim 6 hours for metastable aluminum oxide, <26 days for H_2SO_4 -treated $\alpha\text{-Al}_2\text{O}_3$, and <16 hours for H_2SO_4 -treated $\gamma\text{-Al}_2\text{O}_3$, for typical ambient H_2O concentrations. In the actual rocket exhaust plume, where rocket-emitted H_2O concentrations are two to three orders of magnitude larger than ambient, H_2O uptake on metastable and H_2SO_4 -coated particles would occur much more rapidly, i.e. well within the lifetime of the plume.

Our observation of greatly enhanced HCl uptake by metastable aluminum oxide particles is intriguing. If the surface chemistry of these particles is more representative of solid rocket exhausts than that of $\alpha\text{-Al}_2\text{O}_3$, then chlorine activation on non-sulfated solid rocket exhaust particles may be even more facile than previously thought.^{8,41,42} To further investigate this possibility, it will be essential to capture samples of rocket-exhausted aluminum oxide particles at high altitude for subsequent laboratory analysis and kinetics measurements.

Molina et al⁸ observed chlorine activation (Reaction (1)) on hydroxylated $\alpha\text{-Al}_2\text{O}_3$ surfaces to be over two orders of magnitude more efficient than on sulfuric acid surfaces, and suggested that H_2SO_4 -covered aluminum oxide particles would be inert to chlorine activation due to the low solubility of HCl in H_2SO_4 . Based on our observations, rocket-exhausted aluminum oxide particles are quite active toward H_2SO_4 uptake, and will gradually accumulate H_2SO_4 from the ambient atmosphere. Perhaps more importantly, aluminum oxide particles emitted from the solid rocket boosters on solid-boosted kerosene/LOx rockets will be exposed to high concentrations of H_2SO_4 emitted from the liquid-fueled motor. Kerosene is a multi-component hydrocarbon fuel which contains some amount of fuel-bound sulfur, depending on its refinement

history and additives. During combustion, the fuel-bound sulfur is completely oxidized into SO₂. A fraction of the SO₂ is further oxidized in the exhaust to eventually form supersaturation levels of H₂SO₄ vapor. The H₂SO₄ vapor undergoes both homogeneous and heterogeneous condensation. Normally, the heterogeneous condensation occurs on carbonaceous soot particles which are also emitted in the hydrocarbon combustion process, however aluminum oxide particles emitted by the solid-fuel boosters are much more abundant in the exhaust plume. We expect that most, if not all, of the aluminum oxide particles emitted from the boosters will be rapidly coated with monolayer levels of H₂SO₄ on the ~1-hour time scale of the near-field plume.

Our observation of enhanced HCl uptake on the H₂SO₄-treated particles contrasts with expectations based on the low solubility of HCl in bulk H₂SO₄, as discussed by Molina et al.⁸ However, the observed HCl uptake occurs after the particle has been dosed with H₂O, and may be more representative of HCl solvation in dilute H₂SO₄/H₂O mixtures. Alternatively, the interaction we have observed may not be analogous to the solvation of HCl in bulk aqueous H₂SO₄ solutions, but rather may be the interaction of HCl with near-monolayer coverage of chemisorbed, hydrated sulfate species. In any case, the interaction of HCl with H₂SO₄-coated aluminum oxide particles in a high-H₂O environment as in our experiments is similar to the phenomena that will occur in mixed-propellant rocket plumes. The potential for this process to promote heterogeneous chlorine activation requires further investigation. In addition, the H₂SO₄-coated particles may be active to uptake of HNO₃, and could serve to sequester HNO₃ generated in the exhaust plume. The development of compound HNO₃/HCl/H₂O/H₂SO₄/Al₂O₃ aerosols in rocket plumes could have significant implications for the long term atmospheric denitrification and chlorine activation within the plume-perturbed air parcels as they evolve and are transported poleward.

By analogy to the effects we have previously observed for carbon particles,^{37,38} the activation of aluminum oxide particles by monolayer coatings of H₂SO₄ can enable them to act as cloud condensation nuclei (CCN) as the plume-perturbed air parcel evolves. This effect can be considered in terms of the Köhler theory, which describes critical supersaturation behavior for spherical aerosols.⁴³ This theory applies to the limit of dilute solvent/H₂O mixtures, and provides useful guidelines for relating the laboratory results to atmospheric aerosol growth phenomena. Sub-monolayer coverage of an inert core by a water-soluble substance impacts the sub-saturation hydration behavior of the compound aerosol, as shown in our experiments, and also reduces the critical supersaturation level at which initially small aerosols will grow without bound to form cloud droplets. For a spherical insoluble core whose surface is coated with a small amount of water-soluble material, the saturation as a function of particle radius is given by:

$$\ln S = \frac{A}{a} - \frac{B}{(a^3 - r_u^3)} \quad (9)$$

where S is the saturation (or relative humidity), a is the drop radius, and r_u is the radius of the insoluble core. The terms A and B are constants given by:

$$A = \frac{2M_w \sigma_{w/a}}{RT \rho_w} = \frac{3.3 \times 10^{-5}}{T} \quad (10)$$

$$B = \frac{3vm_s M_w}{4\pi M_s \rho_w} = \frac{4.3 vm_s}{M_s}$$

where M_w and M_s are the molecular weights of water and solute, m_s is the mass of solute, ρ_w is the density of liquid water, $\sigma_{w/a}$ is the surface tension of water vs air, and v is the number of ions into which the solute dissociates upon solvation. Using Eq. (9), we can calculate Köhler growth curves for different solute coverages, as illustrated in Figure 23 for a particle with initial radius of 60 nm. To conveniently illustrate the small amounts of solute required, the solute coverages in these calculations are expressed in terms of fractions of a monolayer. The maxima in these curves define the critical supersaturations required for particle growth without bound. Particles whose critical supersaturation levels are below 1% ($S < 1.01$) are generally regarded as cloud condensation nuclei (CCN).

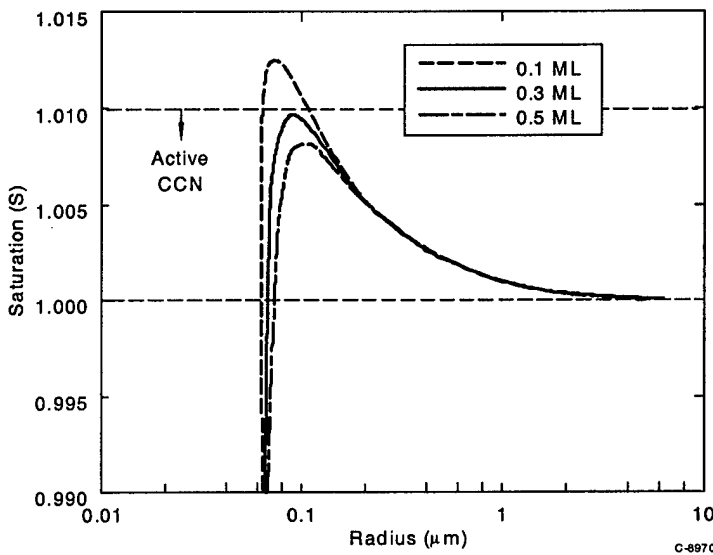


Figure 23. Köhler curves for the hydration growth of a spherical H_2SO_4 -coated aluminum oxide particle with initial radius of 60 nm and solute coverages of 0.1, 0.3, and 0.5 monolayer (ML).

The curves in Figure 23 illustrate the effects of solute coverage on critical supersaturation behavior. For a given initial particle size, increasing amounts of solute on the particle reduce the critical supersaturation level, eventually enabling CCN behavior. For smaller initial particle sizes, the critical supersaturation for a given coverage is higher, and correspondingly larger solute coverages are required to enable CCN behavior. To illustrate the particle size effect, the dependence of critical supersaturation on solute coverage for selected initial particle sizes is

shown in Figure 24. Clearly, initial particle radii smaller than about 40 nm require solute coverages in excess of one monolayer to become CCN. The experimental measurements reported here indicate a typical H_2SO_4 coverage on the order of 1 monolayer-equivalent, suggesting that aluminum oxide with initial radii larger than about 40 nm may contain enough H_2SO_4 to become CCN, given sufficient levels of H_2SO_4 in the plume. This is a substantial fraction of the emitted Al_2O_3 surface area.⁹ Thus, it is likely that rocket-exhausted aluminum oxide particles will act as CCN following exposure to H_2SO_4 vapor.

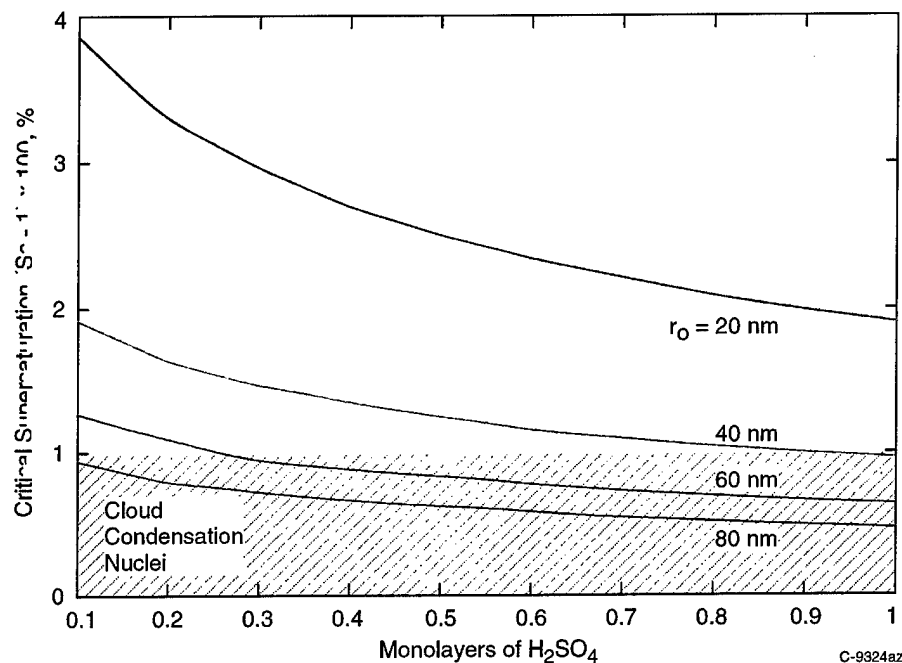


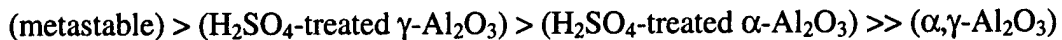
Figure 24. Köhler critical supersaturations as functions of surface coverage for spherical H_2SO_4 -coated aluminum oxide particles with initial radii of 20, 40, 60, and 80 nm.

6. CONCLUSIONS

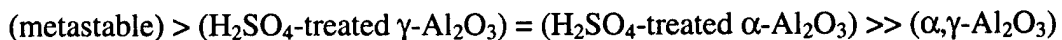
To summarize the experimental results, we have used a single-particle electrodynamic levitation technique to investigate the activities of different types of aluminum oxide particles for uptake of gas-phase H_2O and HCl , with relevance to the atmospheric impacts of solid rocket exhaust emissions. The particle types investigated were α - Al_2O_3 , γ - Al_2O_3 , H_2SO_4 -treated α - Al_2O_3 , H_2SO_4 -treated γ - Al_2O_3 , and metastable aluminum oxide formed by rapid solidification from molten Al_2O_3 in a shock tube, analogous to particle processing in a rocket exhaust nozzle. Particles were treated with H_2SO_4 by vapor deposition in an oven. The kinetic measurements consisted of independent, simultaneous observations of mass uptake and particle size increase upon exposure of single particles to fixed concentrations of H_2O or HCl in slowly flowing gas mixtures at 1 atm and temperatures from 300 K to 190 K. The α - Al_2O_3 and γ - Al_2O_3 particles were obtained from commercial sources, and were highly porous with pore diameters ranging

down to the nm scale, resulting in determinations of diffusion-limited uptake efficiencies which are lower bounds to the actual kinetic values. The metastable particles were spherical and non-porous, resulting in determinations of kinetically limited uptake efficiencies.

We observed apparent gas uptake efficiencies for H₂O at room temperature ranging from ~10⁻¹² to 10⁻⁷, with the activity order:



Similarly, the measured gas uptake efficiencies at room temperature for HCl (after H₂O dosing) ranged from ~10⁻¹² to 10⁻⁸, in the order:



The commercial $\alpha, \gamma\text{-Al}_2\text{O}_3$ particles were essentially inert to H₂O and HCl gas uptake except for capillary condensation in the small pores, but readily took up H₂SO₄ vapor at monolayer-equivalent levels. The adsorption of H₂SO₄ activated the uptake of H₂O and subsequent uptake of HCl, which proceeded at rates consistent with diffusion into the pores followed by rapid reaction on the internal surfaces. Due to the diffusion limitations, it is quite possible that the kinetic limits for activated H₂O and HCl uptake on the H₂SO₄-treated particles are significantly greater than the kinetically limited uptake efficiencies observed for the metastable particles. Uptake of H₂O and HCl was irreversible for all particle types, indicating trapping within the pores and/or chemisorption.

Consideration of the experimental results leads to some intriguing implications for the atmospheric effects of solid rocket exhaust particles. While current levels of rocket-exhausted aluminum oxide particles in the lower stratosphere are very small compared to the global atmospheric aerosol budget, these levels could increase substantially over the next few decades as rocket launch activities increase. In addition, the exhaust products from a given launch may persist at elevated concentrations for hours to days in plume-perturbed air parcels, resulting in localized chemical processing as the material mixes with ambient air and/or is transported poleward. Our general conclusions and suggestions are as follows:

- (1) Atmosphere-exposed $\alpha, \gamma\text{-Al}_2\text{O}_3$ particles are essentially inert to H₂O uptake, probably because of extremely rapid hydroxylation of the available surface sites even at low atmospheric humidities. Freshly emitted particles will be fully hydroxylated by rocket-exhausted H₂O within the first few seconds of the plume lifetime. The time scale for H₂O uptake on a hydroxylated $\alpha, \gamma\text{-Al}_2\text{O}_3$ particle in the lower stratosphere exceeds the particle residence time, so these particles are not expected to act as CCN.
- (2) Metastable aluminum oxide particles are 3 to 4 orders of magnitude more active than $\alpha, \gamma\text{-Al}_2\text{O}_3$ particles for uptake of H₂O and HCl. If these particle surfaces are similar to those produced by expansion from solid rocket engines at high altitudes, then rocket-exhausted aluminum oxide particles may be more active for heterogeneous chlorine activation chemistry than previously thought.

- (3) For a given ratio of surface area to mass, $\alpha,\gamma\text{-Al}_2\text{O}_3$ particles are 1 to 2 orders of magnitude more active than carbon for uptake of H_2SO_4 vapor at monolayer-equivalent levels. It is likely that aluminum oxide particles in the exhaust plumes of solid-boosted kerosene/LOx rockets will adsorb H_2SO_4 vapor generated from fuel-bound sulfur in the hydrocarbon fuel. This will substantially alter their short-term and long-term chemical effects.
- (4) The presence of monolayer-equivalent levels of H_2SO_4 on $\alpha,\gamma\text{-Al}_2\text{O}_3$ particles activates them for uptake of H_2O and of HCl on H_2O -dosed particles. The enhanced activity for H_2O indicates that sulfate-coated aluminum oxide particles may act as cloud condensation nuclei. The enhanced HCl uptake suggests the possibility for enhanced activity for heterogeneous chlorine activation in the humid rocket plume environment. In addition, sulfate-coated aluminum oxide particles may be active for uptake of HNO_3 , and could thus serve as sites for heterogeneous denitrification and chlorine activation processes analogous to the behavior of polar stratospheric cloud aerosols; this would be especially important in the short-term and long-term evolution and fates of rocket-perturbed stratospheric air parcels.

Our results point to several key issues that still need to be addressed in order to more fully assess the atmospheric effects of rocket-exhausted aluminum oxide particles. Perhaps most important of these is a clear determination of the phase and surface activity characteristics of the particles which are actually deposited in the lower stratosphere by the rocket exhaust and after-burning processes. This requires direct sampling and retrieval of particles at high altitude following deposition by a solid-fueled rocket. Another key research direction is to further investigate the activity of (non-porous) aluminum oxide surfaces that have been exposed to H_2SO_4 vapor. In particular, it is important to determine the true kinetic limits for uptake of H_2O , HCl , and HNO_3 , the reaction efficiencies for chlorine activation on hydrated and nitrated particles, and their propensity for psc-like behavior.

7. REFERENCES

1. B.C. Kruger, "Ozone depletion in the plume of a solid-fueled rocket," *Ann. Geophysicae* **12**, 409 (1994).
2. M. Yu. Danilin, "Local stratospheric effects of solid-fueled rocket emissions," *Ann. Geophysicae* **11**, 828 (1993).
3. M.R. Denison, J.J. Lamb, W.D. Bjorndahl, E.Y. Wong, and P.D. Lohn, "Solid rocket exhaust in the stratosphere: plume diffusion and chemical reactions," Proc. 28th Joint Propulsion Conference and Exhibit, Nashville, TN, 6-8 July 1992.
4. M.J. Prather, M.M. Garcia, A.R. Douglass, C.H. Jackman, M.K.W. Ko, and N.D. Sze, "The Space Shuttle's impact on the stratosphere," *J. Geophys. Res.* **95**, 18583 (1990).
5. R.P. Turco, O.B. Toon, R.C. Whitten, and R.J. Cicerone, "Space Shuttle ice nuclei," *Nature* **298**, 830 (1992).
6. B.C. Lippens and J.J. Steggerda, "Active Alumina," in Physical and Chemical Aspects of Adsorbents and Catalysts, B.G Linsen, Ed., Academic Press, New York, 1970, pp. 171-211.
7. G.N. Robinson, A. Freedman, C.E. Kolb, and D.R. Worsnop, "Decomposition of halomethanes on α -alumina at stratospheric temperatures," *Geophys. Res. Lett.* **21**, 377, (1994).
8. M.J. Molina, L.T. Molina, R. Zhang, R.F. Meads, and D.D. Spencer, "The Reaction of ClONO₂ with HCl on Aluminum Oxide," *Geophys. Res. Lett.* **24**, 1619 (1997).
9. M.N. Ross, P.D. Whitefield, D.E. Hagen, and A.R. Hopkins, "In Situ Measurement of the Aerosol Size Distribution in Stratospheric Solid Rocket Motor Exhaust Plumes," *Geophys. Res. Lett.* **26**, 819 (1999).
10. R.A. Reed and V.S. Calia, "Review of aluminum oxide rocket exhaust particles," AIAA-93-2819, AIAA 28th Thermophysics Conference, Orlando, FL, July 6-9, 1993.
11. T. E. Parker, R. R. Foutter, J. C. Person, and W. T. Rawlins, "High Temperature Optical Properties of Particulates Exhausted from Rockets," AL-TR-89-063, Astronautics Laboratory (AFSC), Edwards AFB, CA 93523-5000, November 1990.
12. T. E. Parker, R. R. Foutter, J. C. Person, and W. T. Rawlins, "Experimental Measurements of the Optical Properties of Al₂O₃ and Rocket Exhaust Particles at High Temperatures," 18th JANNAF Exhaust Plume Technology Subcommittee Meeting, Monterey, CA, November 1989.

13. W. T. Rawlins, R. R. Foutter, and T. E. Parker, "Effects of Supercooling and Melt Phenomena on Particulate Radiation in Plumes," PSI-TR-1136, Physical Sciences Inc., Final Report to NASA/MSFC under Contract NAS8-38885, July 1991.
14. W. T. Rawlins, R. R. Foutter, and T. E. Parker, "Infrared Radiative Properties of Rapidly Cooling, Initially Molten Al_2O_3 Particles," AIAA 93-2822, AIAA 28th Thermophysics Conference, Orlando, FL, July 1993.
15. W.T. Rawlins, H. Du, R.R. Foutter, and T.E. Parker, "Experiments to determine the effects of atmosphere on the index of refraction of molten alumina (Al_2O_3)," Tech. Rep. PSI-2223/TR-1272, Final Report for Subcontract No. 250-1-S2, Contract No. NASA8-39235, Physical Sciences Inc., September 1993.
16. C.G. Levi, V. Jayaram, J.J. Valencia, and R. Mehrabian, "Phase Selection in Electrohydrodynamic Atomization of Alumina," *J. Mater. Res.* 3, 969 (1988).
17. S.M. Oliver and R.A. Reed, "The kinetics of alpha vs gamma Al_2O_3 particle formation in solid-propellant rocket exhausts," AIAA-91-0380, 29th Aerospace Sciences Meeting, Reno NV, January 7-10, 1991.
18. M.E. Zolensky, D.S. McKay, and L.A. Kaczor, "A tenfold increase in the abundance of large solid particles in the stratosphere, as measured over the period 1976-1984," *J. Geophys. Res.* 94, 1047 (1989).
19. W.R. Cofer III, G.C. Purgold, E.L. Winstead, and R.A. Edahl, "Space Shuttle exhausted aluminum oxide: a measured particle size distribution," *J. Geophys. Res.* 96, 17371 (1991).
20. W.R. Cofer III, G.G. Lala, and J.P. Wightman, "Analysis of mid-tropospheric Space Shuttle exhausted aluminum oxide particles," *Atmospheric Environment* 21, 1187 (1987).
21. R.A. Dobbins and L.D. Strand, "A comparison of two methods of measuring particle size of Al_2O_3 produced by a small rocket motor," *AIAA J.* 8, 1544 (1970).
22. R. Dawbarn and M. Kinslow, "Studies of the exhaust products from solid propellant rocket motors," Tech. Rep. AEDC-TR-76-49, U.S. Air Force, Washington D.C., 1976.
23. D.J. Hofmann, D.E. Carroll, and J.M. Rosen, "Estimate of the contribution of the space shuttle effluent to the natural stratospheric aerosol," *Geophys. Res. Lett.* 2, 113 (1975).
24. W.R. Cofer III, G.L. Pellett, D.I. Sebacher, and N.T. Wakelyn, "Surface chloride formation on space shuttle exhaust alumina," *J. Geophys. Res.* 89, 2535 (1984).
25. A. Tabazadeh, R.P. Turco, and M.Z. Jacobson, "A model for studying the composition and chemical effects of stratospheric aerosols," *J. Geophys. Res.* 99, 12897 (1994).

26. P. Ausloos, R.E. Rebbert, and L. Glasgow, *J. Res. NBS* **82**, 1 (1977).
27. St.J. Dixon-Warren, I. Harrison, K. Leggett, M.S. Matyjaszczyk, J.C. Polanyi, and P.A. Young, *J. Chem. Phys.* **88**, 4092 (1988).
28. J.M. White, "Photoassisted Reactions on Doped Metal Oxide Particles," in Heterogeneous Atmospheric Chemistry, D.R. Schreyer, Ed., Geophysical Monograph 26, American Geophysical Union, Washington D.C., 1982, pp. 122-135.
29. L.M. Folan, S. Arnold, and S.D. Druger, "Enhanced energy transfer within a microparticle," *Chem. Phys. Lett.* **118**, 322 (1985).
30. S. Arnold and L.M. Folan, "Energy transfer and the photon lifetime within an aerosol particle," *Optics Lett.* **14**, 387 (1989).
31. M.D. Barnes, W.B. Whitten, S. Arnold, and J.M. Ramsey, "Homogeneous linewidths of rhodamine 6G at room temperature from cavity-enhanced spontaneous emission rates," *J. Chem. Phys.* **97**, 7842 (1992).
32. Arnold, S. and Folan, L.M., "Fluorescence Spectrometer for a Single Electrodynamic Levitate Microparticle," *Rev. Sci. Inst.* **57**, 2250 (1986).
33. Arnold, S., and Folan, L.M., "Spherical Void Electrodynamic Levitator," *Rev. Sci. Inst.* **58**, 1732 (1987).
34. Hartung, W.H., and Avedisian, C.T., "On the Electrodynamic Balance," *Proc. R. Soc. Lond. A* **437** (1992) 237.
35. K.L. Carleton, D.M. Sonnenfroh, W.T. Rawlins, B.E. Wyslouzil, and S. Arnold, "Freezing Behavior of Single Sulfuric Acid Aerosols Suspended in a Quadrupole Trap," *J. Geophys. Res.* **102**, 6025 (1997).
36. W.T. Rawlins, R.R. Foutter, and T.E. Parker, "Vibrational Band Strengths and Temperatures of Nitric Oxide by Time-Resolved Infrared Emission Spectroscopy in a Shock Tube," *J. Quant. Spectrosc. Radiat. Transfer* **49**, 423 (1993).
37. Wyslouzil, B.E., Carleton, K.L., Sonnenfroh, D.M., Rawlins, W.T., and Arnold, S., "Observation of Hydration of Single, Modified Carbon Aerosols," *Geophys. Res. Lett.* **21**, 2107 (1994).
38. Rawlins, W.T., Kang, S.G., Sonnenfroh, D.M., Carleton, K.L., and Wyslouzil, B.E., "Activation of Carbon Aerosol by Deposition of Sulfuric Acid," Biomass Burning and Global Change, J.S. Levine, Ed., MIT Press, Cambridge, MA, 1996, Vol. 1, pp. 540-544.

39. Adamson, A.W., Physical Chemistry of Surfaces, 3rd Edition, John Wiley and Sons, New York, 1976, pp. 618 ff.
40. J.W. Elam, C.E. Nelson, M.A. Cameron, M.A. Tolbert, and S.M. George, "Adsorption of H₂O on a Single-Crystal α -Al₂O₃(0001) Surface," *J. Phys. Chem. B* **102**, 7008 (1998).
41. C.H. Jackman, D.B. Considine, and E.L. Fleming, "Space Shuttle's Impact on the Stratosphere: An Update," *J. Geophys. Res.* **101**, 12,523 (1996).
42. C.H. Jackman, D.B. Considine, and E.L. Fleming, "A Global Modeling Study of Solid Rocket Aluminum Oxide Emission Effects on Stratospheric Ozone," *Geophys. Res. Lett.* **25**, 907 (1998).
43. H.R. Pruppacher and J. D. Klett, Microphysics of Clouds and Precipitation, Reidel, Boston, 1980.

APPENDIX A

WB57F Ozone Measurements

A.1 INTRODUCTION

As part of this program, we implemented the PSI UV Ozone Photometer on board the NASA WB57F high altitude airplane to measure ozone depletion in rocket plumes in the lower stratosphere.¹⁻³ These measurements are part of a suite of instrumentation designed to characterize the chemical changes and particulate environment in the stratosphere in the wakes of rocket launches.⁴ In all, the PSI instrument has made ozone measurements on some 40 test and science flights in 1998 and 1999. During February to June 1998, the instrument was integrated onto the aircraft, several test flights were conducted, and two successful rocket plume intercept missions were flown. A description of the data obtained, and a detailed kinetics analysis of the results of one of the missions, are presented in Appendix B. Two additional rocket plume intercept missions were conducted in April 1999, and the PSI ozone measurement results are summarized below.

A.2 SUMMARY OF KINETIC INTERPRETATIONS

The initial analysis of the Delta II plume intercept data from 17 May 1998 is described in Appendix B. In that analysis, we developed a steady-state approximation to relate the instantaneous ozone destruction rate by $\text{Cl} + \text{O}_3$ to the measured ClO concentrations and the presumed initial Cl_x deposited by the rocket exhaust. (Here Cl_x represents the total reactive chlorine in the form of Cl_2 , Cl , ClO, and Cl_2O_2 .) We approximated the plume dilution rate using the observed plume crossing dimensions, and applied a spatially resolved radial expansion model to estimate the radially integrated ozone depletion as a function of plume age for comparison to the model predictions. Based on an estimated calibration of the ClO instrument, we determined that the observed ozone loss was roughly consistent with the estimated initial Cl_x , but with a large measurement uncertainty that allowed the possibility of significant contributions by other ozone removal mechanisms.

More recently, an accurate calibration of the ClO data has yielded ClO concentrations which imply an initial Cl_x deposition that is clearly too small to account for the observed ozone loss. Based on a simplified steady state approximation, we estimated from the ClO data an initial Cl_x deposition of ~ 1 mole/m or less. We have since applied a rigorous calculation, using numerical integration of the complete rate law given by the reaction mechanism in Appendix B, to determine the detailed steady state relationship between ClO and Cl_x over the full range of Cl_x concentrations that could be encountered in the plume. This relationship is plotted in Figure A-1.

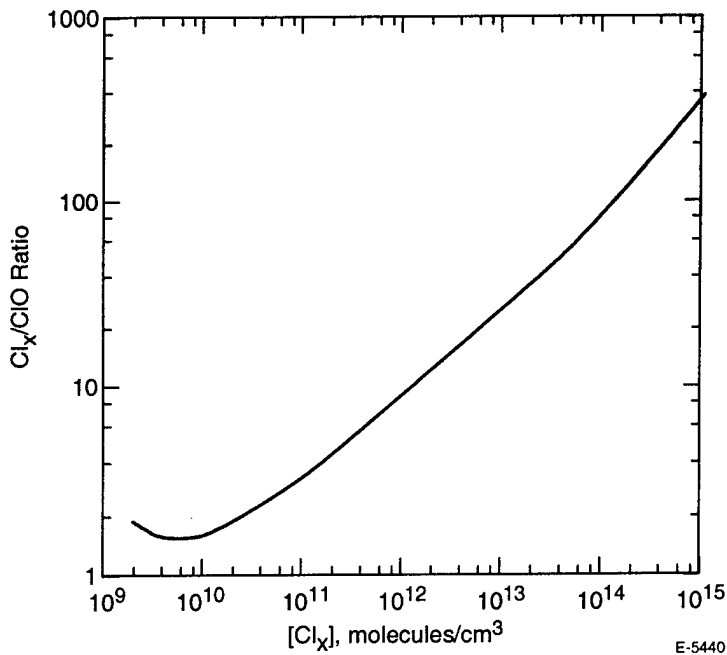


Figure A-1. Steady state relationship between Cl_x and ClO , prior to end point of $\text{Cl} + \text{O}_3$ titration, 18 km altitude, initial $\text{O}_3 = 2 \text{ ppmv}$.

Using the computed steady-state Cl_x/ClO relationship from Figure A-1, we determined the radially integrated Cl_x abundances from the spatially resolved ClO concentrations measured for each plume crossing. This analysis gave total in-plane Cl_x abundances of 0.83, 0.68, and 0.54 mole/m for the second, third, and fourth plume encounters, respectively. The derived value is 0.52 mole/m for the fifth encounter, however it is clear from the O_3 , ClO , and CH_4 data that a significant portion of the plume is over-titrated and no longer satisfies the steady-state relationship. For the first and sixth encounters, the derived Cl_x values are anomalously low, 0.17 and 0.15 mole/m respectively; however we believe that the plume concentrations are undersampled in the first encounter and do not represent a diametric crossing in the sixth encounter. The average of the three representative values is $\text{Cl}_x = 0.7 \text{ mole/m}$. However, we note that the progressive decrease in the derived Cl_x abundances with plume age may also signify an unidentified chemical consumption of Cl_x species within the evolving plume.

In steady-state, the ClO concentration can be related to the O_3 consumption rate as discussed in Appendix B. Thus we can transform the numerical results of Figure A-1 into the O_3 loss rate per unit Cl_x concentration, $-\{d[\text{O}_3]/dt\}/[\text{Cl}_x]$. This quantity is plotted as a function of Cl_x concentration in Figure A-2. At large $[\text{Cl}_x]$, the O_3 loss rate rolls off to approach $[\text{Cl}_x]J_1$, where $J_1 = 1/(4.6 \text{ min})$ is the photolysis rate of Cl_2 as discussed in Appendix B. This is because almost all of the Cl_x at these concentrations is present in the form of Cl_2 , and the O_3 destruction rate is limited by the Cl_2 photolysis step. The assumption of a photolysis-rate-limited steady state, as expressed in Appendix B and in the paper of Ross et al,³ is only strictly true for large $[\text{Cl}_x]$, and otherwise gives an upper bound for the instantaneous O_3 loss rate at a given $[\text{Cl}_x]$.

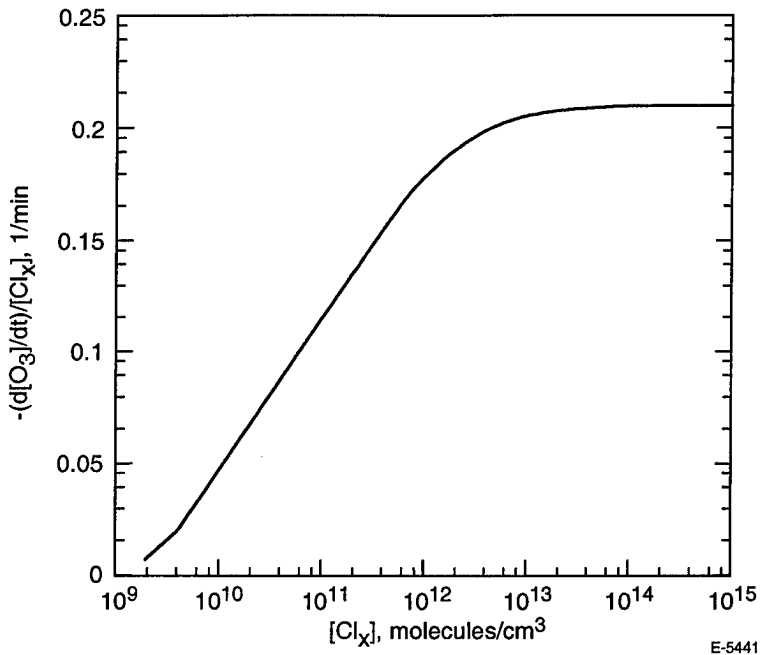


Figure A-2. Instantaneous ozone loss rate per unit $[Cl_x]$, 18 km altitude.

The radially averaged, cumulative ozone loss at a given plume age is determined from a double integral of the instantaneous O_3 destruction rate, $-d[O_3]/dt$ (or $[O_3']$), over time and radius. Using the computed curve in Figure A-2, together with the time-dependent plume dilution approximation determined from the observed plume crossing dimensions (Appendix B), we can evaluate this double integral as a function of plume age for assumed initial Cl_x abundances. That is, for a given $[Cl_x]$, the dilution approximation gives $[Cl_x(r,t)]$. This is then transformed into $[O_3'(r,t)]$, which is integrated over both r and t from zero to the plume age of interest. The results are expressed as cumulative ozone loss in mole/m, and can be directly compared to the measurement results.

The calculated and observed cumulative ozone losses for the Delta II rocket plume are shown in Figure A-3. Data are shown for the first five plume encounters only, since the sixth encounter apparently sampled either an edge or a separated fragment of the plume. The calculations were done for Cl_x abundances of 1.0, 0.8, 0.7, and 0.5 mole/m, the last three values representing the range encompassed by the ClO data. We note that these calculated ozone losses are considerably larger than those obtained from the approximation used by Ross et al,³ $-\{dO_3\} = \{Cl_x\}J_{1t}$, because that approximation does not account for the initially very large $[Cl_x]$ and instantaneous O_3 destruction rates at early times near the plume centerline. All the predictions exceed the ozone loss observed in the first plume encounter, perhaps in part because the instruments were unable to spatially resolve the plume at that early time. The prediction for $\{Cl_x\} = 1.0$ mole/m gives a reasonable match to the data, however the curve for the observed average value of $\{Cl_x\} = 0.7$ mole/m is well below most of the data. In addition, none of the curves have sufficient slope with increasing plume age to account for the large ozone loss

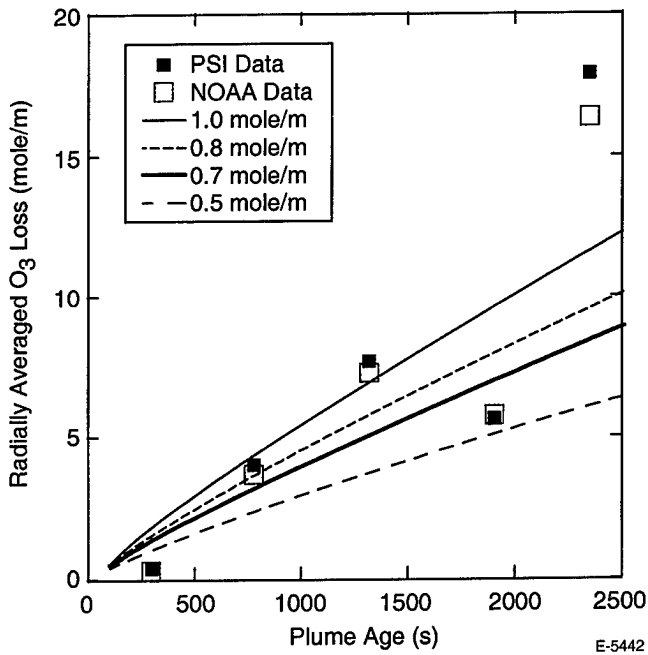


Figure A-3. Predicted and observed cumulative ozone losses, 18 km altitude.

observed in the fifth encounter. Thus it appears clearly distinguishable that the gas-phase Cl + O₃ reaction mechanism accounts for much, but not all, of the observed cumulative ozone loss in the rocket plume.

Several other hypothetical reaction mechanisms should be considered as possible contributors to prompt ozone destruction in the Delta II rocket plume. For present purposes, we focus on one of the more obvious ones, the direct reaction of O₃ with carbonaceous soot particles, which are present among the exhaust products of the kerosene/LOx main engine. This reaction has been reported to occur in laboratory measurements with a reaction efficiency of $\gamma = 3 \times 10^{-3}$.⁵ DeMore et al⁶ recommend an uncertainty in this value of a factor of 30 up and down. As discussed in Appendix B, the instantaneous ozone loss rate due to reaction of O₃ with soot is given by

$$-d[O_3]/dt = (\bar{v} \gamma A_s / 4)[O_3]$$

where \bar{v} is the average molecular thermal velocity and A_s is the concentration of soot surface area in cm²/cm³ ($A_s = AN_p$, A is particle surface area and N_p is particle number density). The UMR particle size distribution measurements from this flight give an area-weighted average radius of 34 nm for the soot component,⁷ corresponding to a distribution-averaged surface area of 1.45×10^{-10} cm²/particle. The product of the reaction efficiency and the particle surface area, γA , is 4.4×10^{-5} $\mu\text{m}^2/\text{particle}$, in good agreement with upper-bound values inferred by Gao et al⁸ from null measurements of ozone loss in Concorde aircraft exhaust plumes.

The initial O_3 destruction rates (i.e., for $[O_3] = [O_3]_0$) are plotted in Figure A-4 for an assumed soot deposition of 0.01 kg/m. This corresponds to ~ 21 g (soot)/kg (propellant). For this soot loading, the centerline particle concentrations are in the range of roughly 10^3 to 10^4 particles/cm 3 , corresponding to surface area concentrations in the range 10^{-6} to 10^{-5} cm 2 /cm 3 . Also plotted in Figure A-4 are the instantaneous O_3 destruction rates due to the Cl_x reaction mechanism as determined above. The sum of the two curves gives total O_3 loss rates that are in good agreement with those predicted from the Cl_x mechanism alone for $\{Cl_x\} = 1.0$ mole/m, which in turn give predicted cumulative ozone losses that are fairly consistent with the data (Figure A-3). That is, the combination of the soot and Cl_x mechanisms gives a reasonable accounting for the observed cumulative ozone loss in the plume, provided we assume 0.01 kg/m of soot deposited by the kerosene/LOx main engine. However, we note that this combination still does not account for the non-linear effect at late time.

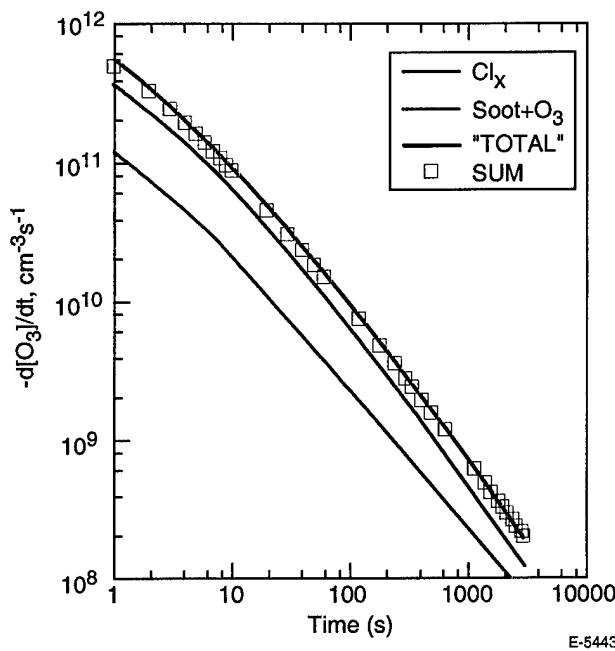


Figure A-4. Instantaneous ozone loss rates for Cl_x and soot reaction mechanisms. "TOTAL" signifies prediction for Cl_x mechanism assuming $\{Cl_x\} = 1.0$ mole/m, to approximate instantaneous $[O_3]$ corresponding to observed cumulative ozone depletions.

Unfortunately, due to the inherent measurement uncertainties and poor sampling statistics for this single flight, we cannot reach any firm conclusions about the possible role of soot in the observed plume ozone loss. In particular, the emission index of soot for these engines is not well known. More definitive evaluations of this reaction require analysis of ozone loss and Cl_x data for plume intercepts in which soot particle yields are well characterized. There may also be other ozone removal or Cl_x recycling mechanisms at work, involving HO_x , NO_x , and/or NO_y . Further examination of these hypotheses awaits more comprehensive flight measurements and kinetic modeling.

A.3 SUMMARY OF 1999 ROCKET PLUME INTERCEPT DATA: PSI OZONE

As part of the ACCENT 1999 mission plan, we flew the PSI Ozone instrument on WB57F rocket plume intercept missions in April 1999 and again in September 1999. The instrument was also flown on several missions to perform measurements in the unperturbed upper troposphere and lower stratosphere during the same time frame. On 12 April 1999, a successful mission was flown to intercept the exhaust plume of an Atlas IIAS rocket launched from Cape Canaveral. An overview of PSI Ozone data for the plume-encounter portion of the flight is shown in Figure A-5. Some 10 plume crossings are clearly identifiable in the ozone data. Several of the plume intercepts show near-total ozone depletion within the plume, and most show complex bifurcated structures as illustrated for the seventh encounter in Figure A-6. The region of perturbed air in Figure 6 is some 40 seconds wide, corresponding to a dimension of ~7.6 km. The general character of this data, i.e. the persistence and complexity of the plume structures, is very similar to that observed for an Atlas IIAS rocket in 1998 and described in Appendix B.

Another mission on 15 April 1999 intercepted the exhaust plume of a Delta II rocket launched from Vandenberg AFB. In this case, there was one encounter with the plume at high altitude, after which the plume became invisible to the pilot at that altitude. The pilot then descended below the tropopause, where the plume was still visible, however the ozone concentrations were so low at that altitude that ozone depletions in the plume were difficult to discern. In addition, during that descent, some foreign matter (possibly plume particulate matter) entered one leg of the ozone absorption cell and obscured the light path, reducing the measurement functionality to only one side of the cell for the remainder of the flight. Extraction of useful

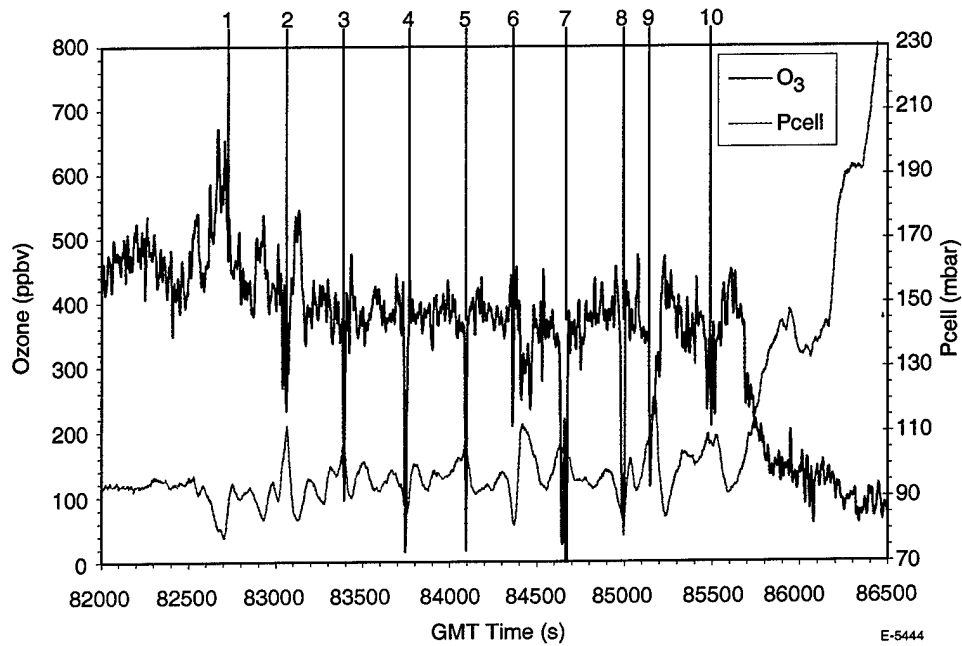


Figure A-5. Ozone mixing ratios and cell pressures for portion of Flight 990412, showing the ozone depletion data for encounters with an Atlas IIAS rocket exhaust plume.

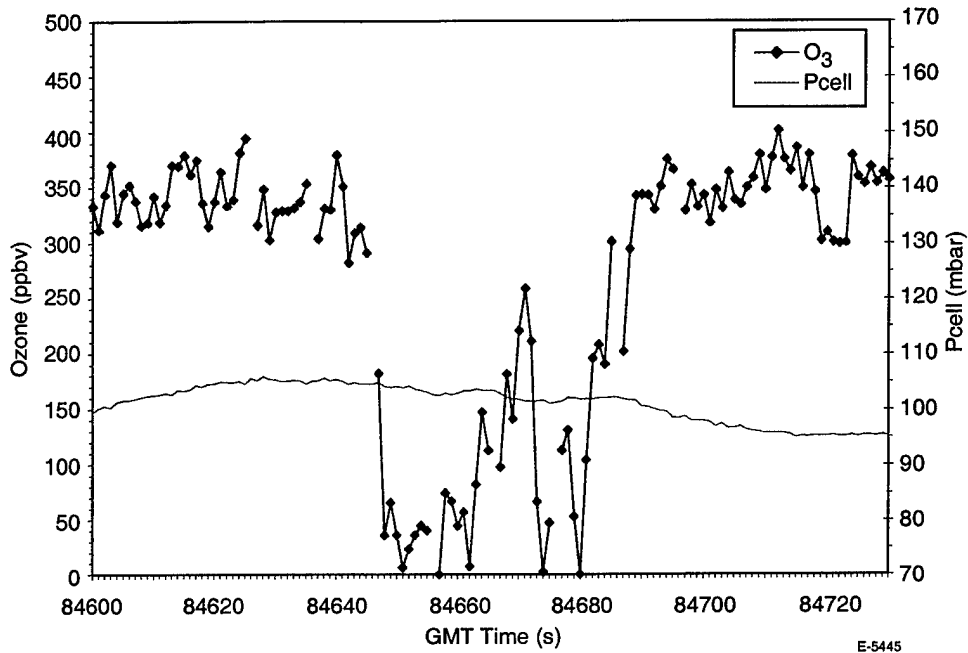


Figure A-6. Ozone mixing ratios and cell pressures during the seventh encounter with the Atlas IIAS exhaust plume, Flight 990412. Measurement frequency is 1 Hz.

ozone depletion data from these measurements will be limited to plume crossings that occurred when the properly functioning absorption channel was in sample mode. We note that the NOAA O₃ instrument acquired data throughout the plume measurement sequence.

Finally, on 24 September 1999, a successful intercept mission was flown for the exhaust plume of an Athena rocket launched from Vandenberg AFB. Six plume encounters near 18 km altitude were achieved. In this case, the PSI Ozone instrument was set up to acquire data at 4 Hz instead of 1 Hz, giving unprecedented spatial resolution (~50 m) of the ozone depletion patterns. Example data for the fifth plume encounter are shown in Figure A-7. Again, near-total ozone depletion was observed within the plume, and the late-time plume structure was quite complex.

In summary, the 1999 additions to the rocket plume data base are substantial. The two Atlas data sets are very similar, and should be analyzed together to provide comparisons of reproducibility and statistical sampling. The Athena data set provides new information at high spatial resolution, as well as new ozone depletion data for a low-Cl_x rocket. In addition, other instrumentation added to the payload provides new data on ClO at high spatial resolution, on aerosol CCN, CN and particle size distributions in the plume, and, for the Athena flight, on NO_x, NO_y, and CO₂ yields. Detailed analysis of the PSI Ozone data for the 1999 Athena and the 1998 and 1999 Atlas missions remains to be performed.

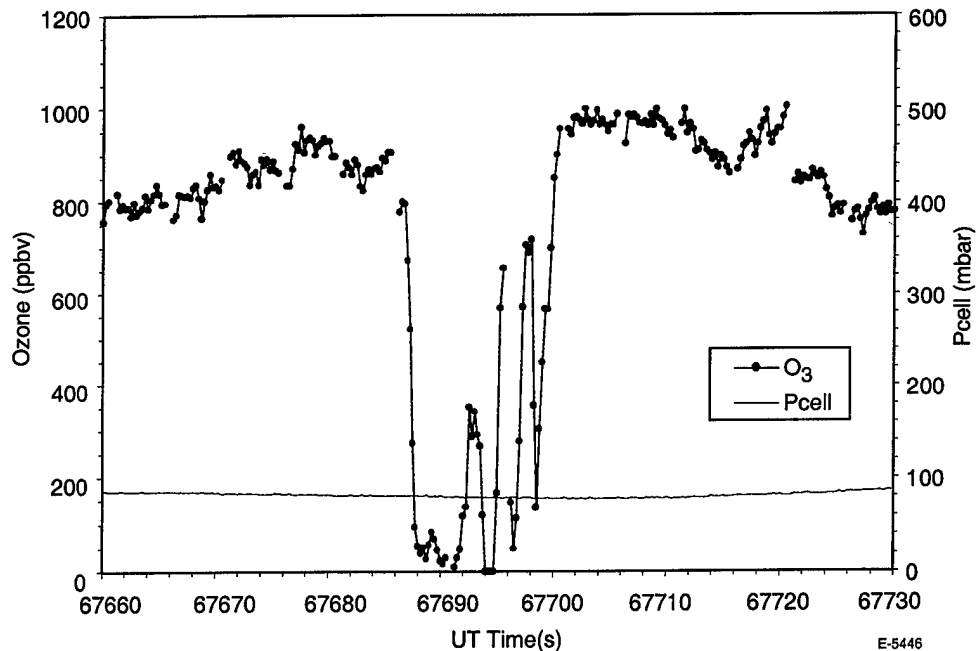


Figure A-7. Ozone mixing ratios and cell pressures during the fifth encounter with an Athena rocket exhaust plume, Flight 990924. Measurement frequency is 4 Hz.

A.4 REFERENCES

1. M.H. Proffitt and W.T. Rawlins, "RISO WB57F Measurements and Intercomparisons of Stratospheric Ozone Depletion in the Exhaust Plume of a Delta II Rocket," American Geophysical Union 1998 Fall Meeting, Paper A31B-04, *EOS Trans. AGU* **79**, F139 (Abstract), 1998.
2. W.T. Rawlins, J.R. Benbrook, D.E. Hagen, A.R. Hopkins, K.K. Kelly, M.H. Proffitt, E. Richard, M.N. Ross, W.R. Sheldon, D.W. Toohey, and P.D. Whitefield, "Kinetics of Stratospheric Ozone Depletion in the Exhaust Plume of a Delta II Rocket as Observed in RISO," American Geophysical Union 1998 Fall Meeting, Paper A31B-03, *EOS Trans. AGU* **79**, F139 (Abstract), 1998.
3. M.N. Ross, D.W. Toohey, W.T. Rawlins, E. Richard, K.K. Kelly, A.F. Tuck, M.H. Proffitt, D.E. Hagen, A.R. Hopkins, P.D. Whitefield, J.R. Benbrook, and W.R. Sheldon, "Observation of Stratospheric Ozone Depletion Associated with Delta II Rocket Emissions," *Geophys. Res. Lett.*, submitted for publication, 2000.
4. M.N. Ross, R.R. Friedl, D.E. Anderson, G. Ash, M.R. Berman, B. Gandrud, W.T. Rawlins, E. Richard, and A.F. Tuck, "Study Blazing New Trails into Effects of Aviation and Rocket Exhaust in the Atmosphere," *EOS Trans. AGU* **80**, 437-443 (1999).

5. C.A. Rogaski, D.M. Golden, and L.R. Williams, "Reactive Uptake and Hydration Experiments on Amorphous Carbon Treated with NO₂, SO₂, O₃, HNO₃, and H₂SO₄," *Geophys. Res. Lett.* **24**, 381 (1997).
6. W.B. DeMore, S.P. Sander, D.M. Golden, R.F. Hampson, M.J. Kurylo, C.J. Howard, A.R. Ravishankara, C.E. Kolb, and M.J. Molina, "Chemical Kinetics and Photochemical Data for Use in Stratospheric Modeling, Evaluation Number 12," JPL Publication 97-4, Jet Propulsion Laboratory, January 15, 1997.
7. D.E. Hagen, P.D. Whitefield, and R. Hopkins, "Aerosol Emissions Characterization in Delta Rocket Exhaust Plumes," American Geophysical Union 1998 Fall Meeting, Paper A31B-02, *EOS Trans. AGU* **79**, F139 (Abstract), 1998.
8. R.S. Gao, B. Kärcher, E.R. Keim, and D.W. Fahey, "Constraining the Heterogeneous Loss of Ozone on Soot Particles with Observations in Jet Engine Exhaust Plumes," *Geophys. Res. Lett.* **26**, 3323 (1998).

Airborne In Situ Ozone Measurements in Rocket Exhaust Plumes

Final Report

P.O. 4600000883

Submitted by:

Wilson T. Rawlins
Physical Sciences Inc.
20 New England Business Center
Andover, MA 01810

Submitted to:

Aerospace Corporation
355 South Douglas Street
El Segundo, CA 90245
Attention: Martin Ross

September 1998

TABLE OF CONTENTS

<u>Section</u>	<u>Page</u>
1. INTRODUCTION	1
2. INSTRUMENTATION AND FLIGHTS	2
3. MEASUREMENT RESULTS	3
3.1 Delta II	3
3.2 Atlas IIAS	8
4. KINETICS ANALYSIS: DELTA II	10
4.1 Chlorine Kinetics	10
4.2 Soot Kinetics	15
4.3 Plume Model	16
5. SUMMARY AND CONCLUSIONS	22
6. REFERENCES	23

LIST OF FIGURES

<u>Figure No.</u>		<u>Page</u>
1	PSI and NOAA O ₃ mixing ratios, PSI photometer cell pressures, and University of Missouri-Rolla particle counts for the RISO Delta II rocket plume intercept on 17 May 1998, Pass 1, 301 s after launch	3
2	PSI and NOAA O ₃ mixing ratios, PSI photometer cell pressures, and University of Missouri-Rolla particle counts for the RISO Delta II rocket plume intercept on 17 May 1998, Pass 2, 782 s after launch	4
3	PSI and NOAA O ₃ mixing ratios, PSI photometer cell pressures, and University of Missouri-Rolla particle counts for the RISO Delta II rocket plume intercept on 17 May 1998, Pass 3, 1321 s after launch	4
4	PSI and NOAA O ₃ mixing ratios, PSI photometer cell pressures, and University of Missouri-Rolla particle counts for the RISO Delta II rocket plume intercept on 17 May 1998, Pass 4, 1907 s after launch	5
5	PSI and NOAA O ₃ mixing ratios, PSI photometer cell pressures, and University of Missouri-Rolla particle counts for the RISO Delta II rocket plume intercept on 17 May 1998, Pass 5, 2344 s after launch	5
6	PSI and NOAA O ₃ mixing ratios, PSI photometer cell pressures, and University of Missouri-Rolla particle counts for the RISO Delta II rocket plume intercept on 17 May 1998, Pass 6, 2848 s after launch	6
7	Intercepted plume widths and diameter curvefits, from University of Missouri-Rolla particle data	7
8	Observed ozone depletion rates for Delta II rocket	8
9	PSI O ₃ mixing ratios and photometer cell pressures, and University of Missouri-Rolla particle counts for the RISO Atlas IIAS rocket plume intercept on 18 June 1998 showing all passes	9
10	Constant volume kinetics model illustrating ozone and methane consumption by active chlorine at conditions appropriate for 18 km altitude	12
11	Cumulative and instantaneous ozone loss rates	14
12	Computed ozone depletion radial profiles at 18 km altitude assuming R(Cl ₂) = 0.25 mole/m	17

LIST OF FIGURES (Continued)

<u>Figure No.</u>		<u>Page</u>
13	Computed ozone depletion radial profiles at 18 km altitude assuming $R(Cl_2) = 0.5$ mole/m	18
14	Computed and observed ozone depletion diameters for the region of the plume where ΔO_3 exceeds 1000 ppbv	18
15	Modeled dependence of O_3 loss on ClO for a spatial resolution of 200 m, assuming $R(Cl_2) = 0.25$ mole/m	19
16	Modeled dependence of O_3 loss on ClO for a spatial resolution of 200 m, assuming $R(Cl_2) = 0.5$ mole/m	19
17	Observed dependence of O_3 loss on ClO for the Delta II rocket	20

1. INTRODUCTION

The Air Force's Rocket Impacts on Stratospheric Ozone (RISO) program supports airborne in situ measurements of rocket exhaust plume chemistry by a WB-57F high altitude airplane.^{1,2} The objective of these measurements is to characterize the plume and plume-atmosphere chemical and dynamic processes that affect local ambient ozone concentrations following the rocket launch. A measurement of primary importance is that of the ozone mixing ratio in the perturbed and unperturbed upper atmosphere. Recent in situ ozone measurements^{1,2} have indicated substantial depletions of ozone within the rocket plumes. This report describes new measurements in two rocket exhaust plumes, using the recently developed PSI UV ozone photometer on board the NASA WB-57F aircraft (#928), based at Ellington Field, NASA Johnson Space Center, Houston, Texas. Flight measurements were performed in the exhaust plumes of a Delta II and an Atlas IIAS rocket. We describe below the Physical Sciences Inc. (PSI) ozone instrumentation and measurements for these two flights, and a detailed analysis of the Delta II data set and its implications for atmospheric chemical kinetics.

2. INSTRUMENTATION AND FLIGHTS

The PSI UV ozone photometer was installed on a "short" pallet which was loaded into the WB-57F payload bay in pallet position #2 for the RISO flights. Companion instruments on this pallet were the NOAA Aeronomy Laboratory's CH₄ and O₃ instruments. The PSI instrument is a 1 Hz, dual-beam, UV absorption photometer designed for high-altitude airborne measurements in an unpressurized, unheated environment. The instrument was built by PSI and Proffitt Instruments Ltd., based on prototype design and components developed and flight-tested previously.^{3,4} It weighs 25 lb, measures 18 x 12 x 10 in., consumes <85 W at 28 VDC (30 to 50 W in typical high-altitude cruise conditions), and has a noise-limited O₃ detection sensitivity of $\approx 3 \times 10^{10}$ molecules/(cm³Hz^{1/2}) over a 20 cm optical path. A catalytic scrubber removes ozone from the reference beam path, and a four-way teflon valve interchanges scrubbed and ozone-laden flows between the two temperature-controlled optical channels every 10 seconds. Reference and transmitted beam intensities from a 254 nm mercury pen lamp are sampled with 20-bit precision at 1 Hz by a custom detection circuit; cell pressure, air flow temperatures, and housekeeping data are acquired by a 12-bit data system. The data are acquired and processed by a PC-486 single-board computer (PC104 format), and are written to a removable 20 MB PCMCIA card for subsequent retrieval and analysis.

The RISO science flights reported here were preceded by several test and science flights of the WB57F Aerosol Mission (WAM), as well as a number of RISO test and ferry flights. During those flights we performed flight-testing, shakedown, and intercomparisons with data from the NOAA Aeronomy Laboratory's dual-beam UV ozone photometer developed and operated by M.H. Proffitt.⁵ These flights showed that the observed noise levels at altitude were larger than the intrinsic noise limit observed on the ground. Much of the observed extrinsic noise was due to fluid dynamic effects at the external sampling inlet; we experimented with various inlet configurations and flow rates throughout most of WAM, optimized the inlet conditions for the current setup, and concluded that the inlet needs to be redesigned for future missions. Some of the extrinsic noise may also have been caused by fluctuations in the supply voltage due to the absence of an isolated return line in the aircraft wiring harness; we plan to install an isolating power supply for future missions. A fraction of the extrinsic noise was also probably contributed by clearly identifiable hardware problems related to performance of the UV beamsplitter and the four-way valve; these will be resolved in our laboratory prior to the next mission.

The first of the RISO flights reported here sampled the exhaust plume of a Delta II rocket launched from Vandenberg AFB on 17 May 1998. This flight produced six identifiable plume crossings at times ranging from ≈ 5 to ≈ 48 minutes after launch. The second flight sampled the exhaust plume of an Atlas IIAS rocket launched from Cape Canaveral on 18 June 1998. This flight produced an extensive and complex data set containing some 14 plume crossings over a period of almost 2 hours, extending through sunset. We have analyzed the Delta II data in considerable detail, as discussed below. The steps taken and hypotheses formed during the Delta II analysis will serve as a guide to more detailed analysis of the Atlas IIAS data to be performed in the future.

3. MEASUREMENT RESULTS

3.1 Delta II

The PSI O_3 mixing ratio data for the six Delta II plume crossings are shown in Figures 1 through 6. Also plotted in these figures are the pressure in the measurement cell (right hand axis), the ozone mixing ratios measured by the NOAA ozone photometer (data provided by M.H. Proffitt), and the particle number densities measured by the University of Missouri-Rolla particle counter (data provided by Ray Hopkins). The pressure measurements provide a relative indicator of aircraft altitude; since the cell pressure is only slightly less than the stagnation pressure at the external inlet, this value should be about 29% greater than the ambient (static) pressure (assuming aircraft speed ≈ 180 m/s). Thus the typical measured values of 85 to 90 mbar suggest ambient pressures of 66 to 70 mbar, which in turn indicate plume encounter altitudes of 18 to 19 km.

The particle data have not been corrected for non-linear response of the detection system, but can be used to mark the boundaries of the particulate-laden region of the plume. Both ozone instruments show regions of ozone depletion which correspond well to the particle data, in terms of both lateral extent and spatial structure within the plume. Additional comparisons to ClO data provided by Darin Toohey (University of California at Irvine) show similar registration of plume-generated ClO with the edges and spatial structure of the particulate-laden region.

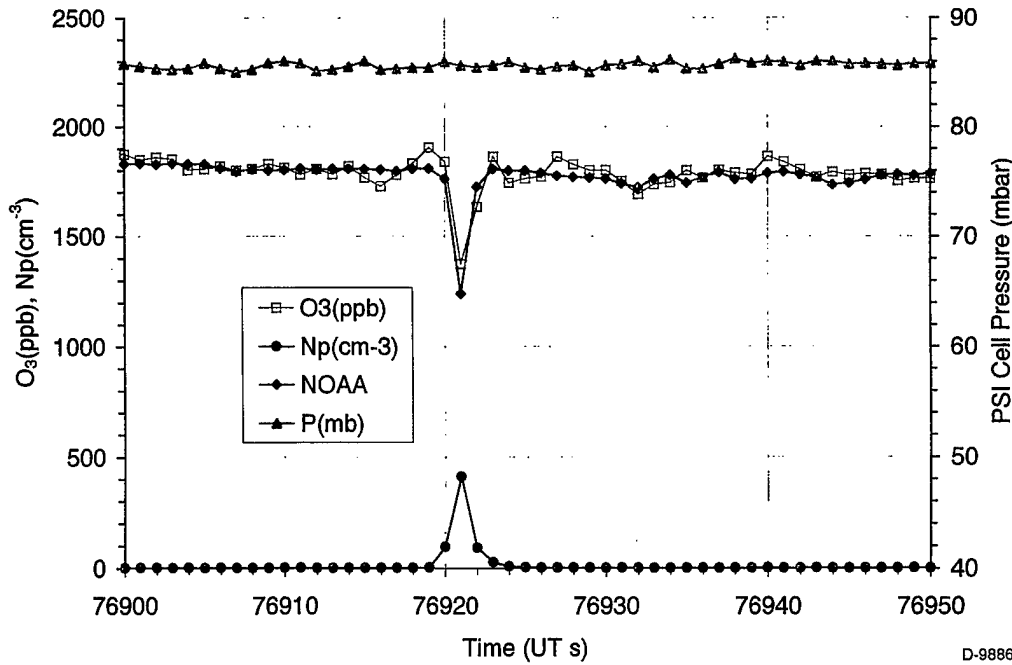


Figure 1. PSI and NOAA O_3 mixing ratios, PSI photometer cell pressures (to indicate altitude), and University of Missouri-Rolla particle counts for the RISO Delta II rocket plume intercept on 17 May 1998, Pass 1, 301 s after launch.

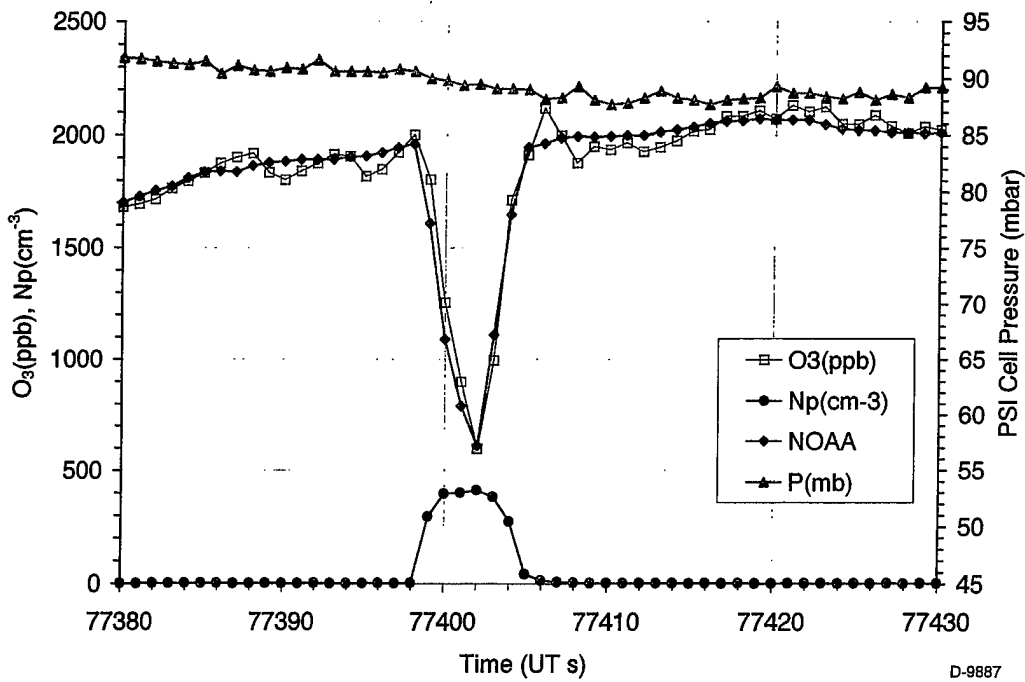


Figure 2. PSI and NOAA O_3 mixing ratios, PSI photometer cell pressures (to indicate altitude), and University of Missouri-Rolla particle counts for the RISO Delta II rocket plume intercept on 17 May 1998, Pass 2, 782 s after launch.

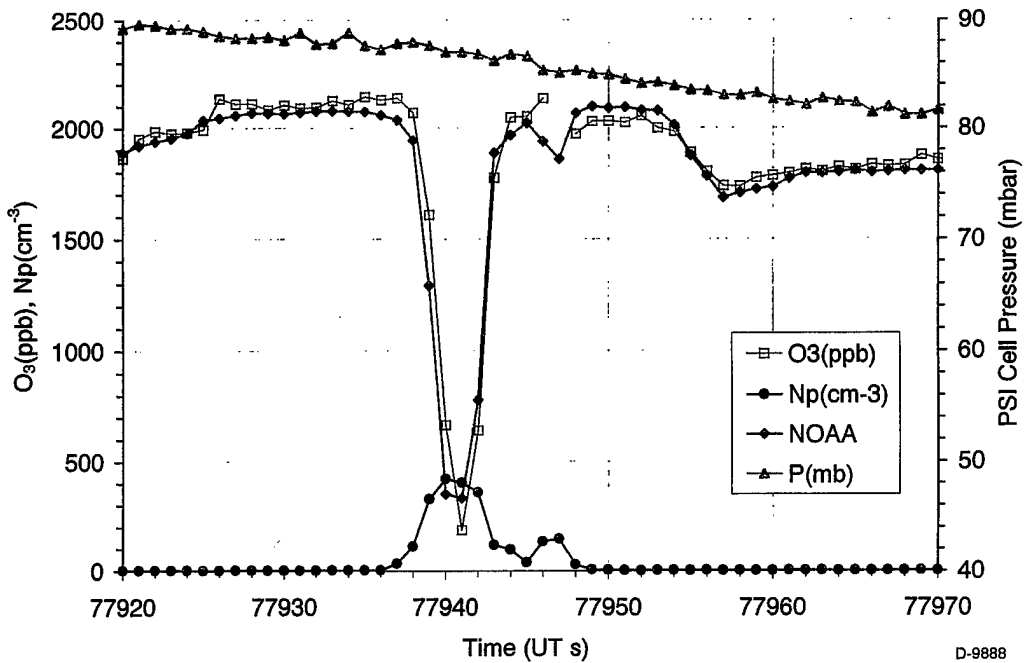


Figure 3. PSI and NOAA O_3 mixing ratios, PSI photometer cell pressures (to indicate altitude), and University of Missouri-Rolla particle counts for the RISO Delta II rocket plume intercept on 17 May 1998, Pass 3, 1321 s after launch.

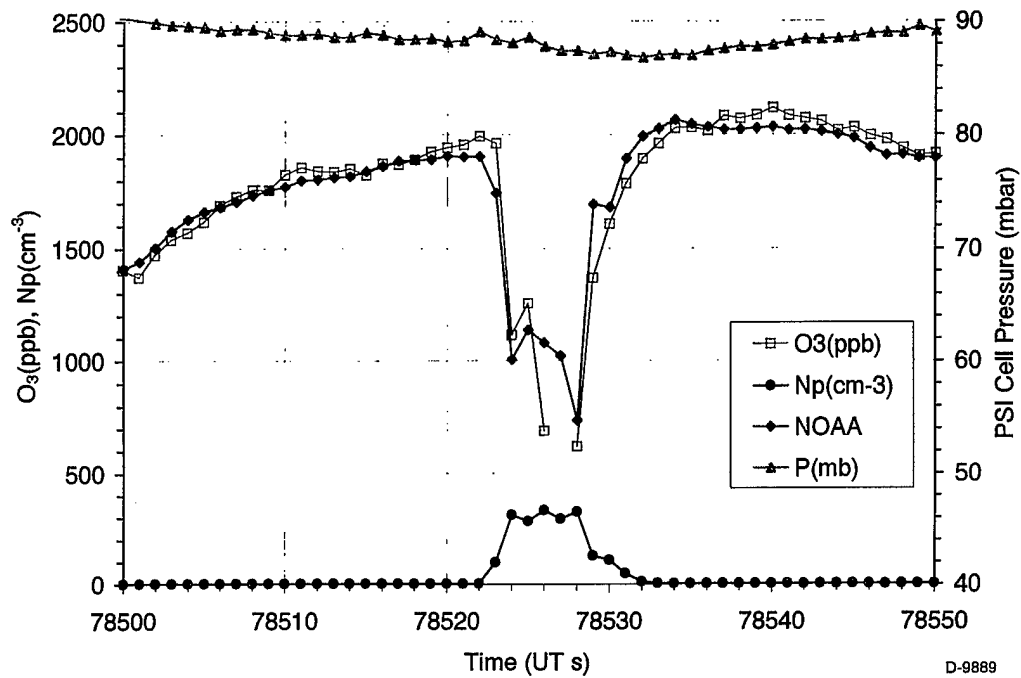


Figure 4. PSI and NOAA O_3 mixing ratios, PSI photometer cell pressures (to indicate altitude), and University of Missouri-Rolla particle counts for the RISO Delta II rocket plume intercept on 17 May 1998, Pass 4, 1907 s after launch.

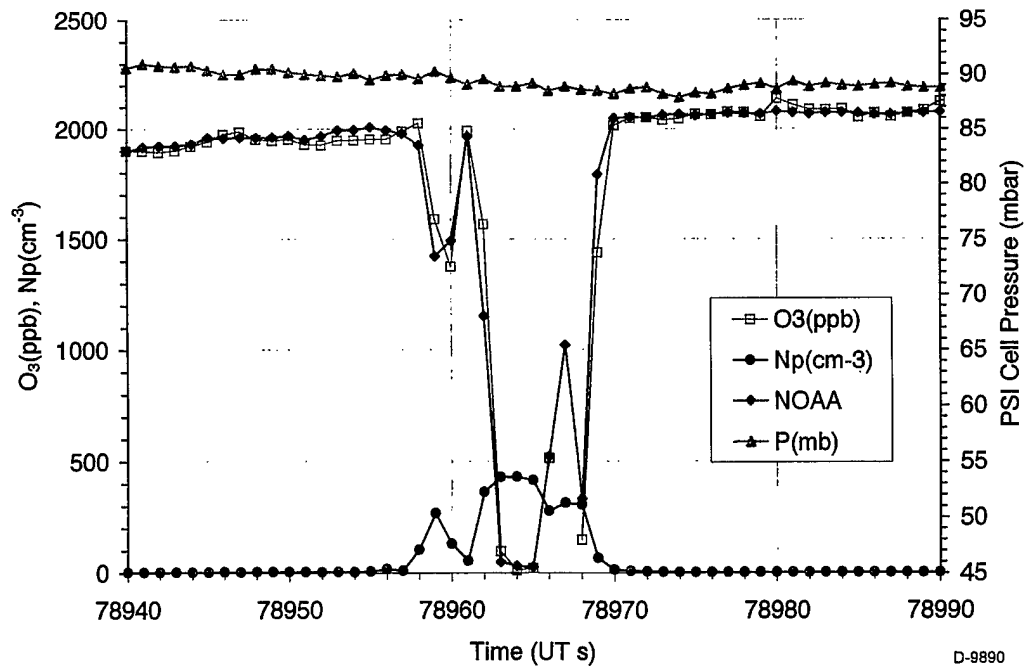


Figure 5. PSI and NOAA O_3 mixing ratios, PSI photometer cell pressures (to indicate altitude), and University of Missouri-Rolla particle counts for the RISO Delta II rocket plume intercept on 17 May 1998, Pass 5, 2344 s after launch.

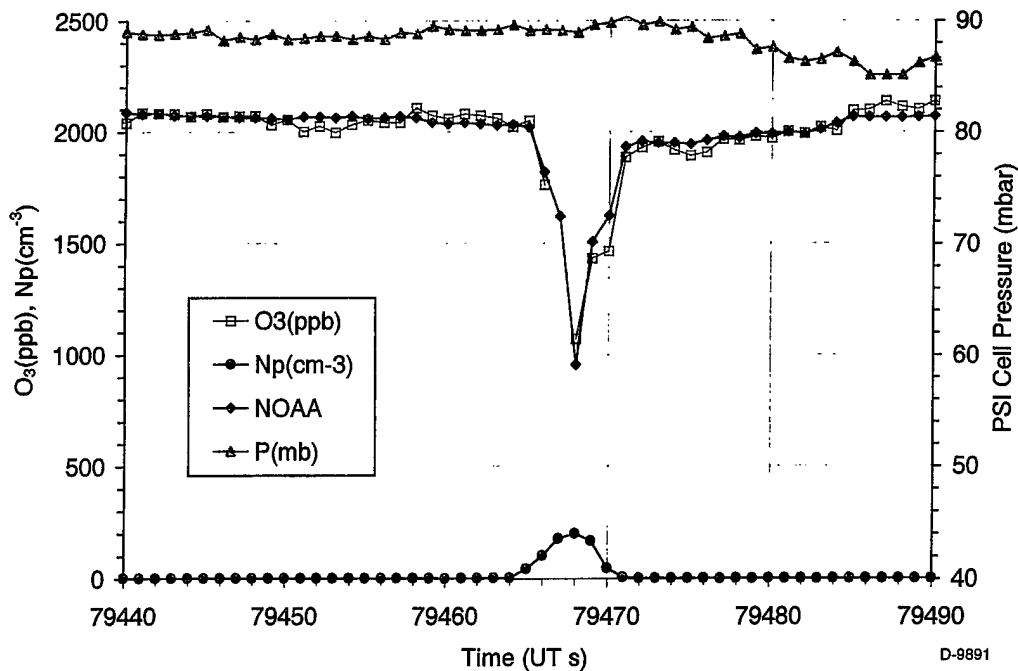


Figure 6. PSI and NOAA O_3 mixing ratios, PSI photometer cell pressures (to indicate altitude), and University of Missouri-Rolla particle counts for the RISO Delta II rocket plume intercept on 17 May 1998, Pass 6, 2848 s after launch.

The PSI ozone data for the slowly varying, unperturbed ambient atmosphere were reduced to ozone mixing ratios using the dual-channel signal ratios as described elsewhere.⁴ For the plume-crossing regions, the data reduction algorithm was modified to ensure accurate response to rapidly varying ozone levels, at the expense of noise reduction provided by the ratiometric approach. The agreement between the PSI and NOAA measurements is very good, within $\approx 2\%$ on average in the ambient atmosphere. It should be pointed out that the two instruments sampled air on opposite sides of the airplane using inlets of different lengths (the PSI inlet was probably sampling inside the aircraft boundary layer while the NOAA inlet was probably outside the boundary layer). In addition, the 1 Hz measurement times of the two instruments were not synchronized. Since the rocket exhaust plume is clearly highly spatially structured, the differences in sampling configuration and timing between the two instruments can be expected to lead to some degree of discrepancy in the determinations of plume-depleted ozone mixing ratios. In view of these differences, the agreement between the two instruments is striking, especially when integrated over each plume crossing.

With the exception of Pass 6, the ozone data show ozone depletion within the plume which progressively increases with plume age. The depletion in the core of the plume reaches $\approx 100\%$, and the radial extent of the depleted region increases steadily throughout the first five passes (≈ 40 min) with little evidence of mixing into the external, ambient atmosphere. Passes 3-5 show increasing evidence of a lobed, complex structure, suggesting the beginnings of vortex breakup and intrusion of the ambient atmosphere; this may signify an early stage of the mixing-

out process. Based on the observed crossing durations, the plume diameter grows from ≈ 0.8 km at 5 min to ≈ 2.4 km at 39 min, as shown in Figure 7. The much shorter duration of Pass 6, ≈ 1.3 km at 48 min, suggests that this encounter was either a near miss or involved a partially mixed-out fragment shed from the main plume. The two curves in Figure 7 represent (1) linear expansion of the plume diameter at 100 m/min (straight line) and (2) linear expansion of cross sectional area at $1965 \text{ m}^2/\text{s}$ (curve). The latter gives a better representation of the apparent evolution of the plume dimensions at long times.

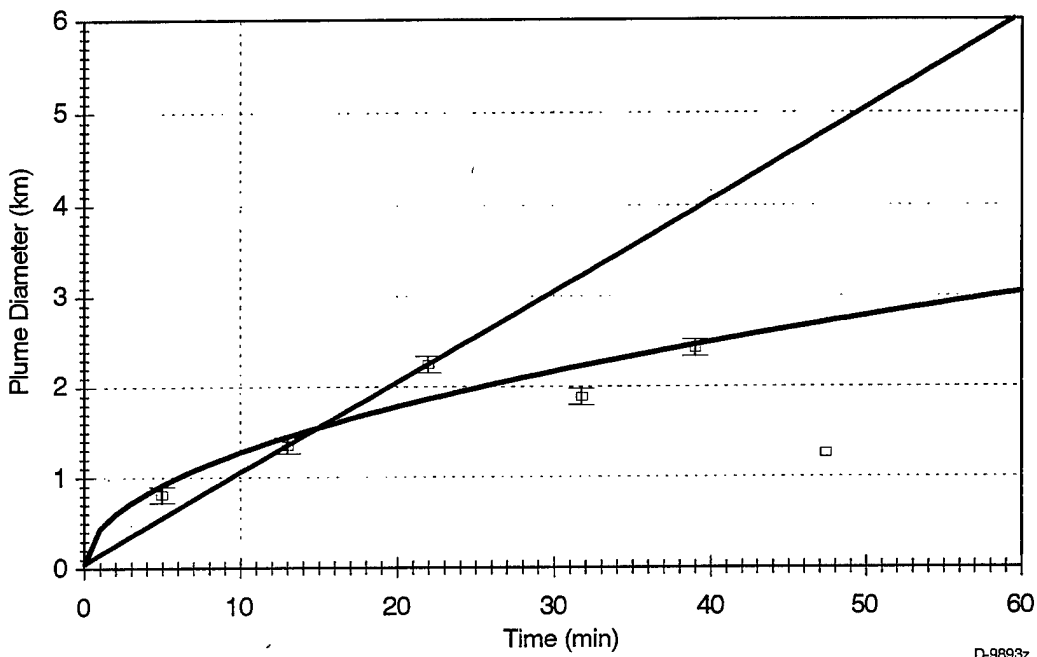


Figure 7. Intercepted plume widths and diameter curvefits, from University of Missouri-Rolla particle data.

By estimating the plume cross sectional area from the observed crossing path lengths, it is possible to estimate the ozone destruction efficiency of the Delta II rocket plume. To perform this estimate, we assumed the observed crossing lengths for Passes 1-5 were diameters of a circular cross section, and averaged the observed ozone losses along each pass for each of the PSI and NOAA data sets. To convert the ozone losses from mixing ratios to concentrations, we assumed an altitude of 18 km, corresponding to a temperature of 215 K and a total number density of 2.2×10^{18} molecules/cm³. The ozone depletion efficiency, dN/dz in moles per meter of altitude, is then given by the product of the pass-averaged loss in ozone concentration in mole/m³ and the apparent plume cross-sectional area in m². Since the actual plume diameters may be larger than the observed pass lengths, and the plume cross section may not be circular, these estimates should be considered lower bounds to the ozone depletion efficiency. The results are plotted in Figure 8. The ozone depletion appears to be still increasing at a plume age of 40 min, and is on the order of ≈ 20 mole/m at that time. These values are approaching the value of ≈ 40 mole/m at 49 min previously reported for a Titan IV plume.²

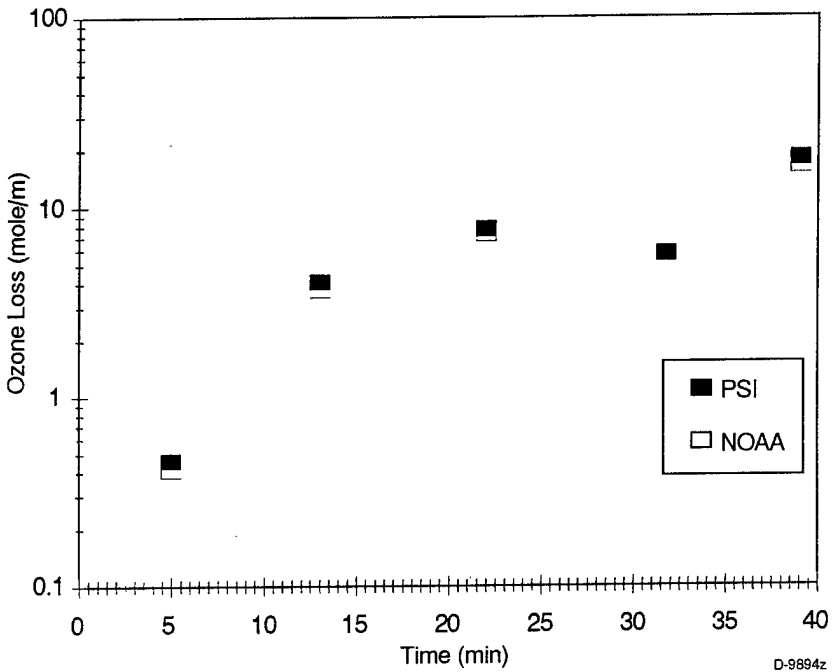


Figure 8. Observed ozone depletion rates for Delta II rocket.

3.2 Atlas IIAS

Preliminary results from the PSI ozone measurements in the Atlas IIAS exhaust plume are shown in Figure 9. The University of Missouri-Rolla particle counter data provided by Ray Hopkins are also shown, to benchmark the plume crossings. The ambient atmosphere shows much lower ozone mixing ratios than in the case of the Delta II measurements; the local atmosphere is highly structured, with distinctly different air parcels containing ozone mixing ratios of ≈ 700 and ≈ 900 ppbv, respectively. The aircraft navigator recorded 18 plume crossings during the flight, however closer inspection of the particle counter data reveals some of these to be different components of the same crossing. Based on the particle counter data, we count 14 clearly identifiable crossings, over a period of ≈ 103 min. Most of the crossings occur at an altitude of ≈ 18 km.

The region of the plume being sampled by the aircraft was bifurcated into two primary components; this bifurcation is pronounced as early as Pass 3 (83330 s UT). The overall plume width, as well as the separation of the bifurcated components, increases steadily with plume age. The ozone depletion patterns within the plume reflect the bifurcation observed in the particle data. In addition, the ozone patterns are highly structured and complex, and may contain significant evidence of mixing into the ambient atmosphere as a function of time. Ozone depletions in the two lobes approach 100% up to 87000 s UT. The degree of ozone depletion is remarkably diminished after 87000 s UT; it is noticeably reduced for Pass 12 (87200 s UT), barely detectable against the ambient atmospheric fluctuations for Pass 13 (87600 s UT), and undetectable for Pass 14 (88850 s UT). Quantitative analysis of this data is under way.

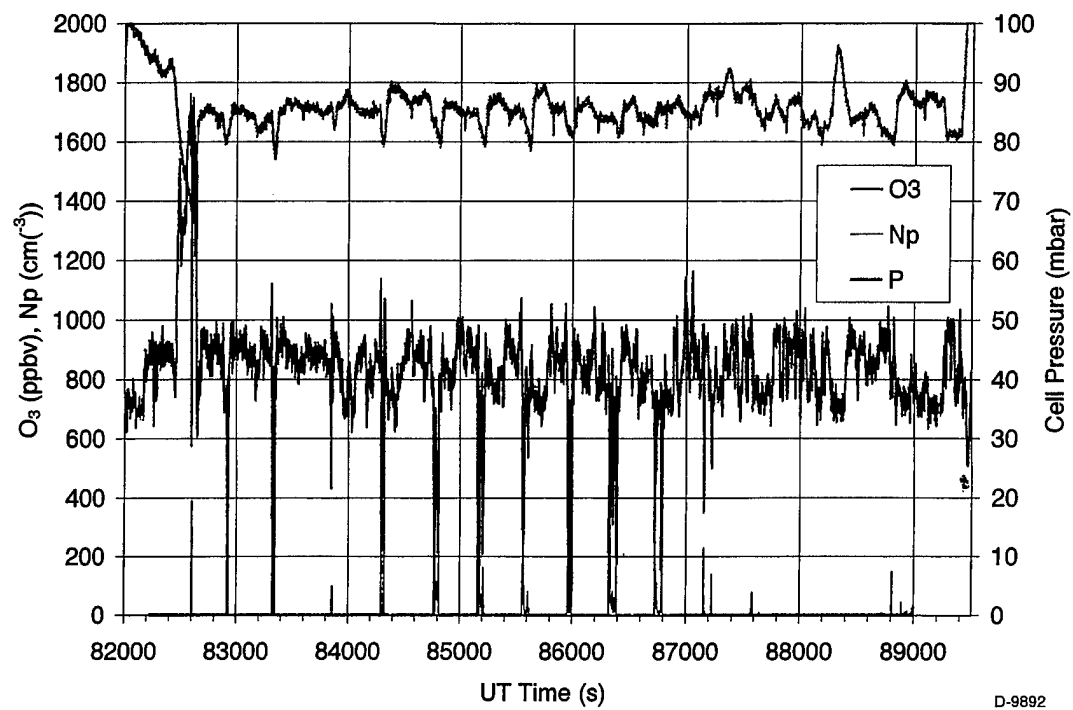


Figure 9. PSI O_3 mixing ratios and photometer cell pressures (to indicate altitude), and University of Missouri-Rolla particle counts for the RISO Atlas IIAS rocket plume intercept on 18 June 1998 showing all passes.

4. KINETICS ANALYSIS: DELTA II

The observation for the Delta rocket plume of ozone depletions on the scale of 20 mole/m is much larger than the expected active chlorine production of 0.5 mole(Cl₂)/m for this rocket. This suggests a highly efficient catalytic cycle for destruction of ozone by active chlorine, which is further supported by Toohey's observations of 10 to 40 ppbv of ClO highly correlated with the ozone depletion patterns. However, the large ozone depletions for this relatively low-chlorine rocket also raise questions about other possible ozone removal mechanisms, namely heterogeneous reaction of ozone on plume soot particles and/or enhancement of the free chlorine cycle by heterogeneous chlorine activation on either soot or aluminum oxide particles present in the plume. We need to answer the following questions:

- (1) Are the observed ozone depletion and ClO production consistent with a homogeneous, catalytic active chlorine chemical cycle?
- (2) Does heterogeneous reaction on soot particles contribute to the ozone loss?
(a) What is the expected O₃ + soot reaction rate in the plume? (b) Is there too much ozone depletion for the amount of ClO observed, suggesting the need for an additional ozone removal mechanism?
- (3) Is the observed ClO yield consistent with the expected active chlorine production of the rocket afterburning region? Is there evidence for an additional chlorine activation mechanism, perhaps via heterogeneous processes on plume exhaust soot and aluminum oxide particles?

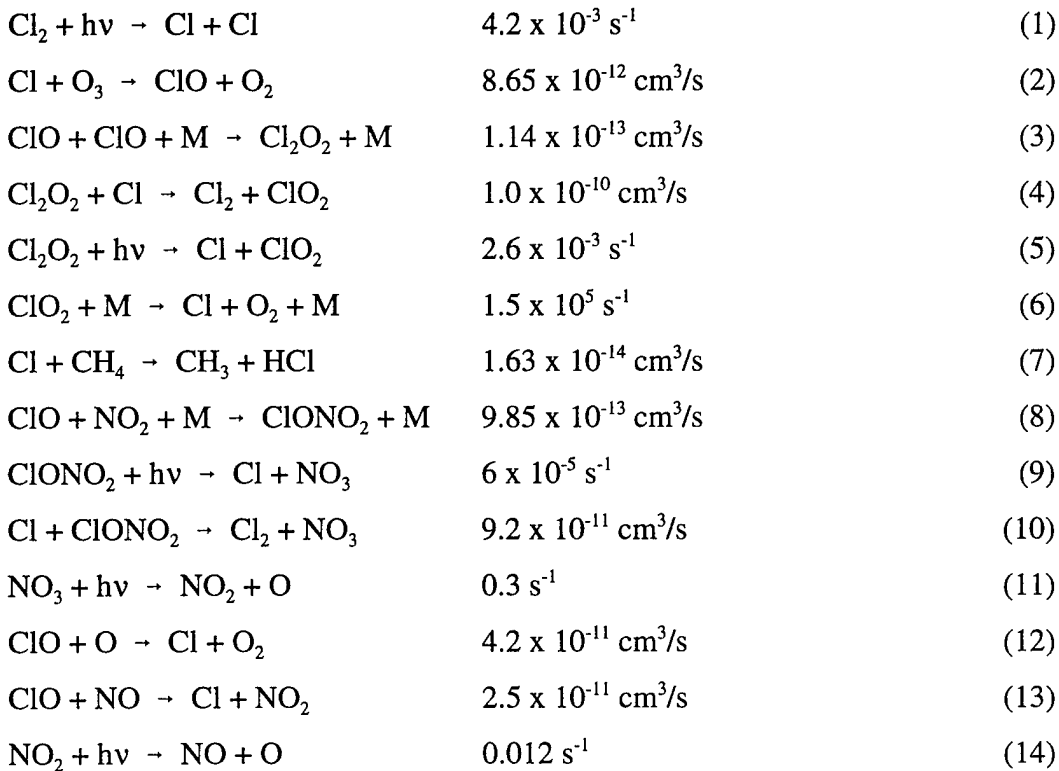
To address these questions, we first examine the basic kinetics of the system, then formulate a simple dimensional model of the expanding/diluting plume, and finally compare the model predictions with the observed O₃ and ClO spatial distributions.

4.1 Chlorine Kinetics

The ClOx catalytic cycle for destruction of ozone is well known from extensive investigations of photochemistry relevant to the ambient stratosphere. The rocket exhaust introduces a massive, highly localized perturbation to the ambient photochemistry. The Delta II rocket employs a kerosene/liquid-oxygen main engine, with solid rocket boosters. The solid-fuel rockets burn aluminum fuel with an ammonium perchlorate oxidizer. The chlorine from the oxidizer is exhausted primarily in the form of HCl, and is partially converted into Cl₂ in the afterburning region of the exhaust plume.⁶ The Cl₂, which is released in very large excess over the ambient Cl and ClO levels, is dissociated into Cl by solar photolysis. The Cl reacts with O₃ to form ClO. Most of the ClO is converted into the dimer Cl₂O₂, which undergoes a series of reactions regenerating Cl₂ and Cl. Thus several ozone molecules can be destroyed for each Cl₂ molecule initially injected by the rocket exhaust. The cycle is terminated when Cl and ClO are finally removed by reactions with ambient CH₄, NO, NO₂, and O. Since none of these species are enhanced in the rocket exhaust (see below), the ClOx regeneration cycle cannot be terminated until (1) sufficient O₃ is destroyed that the Cl + O₃ reaction rate becomes slower than the rate of

reaction between Cl and ambient CH_4 , or (2) the plume becomes fully diluted down to ambient levels. The Delta II data indicate that the chemical time scale is short compared to the dilution time scale, so that most of the atmospheric ozone ingested into the plume is destroyed well before the rocket-injected ClOx reaches ambient levels.

We consider the kinetics of the system in terms of the following mechanism of elementary reactions and rate coefficients for 18 km:



The conditions are: altitude 18 km, $T = 215 \text{ K}$, $[\text{M}] = 2.2 \times 10^{18} \text{ cm}^{-3}$, ambient $[\text{O}_3] = 4.4 \times 10^{12} \text{ cm}^{-3}$ (from the measurements), and other ambient species concentrations, rate coefficients, and photolysis rates are taken from the compilation by DeMore et al.⁷ The expected Cl_2 injection rate of the Delta II rocket motor, 0.5 mole(Cl_2)/m, corresponds to total active-chlorine (as Cl_2) concentrations of $1.5 \times 10^{14} \text{ cm}^{-3}$ (68 ppmv) at an initial diameter of 50 m, $1.6 \times 10^{11} \text{ cm}^{-3}$ (73 ppbv) at the time of Pass 1, and $6.5 \times 10^{10} \text{ cm}^{-3}$ (30 ppbv) at the time of Pass 5. We assume that, initially, the plume contains well-mixed ambient species (mixed by near-field air entrainment) together with plume exhaust species which are diluted into the surrounding atmosphere according to the expansion rate of the plume. The data suggest that, on the time scale of an hour or so, local transport processes can begin to break up the plume structure and accelerate the mixing/dilution of plume species into the surrounding atmosphere. Prior to that time scale, the plume chemistry appears to be well isolated from that of the surrounding atmosphere, such that the volume within the plume may be thought of as a separate chemical system whose composition evolves with time.

An example non-dimensional calculation, shown in Figure 10, illustrates the kinetics of the system. We have assumed an initial Cl_2 concentration of $5 \times 10^{11} \text{ cm}^{-3}$, and have numerically integrated the exact rate law given by the reaction mechanism listed above. As the process initiates through photolysis of Cl_2 , O_3 is consumed by Reaction (2), and some of the Cl_2 is converted into ClO and Cl_2O_2 . Removal of Cl by CH_4 is ~ 1000 times slower than the initial reaction rate of Cl with O_3 . In addition, ClONO_2 concentrations during this period are only slightly greater than normal ambient levels, so removal of Cl by reaction (10) is also negligible. While O_3 is being consumed, $[\text{Cl}]$ is kept low enough that CH_4 is not consumed by Reaction (7). However, $[\text{Cl}]$ is still high enough that the primary fate of Cl_2O_2 is reaction with Cl via Reaction (4) rather than photolysis by Reaction (5) as found in the unperturbed stratosphere. During this period, Cl_2 , ClO , Cl_2O_2 , and Cl are nearly in steady state, and the O_3 loss is nearly linear in time.

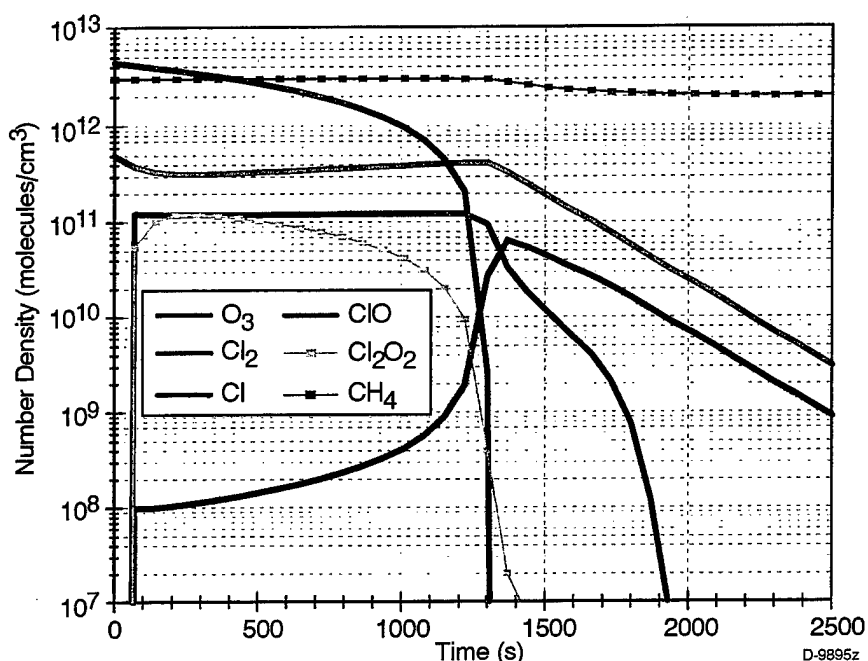


Figure 10. Constant volume kinetics model illustrating ozone and methane consumption by active chlorine at conditions appropriate for 18 km altitude. $[\text{Cl}_2]_0 = 5 \times 10^{11} \text{ cm}^{-3}$, $[\text{O}_3]_0 = 4.4 \times 10^{12} \text{ cm}^{-3}$, $[\text{CH}_4]_0 = 3 \times 10^{12} \text{ cm}^{-3}$, $[\text{M}] = 2.2 \times 10^{18} \text{ cm}^{-3}$, $T = 215 \text{ K}$.

When the O_3 is essentially totally consumed, $[\text{Cl}]$ increases sharply since the only remaining loss for Cl is reaction with CH_4 . Accordingly, CH_4 begins to decrease slowly. $[\text{ClO}]$ and $[\text{Cl}_2\text{O}_2]$ decrease rapidly because there is no more production of ClO from O_3 . ClONO_2 (not shown) is rapidly depleted by the excess Cl . Cl_2 decreases at the solar photolysis rate, and Cl decreases accordingly as it reacts with CH_4 to form HCl .

The process illustrated in Figure 10 is essentially a chemical titration of ozone by the rocket-injected Cl . The endpoint of the titration, i.e. total consumption of ozone, is indicated by a sharp decrease in $[\text{ClO}]$, a sharp increase in $[\text{Cl}]$, and a modest decrease in $[\text{CH}_4]$. This prediction is partially confirmed by observations of CH_4 depletions in Pass 5 and to a lesser

extent in Pass 3 (Eric Richard and Ken Kelly, NOAA Aeronomy Laboratory), both of which show near-total ozone consumption in the core of the plume. In addition, the spatially resolved ClO data for these passes show diminished [ClO] near the core compared to that near the edges, where ozone depletion is only partial (Darin Toohey, University of California at Irvine). We note that the "ClO" measurements as configured for this flight actually constitute measurements of the sum $[ClO] + [Cl]$, so the response of this measurement to the titration endpoint will be muted compared to the responses of individual [ClO] and [Cl] measurements.

Note that the presence of plume-enhanced NO_x would significantly alter the picture presented above. In this event, ozone loss would be accelerated, both through direct reaction with NO and through accelerated conversion of ClO to Cl in Reactions (8-9) and (13). However, this appears not to be the case for these rocket plumes. The main rocket engine uses liquid oxygen as an oxidizer and therefore produces no NO_x in the near-field exhaust. The solid rocket boosters use NH₄ClO₄, however the combustion of the aluminum fuel occurs under conditions that produce little NO_x. The afterburning region, in which residual fuel in the exhaust is burned by entrainment of air into the high-temperature exhaust just behind the rocket, burns at temperatures too low to form NO by the Zeldovich mechanism. Thus we expect the initial NO_x content of the plume to be near ambient levels, in which case Reactions (8) through (14) have negligible impact on the ozone chemistry.

During the period prior to the titration endpoint, the principal chlorine species are in near-steady state, and the ozone depletion kinetics can be described simply by Reactions (1) through (4). The photolysis of Cl₂, Reaction (1), is the rate-limiting step for production of Cl, and essentially every Cl produced reacts with O₃ in Reaction (2). This gives a simple analytical expression for the O₃ destruction rate,

$$d[O_3]/dt = -k_2[Cl][O_3] = -2J_1[Cl_2]_0 \quad (15)$$

where J_1 is the photolysis rate of Cl₂, nominally 0.0042 s⁻¹ at 18 km.⁷ Since ClO is in steady state, produced by Reaction (2) and removed by Reaction (3) at equal rates, we have

$$d[ClO]/dt = k_2[Cl][O_3] - 2k_3[ClO]^2 = 0$$

or

$$d[O_3]/dt = -2k_3[ClO]^2 \quad (16)$$

where k_3 signifies the pressure-dependent bimolecular rate coefficient for reaction (3) as evaluated from the fall-off formulation given in DeMore et al.⁷ Since [Cl₂] and [ClO] are essentially constant during the reaction (i.e. Cl₂ is in excess and ClO is in steady state), the ozone removal rate is constant and [O₃] decreases linearly with time. Thus, for the undiluted cases, we can use the measured ClO concentrations to evaluate the instantaneous ozone removal rate by Reaction (2), and to estimate the initial active-chlorine level in the rocket exhaust, [Cl₂]₀. We have tested the approximations of Equations (15) and (16) against exact numerical solutions like those in Figure 10, and find them to be accurate to $\approx 10\%$ or better.

We examine the apparent and computed ozone destruction rates in Figure 11. The "PSI" and "NOAA" data points represent the observed ozone losses in the core of the plume for Passes 1-6 divided by the age of the plume. However, we note that these quantities are not instantaneous ozone loss rates, but rather represent cumulative losses near the plume centerline. This is emphasized by comparison to the curve labeled "100% O_3 loss", which represents the values that would obtain for 100% ozone loss at each location. Clearly most of the observed ozone loss near the centerline occurs prior to Pass 2.

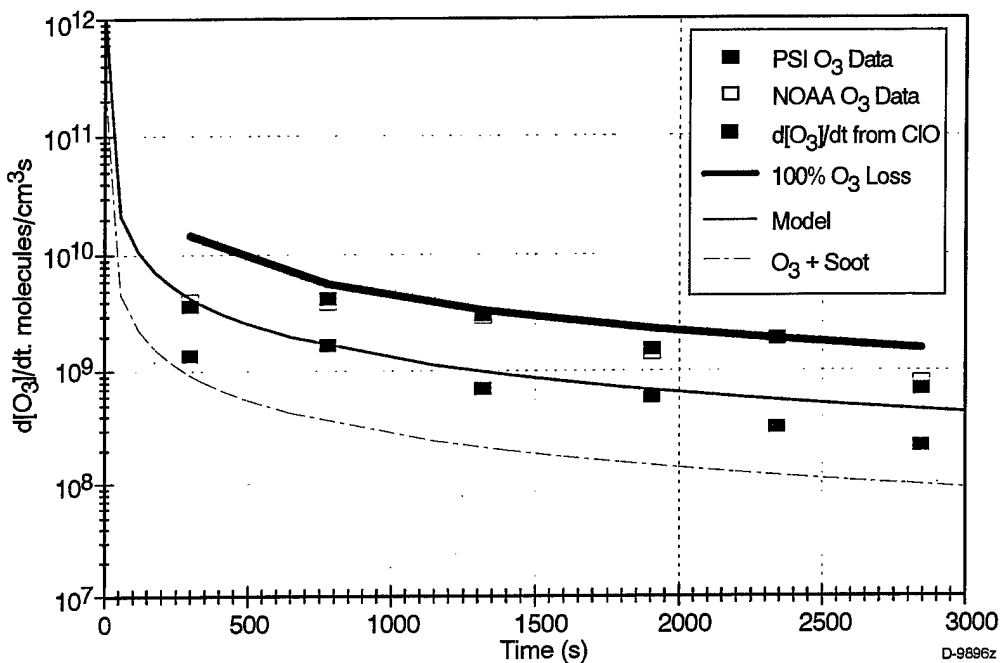


Figure 11. Cumulative and instantaneous ozone loss rates. See text for explanations of symbols and curves.

The kinetics of the observed ozone loss due to chlorine chemistry can be directly examined through use of the measured ClO concentrations in Eq. (16) to determine $d[O_3]/dt$. The points labeled "d[O₃]/dt from ClO" represent the instantaneous ozone destruction rates determined from Eq. (16) using the maximum ClO concentrations observed in each pass. (By using the maximum values rather than the centerline values, we reduce the effects of overtitration observed near the centerline of Passes 3 and 5.) For comparison to these data points, the curve labeled "Model" denotes the instantaneous ozone loss rates as a function of time estimated from Eq. (15) using an initial Cl₂ deposition rate of 0.5 mole/m and a dilution rate of 1965 m²/s (fit to the data in Figure 7). While the predicted rate is larger than that observed in Pass 1, the predicted rates for Passes 2-5 agree fairly well with the observed ones. This means that the assumed active chlorine deposition rate of 0.5 mole/m accounts for the observed ClO levels. Bearing in mind that Passes 3 and 5 have somewhat depressed [ClO] because of overtitration, and that Pass 6 was far from the plume centerline, simple scaling of the model curve shows that an initial active chlorine deposition rate of 0.4 to 0.5 mole/m gives a reasonable fit to the observed rates of ozone destruction due to Reaction (2). The observed rate for Pass 1 is well below the prediction,

perhaps signifying that Pass 1 undersampled the plume centerline due to insufficient spatial resolution (1 s at 180 m/s). The large ozone loss rates in the first 100 s of the plume indicate that ozone near the centerline will be completely consumed well before Pass 1.

The initial active chlorine deposition rate can be determined directly from Eqs. (15) and (16):

$$[\text{Cl}_2]_o = (k_3/J_1)[\text{ClO}]^2$$

For Passes 2, 3, and 4, which give the most definitive sampling of near-titrated ozone removal, we estimate 0.47, 0.54, and 0.32 mole(Cl_2)/m, respectively. These values give a mean Cl_2 deposition rate of (0.45 ± 0.18) mole(Cl_2)/m for the Delta II rocket. This determination is subject to uncertainties in the actual Cl_2 photolysis rate within the rocket exhaust plume. Additional consideration of the $\pm 40\%$ uncertainty in the ClO measurements gives an overall uncertainty of a factor of ~ 2 in the derived active chlorine deposition rate. We conclude that the ClO data are consistent with (0.5×2) mole (Cl_2)/m deposited by the Delta II rocket.

We note that the ClO mixing ratios used in this analysis were evaluated by the author from raw data and an estimated calibration factor supplied by Darin Toohey, and thus do not represent final determinations made by Toohey. Once a final quantitative analysis of the ClO measurements is completed, the analyses described in this report should be repeated using the correct ClO mixing ratios. Conclusions drawn using the current version of the ClO results should be regarded as preliminary.

4.2 Soot Kinetics

Also shown in Figure 11 is an estimate of the instantaneous loss rates of ozone by reaction on soot particle surfaces. These rates were evaluated from assumed plume soot loadings rather than from the actual particle measurements of the University of Missouri-Rolla instrumentation; quantitative analysis of the particulate data should lead to more well-constrained determinations.

The reaction of ozone with various types of carbonaceous surfaces has been studied in the laboratory. The reported reaction efficiency, γ , is 3×10^{-3} with an uncertainty factor of 30 up and down.⁷ The ozone loss rate is given by

$$-\frac{d[\text{O}_3]}{dt} = (\bar{v} \gamma A_s / 4)[\text{O}_3] \quad (17)$$

where \bar{v} is the average thermal molecular velocity in cm/s and A_s is the concentration of soot surface area in cm^2/cm^3 .

To evaluate A_s , we need to know the number density and area-averaged size of the soot particles in the plume. This information should eventually be forthcoming from analysis of the particle size distributions obtained by the University of Missouri-Rolla instrument. For present purposes, we adopt an estimated post-afterburning soot deposition of 0.01 kg/m, intermediate in

the range 0.005 to 0.025 kg/m expected for the Delta II kerosene/LOx main engine (M. Ross, private communication). We further assume an area-weighted average radius of 30 nm, which is typical of combustion-generated soot particles. For the dilution rate deduced from the data in Figure 7, these assumptions give soot particle number densities of $8 \times 10^4 \text{ cm}^{-3}$ for Pass 1 and $1 \times 10^4 \text{ cm}^{-3}$ for Pass 5. The surface area A_s is then given by

$$A_s = 4\pi r^2 N_p$$

This gives values of 9.0×10^{-6} and $1.1 \times 10^{-6} \text{ cm}^2/\text{cm}^3$ for Passes 1 and 5, respectively. The maximum ozone loss rate is determined by using the initial ambient ozone concentration in Eq. (17), giving the curve labeled "O₃ + soot" in Figure 11. Clearly, as ozone diminishes, this rate becomes slower. The estimated initial soot reaction rate is about a factor of 5 lower than that estimated from the ClO data for the Cl + O₃ reaction. However, we note the factor of 30 uncertainty in the reaction efficiency, as well as additional substantial uncertainties in the assumed soot deposition and mean particle size. While it appears that reaction of ozone with soot is probably slow compared to reaction with Cl, the range of uncertainties in the estimate precludes a definitive conclusion. As discussed below, comparison of the estimated O₃ + soot reaction rate, the Cl + O₃ reaction rate, and the total O₃ loss suggests that reaction of O₃ on soot surfaces may contribute to the observed O₃ loss.

4.3 Plume Model

We now wish to examine whether the observed cumulative ozone losses correspond to removal by the active chlorine mechanism alone. This requires a model of the spatial extent of the plume-depleted ozone as a function of time. A sophisticated model would account for expansion and dilution of the plume as well as mixing with the external atmosphere. For present purposes, we will treat the plume expansion but neglect the mixing effects; based on the data, it appears that, for time scales less than 1 hour, external mixing effects will simply "blur" the species radial profiles near the edges of the plume. The present analysis focuses on processes occurring in the core of the plume.

The analytical reductions of Eqs. (15) and (16) lend themselves well to a spatially resolved model of the radial extent of the ozone loss. We divide the plume radius at any time t into 25 m annular bins. As time progresses and the plume expands, diluted active chlorine at concentration [Cl₂]_o enters a new bin and encounters previously unperturbed ambient atmospheric ozone levels, at a time t_o . The ozone loss in that bin at a subsequent time t is then given by

$$\Delta[\text{O}_3] = \int_{t_o}^t 2J_1[\text{Cl}_2]_o \, dt \quad (18)$$

where

$$[\text{Cl}_2]_o = R/A(t),$$

R is the initial active chlorine deposition rate from the rocket, and the cross sectional area A(t) increases at $1965 \text{ m}^2/\text{s}$ as discussed above. Equation (18) is an analytically soluble integral which tracks the evolution of chemical ozone loss coupled with radial plume chlorine dilution.

Computed results for each measurement pass assuming 0.25 and 0.5 mole(Cl_2)/m are shown in Figures 12 and 13, respectively. For $R = 0.25$ mole/m, the region of maximum ozone depletion remains rather small, <100 m in radius. The ozone data clearly indicate development of the depleted region ($>50\%$ depletion) to 500 - 600 m radius by the time of Pass 5. The calculations for $R = 0.5$ mole/m give ozone depletion half-widths (full width at half maximum) which agree reasonably well with the observations, especially for Passes 4 and 5. Figure 14 shows a comparison of the computed and observed diameters of the plume regions where ΔO_3 exceeds 1000 ppbv (essentially the ozone depletion half-widths). Clearly, the assumption of 0.25 mole(Cl_2)/m gives ozone depletion dimensions which are well below the observed values, while 0.4 to 0.5 mole(Cl_2)/m give a reasonable match to the data.

The model predictions can also be compared with the data in terms of maps of the relationship between ozone consumed and ClO produced. Computed results for 0.25 and 0.5 mole/m, averaged over a 200 m spatial resolution, are shown in Figures 15 and 16; the measurement results are plotted in Figure 17. ClO mixing ratios are computed for each radial

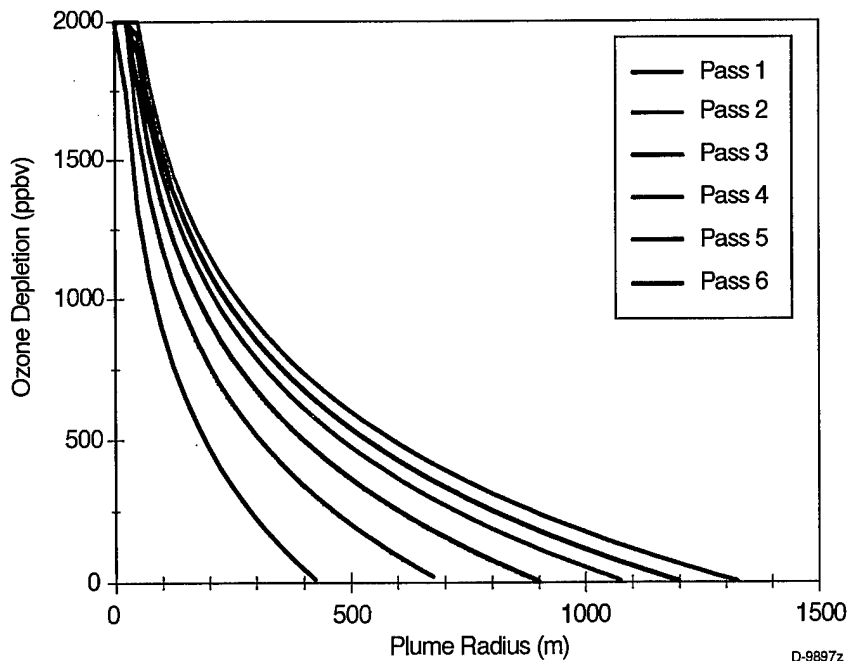


Figure 12. Computed ozone depletion radial profiles at 18 km altitude assuming $R(\text{Cl}_2) = 0.25$ mole/m. The ambient ozone mixing ratio is 2000 ppbv.

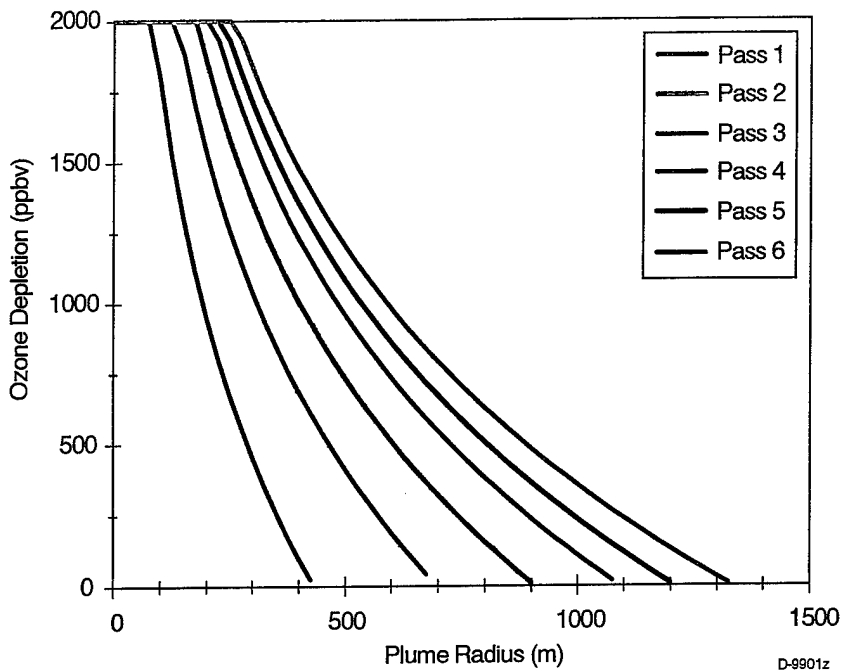


Figure 13. Computed ozone depletion radial profiles at 18 km altitude assuming $R(Cl_2) = 0.5$ mole/m. The ambient ozone mixing ratio is 2000 ppbv.

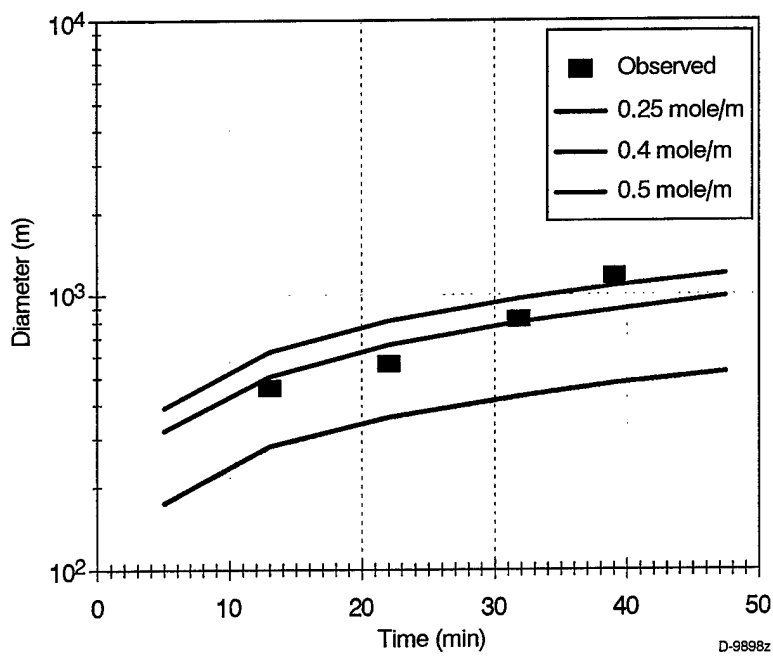


Figure 14. Computed and observed ozone depletion diameters for the region of the plume where ΔO_3 exceeds 1000 ppbv.

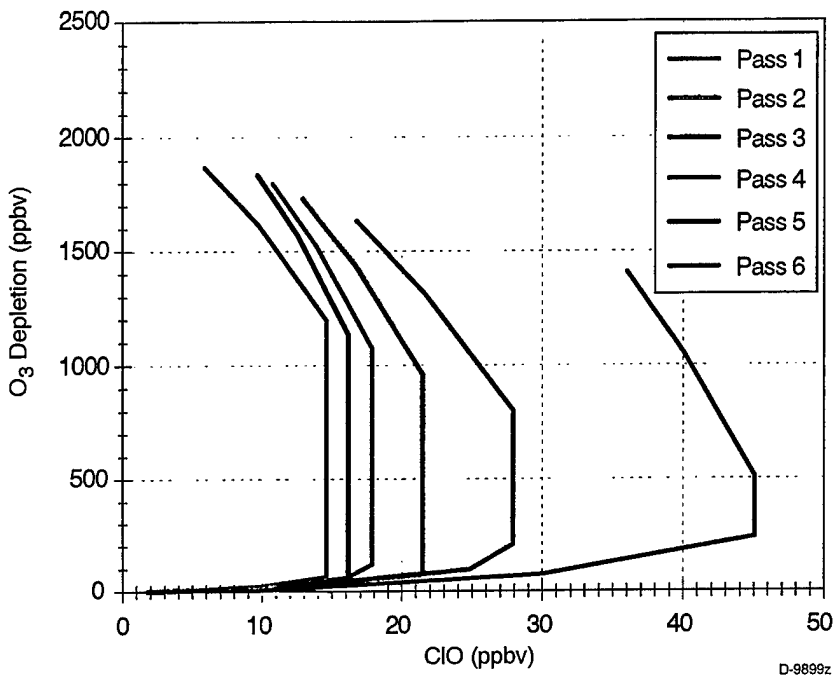


Figure 15. Modeled dependence of O_3 loss on ClO for a spatial resolution of 200 m, assuming $R(Cl_2) = 0.25$ mole/m.

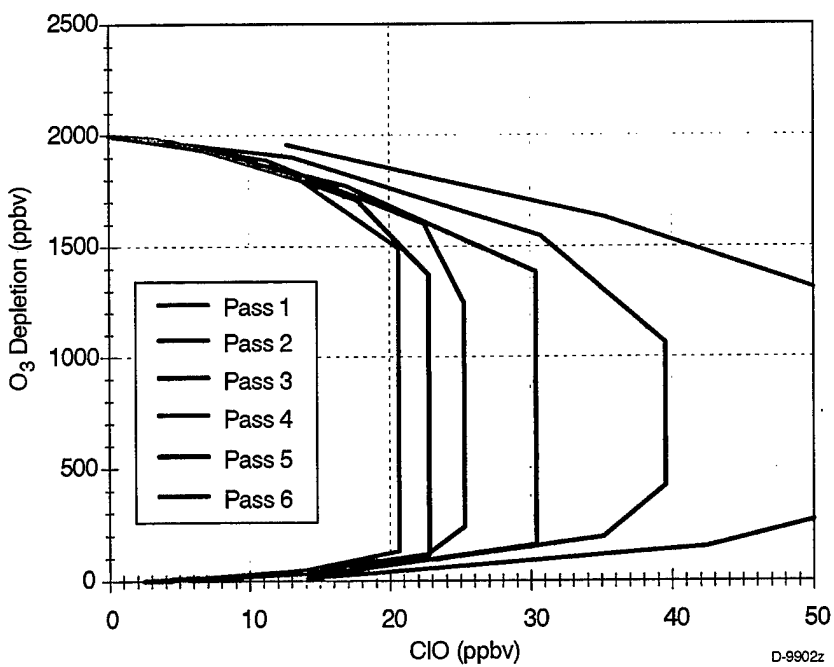


Figure 16. Modeled dependence of O_3 loss on ClO for a spatial resolution of 200 m, assuming $R(Cl_2) = 0.5$ mole/m.

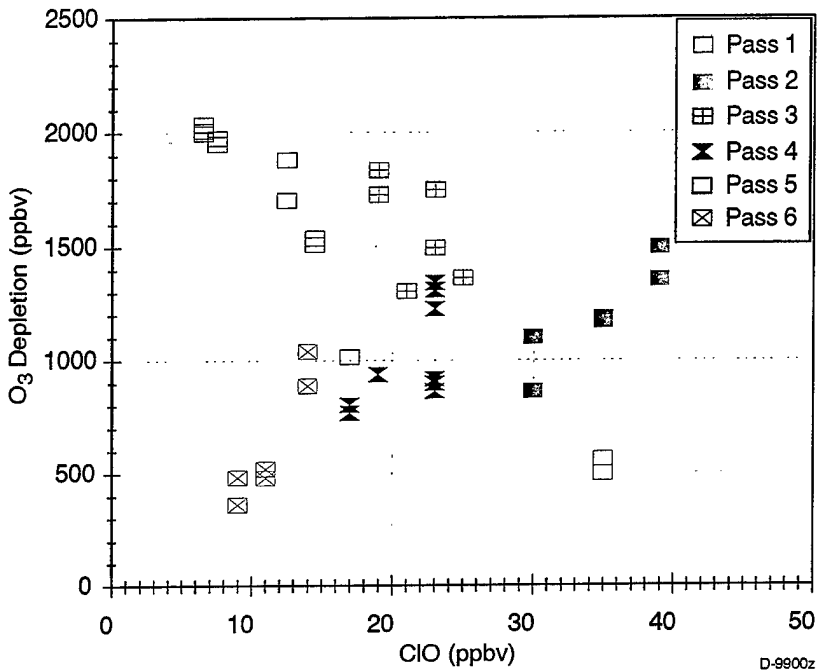


Figure 17. Observed dependence of O_3 loss on ClO for the Delta II rocket.

position and measurement time from Eqs. (15) and (16). The model predictions crudely incorporate the effects of overtitrination at 100% ozone depletion by setting ClO values to zero wherever the computed ΔO_3 value is 2000 ppbv. Values near the lower edge of the plots (near zero ozone depletion) sample the outer edge of the plume, where the model fails to account for mixing with the ambient air; here we expect the model to overpredict the ClO production and ozone depletion. Values near the top of the plots (ozone depletion near 2000 ppbv) sample near the centerline of the plume. As above, we again see that Pass 1 apparently failed to resolve the central region of the plume; this is consistent with the predicted profiles in Figure 13, which show an ozone depletion radius of <200 m for Pass 1, comparable to the measurement spatial resolution element of 180 m. The assumption of $R = 0.5$ mole/m is required to account for the large, ≈ 40 ppbv ClO levels measured in Pass 2. The maximum ClO values for Pass 4 are more consistent with a slightly lower value of $R = 0.4$ mole/m. The Pass 3 data, which are somewhat affected by overtitrination, are consistent with $R \geq 0.3$ mole/m. Pass 5 is strongly affected by overtitrination of the ozone and thus should give an underestimate of R . Pass 6, as noted earlier, sampled near the edge of the plume where external mixing effects are expected to reduce both the ozone depletion and the ClO. The observed ClO levels are seen to drop off sharply above $\Delta O_3 = 1500$ ppbv, near the plume centerline, as is reflected by the predictions for $R = 0.5$ mole/m.

The general consensus of the comparisons between the plume model predictions and the data is that the observed spatial distribution of the ozone-depleted region is consistent with $R \approx (0.4 \pm 0.1)$ mole/m. The same appears to be true for the observed correspondences between ozone consumed and ClO produced, although the uncertainty here is a factor of 2. Unfortunately, this data set does not sample the plume in enough statistical detail to give self-consistent results

for all the measurement passes. Since the observed ClO levels indicate an active chlorine deposition rate of $\approx(0.5 \times \div 2)$ mole(Cl_2)/m, and the ozone spatial distributions indicate $\approx(0.4 \pm 0.1)$ mole(Cl_2)/m, we conclude that most of the observed ozone loss within the plume is due to reaction with Cl. However, the experimental uncertainty in the closure between the Cl reaction rate and the O_3 depletion is large compared to the $\approx 20\%$ contribution expected for the direct reaction with soot. Thus the possibility of O_3 loss due to reaction with soot particles cannot be ruled out, nor can it be clearly identified from the present data set.

The observation of $\approx(0.5 \times \div 2)$ mole(Cl_2)/m from the Delta II rocket, compared to the expected value of 0.5 mole/m, raises some interesting questions. Is this the quantity actually produced in the rocket exhaust, i.e. is this value consistent with detailed models of the afterburning chemistry? Can some of the apparent chlorine activation be due to hitherto unidentified chemical processes, such as heterogeneous activation of chlorine by conversion of rocket-exhausted HCl on particle surfaces? More detailed examination of plume flowfield predictions of the rocket exhaust composition are required to further address this point.

5. SUMMARY AND CONCLUSIONS

We have described airborne WB57F measurements and intercomparisons of ozone depletion dynamics in the exhaust plumes of Delta II and Atlas IIAS rockets in the lower stratosphere. We have analyzed the Delta II data set in considerable detail, both by deduction of basic quantities from the data and by forward modeling to compare simulations with the observations. The data delineate the time scales for plume dilution, photochemical reaction, and mixing of the plume-perturbed air parcel with the external atmosphere. The primary chemical perturbation within the plume is due to photolysis of rocket-generated Cl_2 and subsequent reaction of Cl with ozone. This reaction proceeds until at least half of the ozone within the expanding plume volume is consumed, resulting in total ozone consumption in the central 20 to 30% of the plume diameter. Ozone consumption within the plume occurs on a much shorter time scale than full dilution or dynamically induced plume breakup. The total consumption of the ozone in the plume core leaves a characteristic, observable chemical signature of ClO production followed by ClO and CH_4 depletion.

We have examined the O_3 depletion and ClO production data to address basic questions regarding the viability of reaction mechanisms. Our preliminary conclusions are:

- (1) The observed ozone depletions and ClO productions are consistent with the reaction of O_3 with Cl generated from rocket-derived Cl_2 in a catalytic, regenerative photochemical cycle analogous to that found in the ambient stratosphere.
- (2) The heterogeneous reaction of ozone on soot particles produced by the rocket motor may contribute to the observed ozone loss. (a) The expected reaction rate of ozone with soot is about 1/5 of that for ozone with Cl, albeit with order-of-magnitude uncertainties. (b) The observed $\text{Cl} + \text{O}_3$ and total O_3 destruction rates are essentially equal, but with an uncertainty much larger than the magnitude of the expected reaction rate between ozone and soot. There is no obvious additional deficit to indicate a substantial heterogeneous reaction rate.
- (3) The observed ClO production and ozone depletion indicate an initial active chlorine deposition by the rocket which is consistent with the expected value of 0.5 mole(Cl_2)/m. However, due to the considerable uncertainties which remain, the modeled chlorine output of the Delta II rocket and afterburning region needs to be re-evaluated. In addition, consideration should be given to possible unknown mechanisms for conversion of HCl to Cl_2 in the rocket exhaust plume, e.g. heterogeneous reactions on rocket-exhausted soot and/or aluminum oxide particles.

6. REFERENCES

1. M.N. Ross, J.O. Ballenthin, R.B. Gosselin, R.F. Meads, P.F. Zittel, J.R. Benbrook, and W.R. Sheldon, "In-Situ Measurement of Cl₂ and O₃ in a Stratospheric Solid Rocket Motor Exhaust Plume," *Geophys. Res. Lett.* **24**, 1755 (1997).
2. M.N. Ross, J.R. Benbrook, W.R. Sheldon, P.F. Zittel, and D.L. McKenzie, "Observation of Stratospheric Ozone Depletion in Rocket Exhaust Plumes," *Nature* **390**, 62 (1997).
3. W.T. Rawlins, D.M. Sonnenfroh, and M.H. Proffitt, "Laboratory Intercomparisons and In-Flight WB-57F Measurements of Tropospheric Ozone by a Prototype UV Ozone Photometer," PSI-2388/TR-1496, Physical Sciences Inc., Andover, MA, July 1997.
4. W.T. Rawlins, D.M. Sonnenfroh, D.A. Palombo, P.A. Mulhall, A.H. Burbo, H.C. Murphy, G. Dippel, M.R. Malonson, S.D. Sewell, and R.H. Krech, "Lightweight Ozone Photometer for Balloon and Aircraft Atmospheric Measurements," PSI-2328/TR-1503, Final Report for NASA Contract NAS7-1381, Physical Sciences Inc., Andover, MA, July 1997.
5. M.H. Proffitt, M.J. Steinkamp, J.A. Powell, R.J. McLaughlin, O.A. Mills, A.L. Schmeltekopf, T.L. Thompson, A.F. Tuck, T. Tyler, R.H. Winkler, and K.R. Chan, "In Situ Ozone Measurements Within the 1987 Antarctic Ozone Hole from a High-Altitude ER-2 Aircraft," *J. Geophys. Res.* **94**, 16547 (1989).
6. M. Ross, "Local Effects of Solid Rocket Motor Exhausts on Stratospheric Ozone," *J. Spacecraft and Rockets* **33**, 144 (1996).
7. W.B. DeMore, S.P. Sander, D.M. Golden, R.F. Hampson, M.J. Kurylo, C.J. Howard, A.R. Ravishankara, C.E. Kolb, and M.J. Molina, "Chemical Kinetics and Photochemical Data for Use in Stratospheric Modeling, Evaluation Number 12," JPL Publication 97-4, Jet Propulsion Laboratory, January 15, 1997.